IntechOpen

UWB Technology and its Applications

Edited by Dusan Kocur

UWB TECHNOLOGY AND ITS APPLICATIONS

Edited by **Dusan Kocur**

UWB Technology and its Applications
http://dx.doi.org/10.5772/intechopen.74349
Edited by Dusan Kocur

Contributors

Ikram E Khuda, Rabia Yahya, Makoto Itami, Akira Nakamura, Xuehui Guan, Yuan He, Ke Xu

© The Editor(s) and the Author(s) 2019
The rights of the editor(s) and the author(s) have been asserted in accordance with the Copyright, Designs and Patents Act 1988. All rights to the book as a whole are reserved by INTECHOPEN LIMITED. The book as a whole (compilation) cannot be reproduced, distributed or used for commercial or non-commercial purposes without INTECHOPEN LIMITED’s written permission. Enquiries concerning the use of the book should be directed to INTECHOPEN LIMITED rights and permissions department (permissions@intechopen.com).
Violations are liable to prosecution under the governing Copyright Law.

Individual chapters of this publication are distributed under the terms of the Creative Commons Attribution 3.0 Unported License which permits commercial use, distribution and reproduction of the individual chapters, provided the original author(s) and source publication are appropriately acknowledged. If so indicated, certain images may not be included under the Creative Commons license. In such cases users will need to obtain permission from the license holder to reproduce the material. More details and guidelines concerning content reuse and adaptation can be foundat http://www.intechopen.com/copyright-policy.html.

Notice

Statements and opinions expressed in the chapters are these of the individual contributors and not necessarily those of the editors or publisher. No responsibility is accepted for the accuracy of information contained in the published chapters. The publisher assumes no responsibility for any damage or injury to persons or property arising out of the use of any materials, instructions, methods or ideas contained in the book.

First published in London, United Kingdom, 2019 by IntechOpen
eBook (PDF) Published by IntechOpen, 2019
IntechOpen is the global imprint of INTECHOPEN LIMITED, registered in England and Wales, registration number: 11086078, The Shard, 25th floor, 32 London Bridge Street
London, SE19SG – United Kingdom
Printed in Croatia

British Library Cataloguing-in-Publication Data
A catalogue record for this book is available from the British Library

Additional hard and PDF copies can be obtained from orders@intechopen.com

UWB Technology and its Applications
Edited by Dusan Kocur

p. cm.

Print ISBN 978-1-78985-715-3

Online ISBN 978-1-78985-716-0

eBook (PDF) ISBN 978-1-83962-069-0

Meet the editor

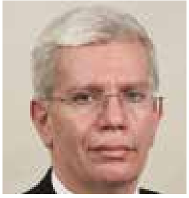

Dušan Kocur was born in Kosice, Slovakia, in 1974. He received his M.Sc. and Ph.D. degree in Radioelectronics from the Faculty of Electrical Engineering, Technical University of Košice, in 1985 and 1990, respectively. Nowadays, he is a full professor at the Department of Electronics and Multimedia Communications of his Alma Mater. His main research interests include ultra-wideband (UWB) radar systems, real-time operating UWB localization systems, UWB sensor network and UWB radar with synthetic aperture. He has also dealt with UWB radar signal processing focused on short-range localization and tracking of moving and static persons and on contactless monitoring of breathing frequency and heart rate of human beings. He has published more than 230 scientific papers in books, journals and conference proceedings.

Contents

Preface

Ultra-wideband (UWB) technology is a radio technology that uses electromagnetic waves with a very low power spectral density occupying a bandwidth of more than 25% of a centre frequency, or more than 0.5GHz, for short-range remote sensing, high-bandwidth communications or object positioning. As UWB systems exploit a very large frequency band, they can provide high-range resolution for sensors, radars, object positioning and a high transmission rate for wireless communication systems. This feature of UWB technology has motivated researchers to develop a range of interesting applications of UWB systems. They include person localization and tracking at security operation and disaster events, contactless monitoring of breathing frequency and heart rate of human beings, medical and industrial applications of microwave imaging, ground penetrating and automotive radars, positioning systems, impedance spectroscopy, wireless communication systems, etc.

The detailed analyses of state-of-the-art UWB technology has shown that UWB technology can be considered very interesting, promising and having great application potential. Following these facts, our book attempts to present current and emerging trends in research and development of UWB systems as well as some future expectations. The book consists of five chapters. The chapters are focused on basic components of UWB systems and on some applications of UWB systems.

The first chapter is devoted to early detection of cancers using UWB technology. By early detection, we mean identification of tumours before the symptoms become visible. This can be done clinically using modern instrumentation and procedures referred to as screening. In this field, UWB microwave imaging has been introduced as a possible tool for replacing prior screening techniques such as X-rays, ultrasound and MRI to be applied for cancer detection. Following this idea, the chapter compares UWB technology with other screening techniques to be applied for cancer detection. Moreover, selected properties of human tissues allowing identification of tumours are studied in the chapter.

In the next chapter, an overview of the fundamental applications of frequency selective surfaces (FSS) in antenna engineering is presented. Here, special attention is paid to antennas for UWB systems employing FSS. In this field, the basic FSSs such as the capacitive and its complementary inductive FSSs to design UWB reflectors that can serve improving and stabilizing the gain of UWB antennas are considered. Thereafter, a proposed UWB single-layer FSS is used to serve the same purpose. And finally, the FSS is integrated and designed together with UWB radiators, which has resulted in lower profile along with a good performance.

It is well known that bandpass filters such as resonators (stub-loaded resonator, slot-line resonator, multi-mode resonator) and notch filters are an essential part of UWB systems. These components of UWB systems are studied in the third chapter. The chapter is focused on microstrip multimode resonator based bandpass UWB filters. Besides that, filters that decrease the interference between UWB systems and existing communication system such as WLAN and WiMAX are discussed in the chapter. It is shown that such filters can be obtained by insertion of notch bands in the UWB passband. Several novel designs have been proposed and realized to verify the proposed design scheme.

The fourth chapter is focused on human target monitoring using UWB radar. In this chapter, a novel concept, called range-Doppler surface, for human target analysis using UWB radar is described. The construction of range-Doppler surface involves range-Doppler imaging, adaptive threshold detection and isosurface extraction. A Keystone-transform-based range migration compensation approach is applied to allow high-quality range-Doppler imaging using UWB radar. Adaptive threshold detection is applied to detect the extended target in the range-Doppler image. And finally, range-Doppler surface is constructed by extracting an isosurface from a range-Doppler video sequence defined as a sequence of range-Doppler images. In comparison with micro-Doppler profiles and high-resolution range profiles, range-Doppler surface contains range, Doppler and time information simultaneously. The importance of the range-Doppler surface in the field of person monitoring is illustrated by simulations and experimental results. The obtained results show that the range-Doppler surface applications open a new area in the field of human target analysis.

The final chapter deals with photonic technologies applied for UWB signal processing. It is well known, that UWB signals generated in the optical domain can benefit the advantages of the large bandwidth and compatibility with optical fibre network. With regard to the importance of this approach, an overview of the UWB signal processing using photonic techniques is presented in this chapter. The chapter is focused on UWB signal generation and modulation using photonic approaches. The basic principles of this approach are based on linear optics, nonlinear optics, electro-optics covering a wide scope of hot topics in photonics area. The technical implementations rely on optoelectronic components, photonic integrated circuits, or novel 2D materials. The working principle, technical implementations, pros and cons, applications and the prospects are discussed in this chapter.

The contributors hope that readers will find in our book some new and useful insight into the discussed field of UWB technology and its applications.

Dušan Kocur
Department of Electronics and Multimedia Communications
Faculty of Electrical Engineering and Informatics
Technical University of Kosice, Slovakia

Feasibility of the Detection of Breast Cancer Using Ultra-Wide Band (UWB) Technology in Comparison with Other Screening Techniques

Ikram E Khuda

Additional information is available at the end of the chapter

http://dx.doi.org/10.5772/intechopen.79679

Abstract

Breast cancer is considered a leading cause of deaths among women. Researches state that women around the world still face this problem, and because of its unawareness, it is many times left unattended in the budding stages. If correctly screened and detected early, then with proper treatment, this could stop the metastasis and reduce the pains and difficulties of the later stages. Screening methods such as x-ray-based mammography, ultrasound, PET scan, and magnetic resonance imaging (MRI) clinically exist for breast tumor investigation. It is very important that screening procedures should have high specificity and sensitivity for the detection of tumors. Additionally, these methods also have to placate concerns such as ease of the patient during imaging, high-resolution images for added precise elucidation, cost effectiveness, and the capacity to detect the malignant-leading tumors in the early stage. Existing imaging techniques do not meet all of these conditions concurrently. In this scenario, ultra-wide band (UWB) technology has come into play the role of a useful alternative for screening and detection of breast tumors. This chapter discusses firstly probabilistic qualitative metrics which are used in measuring the quality of testing procedures, and then later UWB testing methods are discussed in brief.

Keywords: cancer, breast cancer, x-rays, MRI, ultrasound, UWB, microwave tomography, radars

1. Introduction

Cancer is a syndrome characterized by an uncontrolled anomalous growth of cells, originating anywhere in the human body and spreading to other nearby tissues and organs as a chain reaction and at an exponentially fast pace. The mass formed by these cells is called tumor. These can be malignant or benign. A malignant tumor can grow uncontrollably to other parts of the body. Comparatively, a benign tumor can grow but does not spread. Cancers that are defined by the existence of tumors are carcinomas and sarcomas. The spreading of cancer cells, which also characterize them as malignant, is called metastasis. New metastatic tumor in some other organ or tissue is of the same type from where it was originated. For example, if breast cancer spreads into the lungs, the cancer cells in the lungs are designated as breast cancer cells. Hence, it is quite apparent that early detection of the presence of cancer cells is a very important stage to cure it. This early detection is called screening. The whole objective of screening is to stop the metastasis stage as early as possible.

Scientists and researchers are always in the continuum to develop the methods which could help in the finding of cancer cells well before the symptoms appear or impact of cancerous cells could be observed/felt with as convenience as possible to the patients. Modeling new cancer screening methods is an area of active research in medicine and biomedical engineering.

Screening methods available or in use at present and clinically accepted include x-ray mammography, ultrasound, and magnetic resonance imaging (MRI) [1–3]. Another screening method which is still under experimental research is ultra-wide band (UWB) technology. In this chapter we shall discuss about the feasibility of UWB technology for early detection of breast cancer.

2. Breast cancer screening techniques

2.1. X-ray mammography

X-rays are electromagnetic waves having wavelengths varying from 0.01 to 10 nanometers, belonging to frequencies in the range 30 petahertz to 30 exahertz (3×10^{16}–3×10^{19} Hz) and having energies from 100 eV to 100 keV. Their wavelength is shorter than UV rays and longer than gamma rays. X-ray mammography employs controlled dose of these radiations for producing images (radiographs) to early detect breast cancer before the symptoms become visible. X-ray radiography is noninvasive if used controllably, i.e., in small dose. Exhausting a standard measure of radiation dose, millisievert (mSv), the total dose for a screening mammogram with two views of each breast (four images total) is approximately 0.4 mSv [4, 5]. The radiation which a woman receives with a screening mammogram is about equal to the dose received over 7 weeks from natural surroundings or background radiation. The radiation dose from a mammogram is little more than from a chest x-ray. Interestingly, if the radiation dose from x-rays is not controlled, then they themselves can become a high risk of producing breast cancer. This effect is because of the ionizing nature of high-energy x-rays at high frequencies. Hence, using x-rays for mammography requires ensuing precise guidelines and conducting regular equipment inspections to guarantee that the equipment is safe and uses the lowest radiation dose possible for producing high-quality, investigative images. The frequency of x-rays and their energy with duration of emission (dose) set the quality of x-rays which are difficult to trade off for each other.

Penetration of x-rays is directly proportional to the wavelength. So, high-frequency x-rays have low power to penetrate than low-frequency x-rays. In comparison, energy of the transmitting x-rays varies inversely with the wavelength and directly with the frequency of transmission. Thus, high-frequency x-rays lead to high-energy photons and also produce better resolution of the mammogram. But, at the same time, the higher the penetrating power is of the x-rays, the more is their ionizing effect.

So, although x-ray mammography is a conventional method for breast cancer screening, it is not easy to trade off between low-frequency x-rays (for higher penetration), low-energy x-rays for less ionization, and simultaneously high-energy x-rays for better resolution of the mammogram. Also, as reported in [6, 7], the rate of failure in detecting the tumor using x-ray mammography is significantly considerable and therefore cannot be neglected. This includes false-positive and false-negative probabilities.

2.2. Magnetic resonance imaging (MRI)

An alternative to x-ray mammography is magnetic resonance imaging or MRI for detecting breast tumors or other cancer tumors. MRI offers better sensitivity as compared to X-rays, but besides the cost of the examination, the specificity is very little and can lead to erroneous diagnosis [8]. MRI does not involve x-rays and other ionizing radiations. The frequencies used are in 60 MHz range [8]. This is quite low as compared to x-rays. The human body mostly comprises water and chemically water molecules (H_2O) contain hydrogen nuclei (which are protons). They become aligned in a magnetic field. An MRI scanner produces such a strong magnetic field (about 0.2–3 tesla), which aligns the proton "spins." The scanner also produces a current that creates a varying magnetic field of approximately 60 MHz. The protons absorb the energy from the magnetic field and flip their spins. When the field is removed, the protons gradually return to their normal spin (precession). The return process produces a radio signal that can be measured by the receivers in the scanner and converted into an image. Protons in different body tissues return to their normal spins at diverse rates, so the scanner can differentiate among various types of tissues. The scanner settings can be adjusted to produce contrasts between the body tissues. Surplus magnetic fields are used to produce three-dimensional images that may be viewed from different angles. There are many forms of MRI, but diffusion MRI and functional MRI (fMRI) are two of the most commonly used forms in biomedical imaging. Diffusion MRI measures the way water molecules diffuse through body tissues. Certain disease processes—especially tumor—can hamper this diffusion, thus helping to diagnose them. In addition to structural imaging, functional MRI can also be used to visualize functional activities. Functional MRI, or fMRI, is used to measure changes in blood flow to different parts of the tissues or organ.

2.3. Ultrasound waves

This is another alternative for detecting and screening the presence of tumors and specifically breast tumors. In this testing procedure, high-frequency sound waves are transmitted to the effected tissue, and without involving radiations, the received signals are converted into images. Ultrasound cannot replace the effectiveness of mammogram or MRI. It is only used to see if the breast lump is filled with cyst or if it is solid. Ultrasound can also be used to characterize the type of tumor. They are considered a good extension of physical palpations which use touching the breasts to detect the presence of any tumors. But they are limited to penetration because of lower frequency as compared to MRI and x-ray mammograms. Ultrasound waves have frequencies above about 20 kHz [9, 10].

3. Quality of diagnostic testing procedure

It should be understood that testing the presence of breast tumor (just like any other tumor) is a random experiment with probabilities associated with the outcomes. Therefore, the quality of diagnostic tests can be measured using the probabilities associated with them. A test can be positive (detect tumor) when the tumor is actually present (true positive), and a test can also be positive (detect tumor) when there is no tumor at all (false positive). Likewise, a test can be negative (does not detect tumor) when the tumor is not present (true negative), and a test can also be negative (does not detect tumor) when the tumor is actually present (false negative). Out of these four different probabilities, the two which are normally used to qualitatively access the diagnostic procedure accuracy are *sensitivity* which is the true-positive rate probability and *specificity* which is the true-negative rate probability. If T^+ indicates the test is positive, T^- indicates the test is negative, C^+ indicates existence of cancer, and C^- indicates the absence of cancer, then the conditional probabilities stated above are shown in **Table 1**.

Sensitivity, specificity, and other probabilities which are used in the test's qualitative measure can be easily calculated using Bayes' theorem. If "a," "c," "b," and "d" indicate the test positive and cancer-carrying persons, test positive and cancer-not-carrying persons, test negative and cancer-carrying persons, and test negative and cancer-not-carrying persons, respectively, then using **Table 2**, the probabilities in **Table 1** and other percentages can be calculated in **Table 3** at any confidence interval (CI).

The statistics of the cancer-detecting modalities in **Table 4** suggests that despite their recognized ability to detect tumors they still have their lackings. False-positive rate and false-negative rate are not negligible. False-positive rates lead to a number of needless surplus investigations which could produce ionization. In the context of false-negative rate, if a fraction of the tumors are not detected at an early stage, then this could lead to malignancy and

Probability name	Conditional probability
True positive	$P(T^+/C^+)$
False positive	$P(T^+/C^-)$
False negative	$P(T^-/C^+)$
True negative	$P(T^-/C^-)$

Table 1. Conditional probabilities associated with cancer diagnostic tests.

	Cancer tumor		
Test	**Present**	**Absent**	**Total**
Positive	a	c	a + c
Negative	b	d	b + d
Total	a + b	c + d	a + b + c + d

Table 2. Cross tabulation table of conditional probabilities.

S. no	**Test statistics**	**Computation method**	**Definition/interpretation**
1.	Sensitivity	a/(a + b)	It is the true-positive rate. This shows the probability that a test result will be positive when the cancer tumor is present
2.	False-negative rate	1-Sensitivity = b/(a + b)	This shows the probability of a negative test result given that the cancer tumor is present
3.	Specificity	d/(c + d)	It is the true-negative rate. This shows the probability that a test result will be negative when the cancer tumor is absent
4.	False-positive rate	1-Specificity = c/(c + d)	This shows the probability of a positive test result given that the disease is not present
5.	Positive likelihood ratio	Sensitivity/(1-specificity)	It is the ratio of the true-positive rate to the false-positive rate.
6.	Negative likelihood ratio	1-Sensitivity/(specificity)	It is the ratio of the false-negative rate to the true-negative rate
7.	Cancer prevalence	(a + b)/(a + b + c + d)	This shows total probability of the presence of cancer tumor
8.	Cancer absence	(c + d)/(a + b + c + d)	This shows total probability of the absence of cancer tumor
9.	Positive predictive value	a/(a + c)	This shows the probability that the cancer tumor is present given the test is positive
10.	Negative predictive value	d/(b + d)	This shows the probability that the cancer tumor is absent given the test is negative
11.	Accuracy	(a + d)/(a + b + c + d)	This shows the probability that he patient will be correctly classified

Authors in [11] surveyed these test statistics of different breast cancer screening tests, and their results are tabulated in **Table 4**.

Table 3. Calculation methods of test statistics as quality metrics of diagnostic tests for 95% confidence intervals (CI).

ultimately to metastasis. An important reason for the limitations using the techniques is that the contrast between the tumor and the surrounding tissue sometimes can be as low as a few percent and therefore it adds to the error of diagnostic procedure.

These and other relevant issues motivated the researchers to seek for an alternative technology which could provide better statistics and also not be harmful at the same time. This alternative technology and methodology is the use of ultra-wide band (UWB) emission and imaging system.

Diagnostic procedure	Sensitivity	Specificity	PPV	Accuracy
Mammography	67.8%	75%	85.7%	70.2%
Mammography and clinical examination	77.4%	72%	58.6%	75.6%
Clinical examination	50.3%	92%	94%	63.6%
Ultrasound	83%	34%	73.5%	67.8%
Mammography and ultrasound	91.5%	23%	72.3%	70.2%
Mammography, clinical examination, and ultrasound	93.2%	22%	72.4%	70.9%
MRI	94.4%	26%	73.6%	72.9%
Mammography, clinical examination, and MRI	99.4%	7%	70.1%	70.5%

Table 4. Contrast among different breast cancer detection modalities [11].

4. Positron emission tomography (PET)

PET is an imaging procedure that identifies the presence of cancer by using an injection mixture of radioactive materials with sugar and observes how cells react to it. The cancer cells having the characteristics to grow faster than normal cells consume nutrients. When this happens, positrons are emitted. PET makes an image by detecting these positrons. Unlike X-ray, CT, and MRI, PET can detect cancer in the very early stages. However, it has low resolution. PET scanning is combined with other techniques, e.g., PET and CT scan, for further evaluation. Therefore, PET scans cannot be used to detect small-sized tumors in the breast (in the budding stages). But they can be used for identifying the presence of metastasis, spreading to other body parts or spreading to lymph nodes.

5. Breast cancer screening using ultra-wide band (UWB)

In the last decade, the alternative technology which has been in focus of research is breast cancer detection using ultra-wide band (UWB) electromagnetic radiations, i.e., at microwave range. Microwaves provide higher and stronger contrast between healthy tissue and tumors, which supports in better tumor detection without the hazard of ionization effects. UWB microwave imaging can be done, either using microwave tomography or microwave radar imaging. The latter uses power distribution of scattered waves to distinguish between healthy and tumor-containing tissues.

Ultra-wide band (UWB) radio is no more an emergent technology, but rather the past two decades are full of experimentations with UWB for various research applications in wireless communications, radar, and medical fields.

Before the present millennia, UWB was confined totally in military applications. But, since 2002, Federal Communications Commission (FCC) has increasingly allowed the commercialization of UWB bandwidths. Federal Communications Commission (FCC) has standardized that the frequency for the UWB technique is from 3.1 to 10.6 GHz in America. However, in Europe, the frequencies include two parts: from 3.4 to 4.8 GHz and from 6 to 8.5 GHz. Applications of UWB radar in health and medicine include human body monitoring, remote sensing, and imaging. Unlikely with x-ray imaging, UWB radar uses non-ionizing electromagnetic waves which have been proved to be harmless to the human body. Additionally, the UWB radar has a very low-average power level, power efficiency, and robustness against noise. Thus, UWB is a cost-effective way of real-time human body imaging. Categorically, some other features of UWB are enumerated as follows.

Penetrating through obstacles. UWB uses RF pulses with high gain. Therefore, UWB can penetrate through walls. This makes UWB practicable for wide area presentations where obstacles are sure to be met. This uniqueness of UWB makes it feasible to image organs of the human body.

High precision ranging at the centimeter level. UWB provides an effectively precise ranging to the centimeter level because of highly short-pulse characteristics. The short UWB pulse has a very strong temporal and space-resolving capability, which is appropriate for the localization and detection in the medical diagnostic applications of tumors.

Low electromagnetic radiation. UWB also features low electromagnetic radiation because of low radiation power of the emitted pulse. According to the standards, these are less than −41.3 dBm in indoor communications. Again, the low-powered radiation effects the environment very less, which is ideal in medical diagnostic applications involving human body where organs are very close to each other.

Low processing energy consumed. As UWB utilizes very short-duration pulses, this permits the use of long-life battery-operated devices. These features are quite analogous with the wireless sensor network (WSN) nodes which essentially have to be operable under strict power control and high power efficiency.

UWB encompasses numerous utmost sought practical features for any electrical instrumentation used in medical applications. These features include noninvasiveness, low power, noncontact remote operation, biocompatibility, biological friendliness, environmental friendliness, detection, and localization. But in terms of tissue imaging, their physiological understandability by the users, high sensitivity (true-positive rate), and high specificity (true-negative rate), UWB requires more research. In this respect, the way human tissues behave with UWB waves emitted on them, i.e., their channel impulse response, is a very important aspect in the research of UWB applications in health monitoring and diagnostic systems.

5.1. UWB microwave tomography

The objective of microwave tomography is to use the inverse scattering method in finding the dielectric properties of the tissue under study. This gives a dielectric contrast of it. It produces a chart of permittivity and conductivity through inversion scattering.

In a microwave tomography breast cancer investigation system, the breast is lowered into a cylinder-shaped antenna system which covers the breast completely. Microwave measurements are then made with all possible combination of antennas, acting as both transmitter and receiver, respectively. Since the microwaves are spread, scattered, and reflected when they penetrate inside the tissue, the wave field becomes very complicated. The large amount of data generated from the extensive wave field is analyzed with a radical image reconstruction algorithm that constructs an image of the internal dielectric properties of the whole body part (tissue under examination). This detection technique depends highly on the dielectric and electromagnetic properties, which are the permittivity, conductivity, and electrical parameters of the cancerous tissue. These properties have been investigated to be much different than those of normal breast tissue [12].

Basically, the system comprises of two things: (1) transmitting and receiving antennas and (2) image reconstruction algorithm. In the measurements each antenna is operated as a transmitter as well as a receiver for every possible combination of antennas. To perform the measurements, a network analyzer with switch multiplexer module can be employed to automatically connect and disconnect transmitting and receiving antennas to the PNA. The low amount of radiated power (typically in milliwatts) is considered harmless for the patient and surrounding environment. In most of the research work, a 2D or two-dimensional image reconstruction algorithm has been used. This is most suitable for imaging 2D objects with dielectric properties that are constant in the z-direction which is taken perpendicular to the antenna plane. However, imaging a three-dimensional or 3D object, the accuracy of a 2D imaging technique is severely bounded. This means that effects would be generating in the z-axis but not being modeled using a 2D image reconstruction algorithm. Therefore, a 3D algorithm is required to accommodate all the effects. In the current systems to develop a clinical prototype, the most suitable designs consist of an antenna array where antennas are placed also outside the plane in a 3D pattern to get z-axis effects. This can be obtained by constructing a cylindrical antenna array. Together with a 3D reconstruction software, the potential for improved accuracy is optimized. However, this has significantly increased computational burden in the reconstruction algorithm.

Although the technique of microwave tomography for detection of cancers has a great potential, but still it is in the experimental stages. The clinical practice of it is still underway and has not been employed as a regular technique like other modalities discussed above. In some clinical studies, the capability to detect breast cancer tumors with microwaves has been shown. However, further clinical studies need to be undertaken in order to get a complete picture of the prospective for microwave imaging in practice. An important aspect related to breast cancer is that depending on the mixture between fatty and glandular tissues in the breast the distinction varies largely between individual patients.

5.2. UWB radar imaging

UWB microwave radar imaging rebuilds the image using the reflected wave from objects. This technique unlike microwave tomography reconstructs the scattering power distribution when microwaves are emitted on the breast and their reflected waves are analyzed. It works very much like a ground-penetrating radar (GPR). The origin dates back in 2001 by Hagness and Xu Li in Wisconsin University, USA [13]. In this context it therefore becomes very important to understand the behavior of human tissues as channel to propagate the UWB-emitted waves.

In this relevance, authors in [14] have developed an analytical body propagation model equation for human breast tissue in terms of scattering parameters toward (S_{11} or reflection

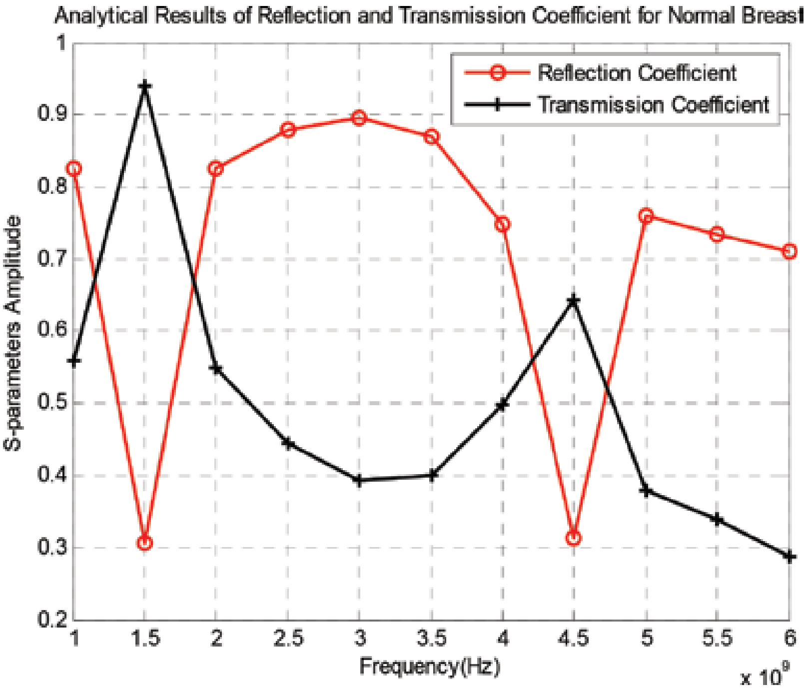

Figure 1. Trends in reflection and transmission coefficients for normal breast [14].

coefficient and S_{12} or transmission coefficient) the design goal of a suitable ultra-wide band (UWB) transceiver for early breast tumor detection. Both of these scattering parameters can be treated as channel impulse response, depending if the communication system is using reflection or transmission of waves at the receiver end. The consideration was a heterogeneous breast model comprising skin, adipose, and glandular tissues as body (breast) channel with one layer of tumor. Due to dispersive nature of heterogeneous breast, S_{11} and S_{12} varied with frequency. Modeling and simulations were performed for a 4.5 GHz center frequency UWB system. The backpropagated (reflected/scattered) signals showed approximately 63.3% higher amplitude than forward propagated signals for the breast channel with tumor. Analytical expressions were derived and formulated for S_{11} and S_{12} scattering parameters and were simulated for UWB frequency band of 1–6 GHz as shown in **Figures 1** and **2**.

In these simulations, the following interpretations can be made readily:

1. The simulations were carried out from 1 to 6 GHz.
2. Reflection and transmission coefficients show 180° out of phase at any frequency.
3. The dispersions are present in reflection and transmission coefficients. The scattering parameters are not constants but vary randomly as the frequency changes.
4. The trends are highly nonlinear. This is because the breast tissue is a nonlinear channel.
5. The concern of center frequency is very important.

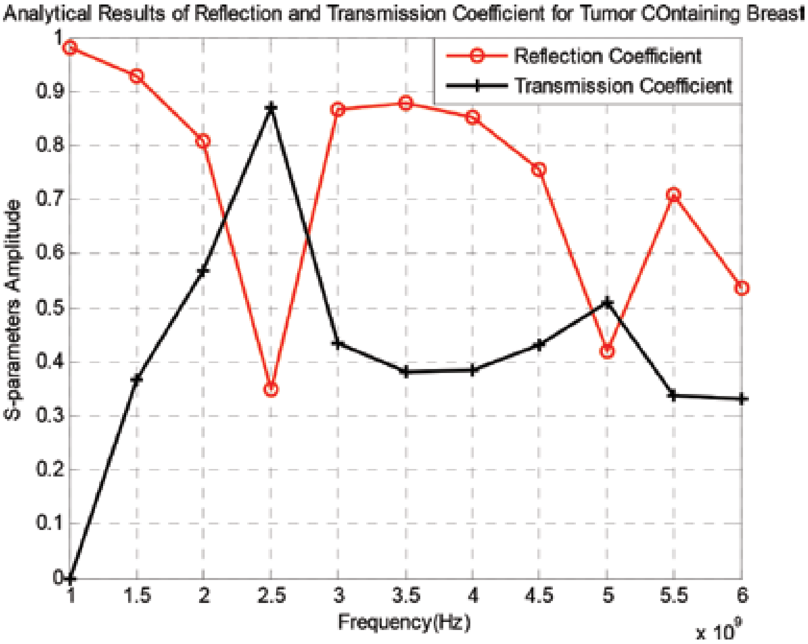

Figure 2. Trends in reflection and transmission coefficients for tumor-containing breast [14].

The simulation in **Figures 1** and **2** suggests that investigations along with the body propagation model can lead to more affirmative results to determine and predict the cancerous abnormalities in the breast. For example, at 4 GHz, the reflection coefficient of a normal breast tissue is reaching to 75%, but at the same, the frequency for a tumor-containing breast is reaching to 90%.

6. Research areas in UWB breast cancer detection

6.1. Receiver design

As discussed, screening and diagnostic testing for the presence of cancer is a probabilistic process; therefore, UWB should also have a percentage of accuracy, efficiency, and other associated probabilities. However, UWB for breast cancer detection is still not completely used for clinical testing. So, these probabilities haven’t been determined yet. But it must be well understood that increasing the true-positive rate and true-negative rate is very much dependent on the accuracy of the received signal. This puts a good responsibility on the receiver to detect the signals correctly. Hence, receiver design is very important. In this regard, two things could be catered: (1) antenna engineering and (2) inducing intelligence in the receiver to separate and classify the signals coming from normal and cancerous breast.

6.1.1. Antenna engineering and receiver intelligence

In the antenna engineering part of the UWB research, researchers have mostly employed patch antenna with their many variants and arrays of them [15–18]. Researchers have also explored many beam-forming techniques to associate them with the antenna structures (adaptive antennas) so that information could be extracted from the received signal. Researchers have used different artificial intelligence tools like neural networks and support vector machines to classify the signals coming from cancer cells and normal cells, which have proved to be very effective in the laboratory [19, 20].

6.2. Breast phantoms

When coming to experimental investigation of UWB for breast cancer detection, another important aspect is the design and development of tissue/organ phantom under investigation. The results obtained on phantoms are expected to be obtained on real tissues. Therefore, phantom making is a research-oriented subject. UWB systems need realistic phantom model tailored to the biochemical as well as morphological features of the breast tissue. Existing breast phantoms are available both in solid and liquid structures [21]. Solid phantoms as compared to liquid phantoms have the ability to hold the desired geometrical shape, thickness, and inhomogeneity as that of multilayered tissues and can be fabricated with controlled electrical properties. The concept of a thin, solid tissue phantom along with its analytical model is a challenging task and has gained attention only in the recent past. After fabrication, extraction of information from such solid phantoms requires precise characterization with respect to changes in composition for different breast density characteristics. This could be done with proper analytical model or channel impulse response of the tissue phantoms. In [22] authors have contributed toward developing a numerical model for both normal and cancerous breast tissues using finite-difference frequency techniques.

7. Conclusion

This chapter has briefly discussed about the procedures of different breast cancer screening and detection including x-ray mammography, MRI, PET, and ultrasound. These are the techniques which are clinically being used commonly around the world. However, survey showed that these testing methods do not give a very good quality measures. In this regard UWB technology for early detection of breast cancers is discussed with their two important methodologies, namely microwave tomography and UWB radars.

Although many experimental researches have been conducted, but still the clinical translation of this research is not deployed. The clinical practice of UWB will definitely produce new problems which would rectify and improve the UWB technology for screening and detection of breast tumors. But still because of the advantages that UWB has promised to provide are surly to take it a long way and unbeatable competitor against x-ray mammography, MRI, PET, and ultrasound. However, it can be seen that UWB in combination with other screening methods can prove useful in early detection of breast cancers. UWB has an advantage of being low cost, non-ionizing, and noninvasive. This makes it a human health-friendly technology.

Author details

Ikram E Khuda

Address all correspondence to: ikram@iqra.edu.pk

Faculty of Engineering Sciences and Technology, Iqra University, Karachi, Pakistan

References

[1] Khuda IE. A comprehensive review on design and development of human breast phantoms for ultra-wide band breast cancer imaging systems. Engineering Journal. 2017; **21**(3):183-206. DOI: 10.4186/ej.2017.21.3.183

[2] MARIBS Study Group. Screening with magnetic resonance imaging and mammography of a UK population at high familial risk of breast cancer: A prospective multicentre cohort study (MARIBS). The Lancet. 2005;**365**(9473):1769-1778. DOI: 10.1016/S0140-6736(05)66481-1

[3] Berg WA, Blume JD, Cormack JB, Mendelson EB, Lehrer D, Böhm-Vélez M, Mahoney MC. Combined screening with ultrasound and mammography vs mammography alone in women at elevated risk of breast cancer. JAMA. 2008;**299**(18):2151-2163. DOI: 10.1001/jama.299.18.2151

[4] Linet MS, Slovis TL, Miller DL, Kleinerman R, Lee C, Rajaraman P, Berrington de Gonzalez A. Cancer risks associated with external radiation from diagnostic imaging procedures. CA: A Cancer Journal for Clinicians. 2012;**62**(2):75-100. DOI: 10.3322/caac.21132

[5] Smetherman DH. Screening, imaging, and image-guided biopsy techniques for breast cancer. Surgical Clinics. 2013;**93**(2):309-327. DOI: 10.1016/j.suc.2013.01.004

[6] Zhao H, Zou L, Geng X, Zheng S. Limitations of mammography in the diagnosis of breast diseases compared with ultrasonography: A single-center retrospective analysis of 274 cases. European Journal of Medical Research. 2015;**20**(1):49. DOI: 10.1186/s40001-015-0140-6

[7] Abbosh YM. Breast cancer diagnosis using microwave and hybrid imaging methods. International Journal of Computer Science and Engineering Survey. 2014;**5**(3):41. DOI: 10.5121/ijcses.2014.5304

[8] Morrow M, Waters J, Morris E. MRI for breast cancer screening, diagnosis, and treatment. The Lancet. 2011;**378**(9805):1804-1811. DOI: 10.1016/S0140-6736(11)61350-0

[9] Gordon PB. Ultrasound for breast cancer screening and staging. Radiologic Clinics. 2002;**40**(3):431-441. DOI: 10.1016/S0033-8389(01)00014-8

[10] Cheng HD, Shan J, Ju W, Guo Y, Zhang L. Automated breast cancer detection and classification using ultrasound images: A survey. Pattern Recognition. 2010;**43**(1):299-317. DOI: 10.1016/j.patcog.2009.05.012

[11] Rahman A, Islam MT, Singh MJ, Kibria S, Akhtaruzzaman M. Electromagnetic performances analysis of an ultra-wideband and flexible material antenna in microwave breast imaging: To implement a wearable medical bra. Scientific Reports. 2016;**6**:38906. DOI: 10.1038/srep38906

[12] Winters DW, Shea JD, Kosmas P, Van Veen BD, Hagness SC. Three-dimensional microwave breast imaging: Dispersive dielectric properties estimation using patient-specific basis functions. IEEE Transactions on Medical Imaging. 2009;**28**(7):969-981. DOI: 10.1109/TMI.2008.2008959

[13] Li X, Hagness SC. A confocal microwave imaging algorithm for breast cancer detection. IEEE Microwave and Wireless Components Letters. 2001;**11**(3):130-132. DOI: 10.1109/7260.915627

[14] Khuda IE. Modeling and simulation of UWB wave propagation for early detection of breast tumors in cancer dielectric imaging systems. Engineering Journal. 2017;**21**(2):237-251. DOI: 10.4186/ej.2017.21.2.237

[15] Klemm M, Craddock IJ, Leendertz JA, Preece A, Benjamin R. Radar-based breast cancer detection using a hemispherical antenna array—Experimental results. IEEE Transactions on Antennas and Propagation. 2009;**57**(6):1692-1704. DOI: 10.1109/TAP.2009.2019856

[16] Gibbins D, Klemm M, Craddock IJ, Leendertz JA, Preece A, Benjamin R. A comparison of a wide-slot and a stacked patch antenna for the purpose of breast cancer detection. IEEE Transactions on Antennas and Propagation. 2010;**58**(3):665-674. DOI: 10.1109/TAP.2009.2039296

[17] Kelly JR, Hall PS, Gardner P. Band-notched UWB antenna incorporating a microstrip open-loop resonator. IEEE Transactions on Antennas and Propagation. 2011;**59**(8):3045-3048. DOI: 10.1109/TAP.2011.2152326

[18] Bahramiabarghouei H, Porter E, Santorelli A, Gosselin B, Popović M, Rusch LA. Flexible 16 antenna array for microwave breast cancer detection. IEEE Transactions on Biomedical Engineering. 2015;**62**(10):2516-2525. DOI: 10.1109/TBME.2015.2434956

[19] Singh N, Mohapatra AG, Kanungo G. Breast cancer mass detection in mammograms using K-means and fuzzy C-means clustering. International Journal of Computer Applications. 2011;**22**(2):15-21

[20] Fouda AE, Teixeira FL. Ultra-wideband microwave imaging of breast cancer tumors via Bayesian inverse scattering. Journal of Applied Physics. 2014;**115**(6):064701. DOI: 10.1063/1.4865327

[21] Joachimowicz N, Conessa C, Henriksson T, Duchêne B. Breast phantoms for microwave imaging. IEEE Antennas and Wireless Propagation Letters. 2014;**13**:1333-1336. DOI: 10.1109/LAWP.2014.2336373

[22] Khuda IE, Anis MI, Aamir M. Numerical modeling of human tissues and scattering parameters for microwave cancer imaging systems. Wireless Personal Communications. 2017;**95**(2):331-351. DOI: 10.1007/s1127

Chapter 2

Ultra-Wideband FSS-Based Antennas

Rabia Yahya, Akira Nakamura and Makoto Itami

Additional information is available at the end of the chapter

http://dx.doi.org/10.5772/intechopen.79888

Abstract

As antennas are indispensable elements in wireless systems, it is necessary to provide UWB antennas suitable for UWB systems. The most proposed UWB antennas have omnidirectional radiation, which provides the wide coverage area that is highly demanded by many conventional UWB applications. However, directional radiation is more beneficial for other UWB applications and it may even be beneficial for the conventional UWB omnidirectional applications in some environments that contain many sources of interference and distorting objects, where the omnidirectional radiation leads to high interference and loss of power in undesirable directions. Consequently, an immense research has addressed the issue of realizing UWB planar antennas with unidirectional radiation characteristics. Basically, the main technique used to create unidirectional radiation patterns is employing cavity-baking reflectors to redirect the back radiation, hence increasing the gain of the radiators. In addition, these reflectors can decouple the mounted radiator from the surroundings that can damage its characteristics. Therefore, we suggest the employment of UWB reflectors to achieve UWB planar antennas with directional radiation. Our research for designing optimal UWB reflectors has led to the investigation in the field of frequency selective surfaces (FSSs), which are valuable structures and can be of great interest to a wide range of applications especially UWB applications. Subsequently, the main aim of this chapter is to give a review of the fundamental uses of FSSs in antenna engineering and the basic physical concepts that have been employed to serve the purpose of enhancing antennas' performances using FSSs with a variety of features and characteristics. Furthermore, it is geared toward the presentation of our proposed UWB FSS-based antennas. First, we use basic FSSs such as the capacitive and its complementary inductive FSSs to design UWB reflectors that can serve improving and stabilizing the gain of UWB antennas. Thereafter, a proposed UWB single-layer FSS is used to serve the same purpose. Then, the FSS is integrated and designed together with UWB radiator, which resulted in lower profile along with good performance.

Keywords: FSS, UWB reflectors, UWB FSS, directional UWB antennas, unidirectional radiation

---

1. Introduction

The antenna is an important aspect of any wireless system. It ensures the transmission/reception of the signals and can be designed to comply with the systems' requirements, especially those with imposed regulations that must be respected such as UWB systems. Antennas are the components of the wireless communication system that are responsible for shaping and launching the emission as well as receiving the incoming radiation. As a result, the system's antennas control its coverage range and area. As the antenna directivity gets increased, its coverage area gets narrower, which may not be convenient for omnidirectional applications. Meanwhile, many real-world environments cause the distortion of the omnidirectional radiation and make it more exposed to interference with the surroundings. Hence, in these cases, the directional radiation becomes preferable, especially when it ensures a wiser use of the radiated power.

Appropriately designed UWB reflectors can bring directionality to existing UWB omnidirectional antennas, as well as shielding them from nearby metallic objects that would otherwise destroy their performance, providing them with the suitability for a variety of applications. It is obvious that planar metallic reflectors cannot provide these advantages over an ultra-wide bandwidth due to their out-of-phase reflection.

Developments in periodic structures have led to the development of planar surfaces that have, among other characteristics, the possibility to act as a perfect magnetic conductor (PMC) with in-phase reflection over a narrow bandwidth. The insertion of such surfaces enhances impedance matching, hence improving the efficiency of some antennas (e.g., printed planar antennas) when they have to be installed close to conducting surfaces, and creates a unidirectional radiation. These structures can be seen as a combination of frequency selective surfaces (FSSs) and conventional metallic reflectors. FSSs have helped to solve some crucial challenges in various fields and they have been proposed as UWB reflectors.

Furthermore, by proposing UWB FSSs, the applications of these structures can be extended to include UWB communication systems and radars or to enhance the performance of UWB components such as antennas, where UWB FSSs can be used as UWB reflectors to increase their gain and minimize their back radiation and create pattern diversity.

This chapter is a compendium of FSSs in antenna engineering that gives an introduction to how FSSs have been used in antenna fields and their potentials that can serve our purposes. Furthermore, it illustrates the principal physical concepts that can be used to explain the interaction between antennas and FSSs. Then, it itemizes the designs of the proposed FSS-based antennas using the concepts introduced in the first part.

2. Relations between FSSs and well-known structures

Some well-known structures, such as high impedance surfaces (HIS), can be considered as evolved versions of FSSs, whereas these structures combine FSSs with metallic ground planes and metallic pins (vias). Hence, they can provide two important characteristics, namely, artificial magnetic conductor (AMC) and electromagnetic band gap (EBG) simultaneously.

An FSS of metallic patches, like the one indicated in **Figure 1**(**a**), can effectively suppress surface waves because currents cannot travel across the gaps between the patches. Over the frequency range where it prohibits surface waves, it is partially reflective. It is only at very high frequencies, when the effective capacitors between neighboring plates behave as shorts, that surface waves can propagate. Hence, this FSS transmits low frequencies while reflecting high frequencies.

The complementary geometry of this capacitive FSS is the inductive one that consists of an array of square slots as shown in **Figure 1**(**b**). Since the inductive structure represents the complementary of the capacitive one, it has complementary transmission spectra. Thus, the latter transmits high frequencies while reflecting low frequencies.

For the inductive surface, the waves that are short compared to the diameter of the holes will easily fit through the mesh, while longer waves will see the sheet as continuous metal. Therefore, the sheet of metal islands transmits long wavelengths while reflecting short wavelengths. At low frequencies, where it can prevent the propagation of surface waves, the capacitive sheet is not completely reflective. Conversely, while the inductive sheet is reflective at low frequencies, surface waves can propagate easily along the continuous metal wires.

If a ground plane is added to a capacitive FSS, the structure will become completely reflective, and it will own the favorable reflection phase properties of high-impedance surfaces, but the propagation of surface waves will still be permitted. It is only when both the ground plane and the vias are included that the important properties of high-impedance surfaces, namely, in-phase, 100% reflection, and suppression of surface current propagation, are obtained [1].

2.1. FSS in proximity to a ground plane

Free-standing doubly periodic arrays of metallic elements were studied for many years in the context of FSS and their behavior is well understood. The incident polarization is assumed to be suitable to excite the metallic elements, meaning that in the case of linear dipole elements,

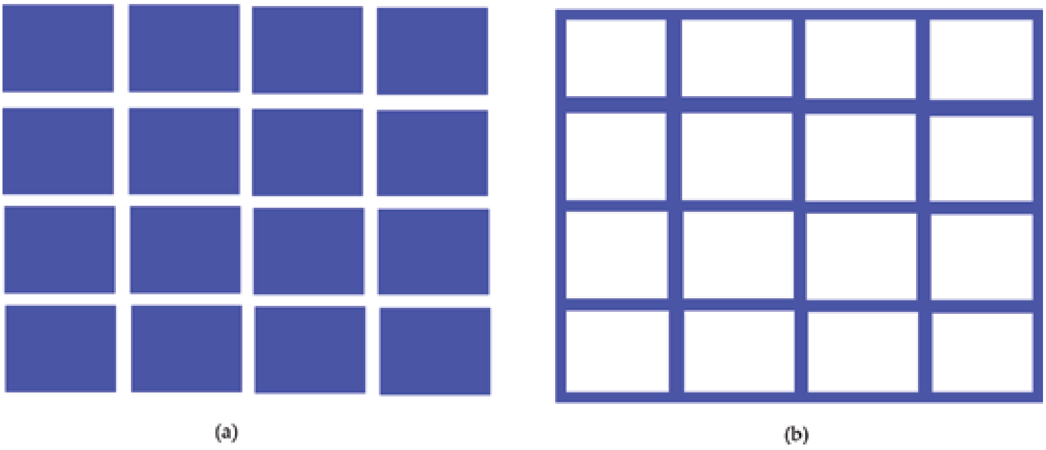

Figure 1. Complementary surfaces. (a) Capacitive surface, (b) inductive surface.

the electric field should have a component parallel to the direction of the dipoles. It is well known that at the resonant frequency of the array, the latter performs as a fully metalized screen and the incident waves are fully reflected with a phase reversal. Moreover, at resonance, the current is in phase with the incident field, i.e., the impedance seen by the incident wave is purely real, since the capacitive and inductive parts cancel each other. Also, a maximum current magnitude is excited on the elements.

For periodic arrays in proximity to a ground plane, some differences emerge. Due to the ground plane, incident waves are fully reflected at all frequencies. However, in this type of structures, careful investigation reveals that two distinct resonant phenomena occur for a normally incident wave. By assuming a free-standing array in proximity to an all-metal ground plane illuminated by a normally incident wave, the array resonance can be defined at the frequency where the currents excited on the array are in phase with the incident wave. At this frequency, the incident wave is reflected from the periodic array with a phase reverse, as in the case of the free-standing array resonance. However, it can be found that there also occurs a Fabry-Perot type of resonance at the cavity formed between the ground plane and the array. The Fabry-Perot resonance occurs at frequencies different from the array resonance. This strong cavity-type resonance excites maximum currents on the elements (which in general are out of phase with the incident wave), and the incident wave is reflected with a zero phase shift [2].

2.2. AMC resonance cavity

The presence of vias in a mushroom-type structure imposes an EBG at the same frequency range as the AMC property. In other words, the mushroom structure exhibits high surface impedance for both normally incident and surface waves at the same frequency band. Hence, at the same frequency, it reflects a normally incident plane wave with zero phase shift behaving, therefore, as an AMC and supports no surface waves behaving, therefore, as an EBG. It was demonstrated that the AMC operation is not directly related to the resonance of the FSS array. In fact, it is noticed that with varying array periodicity, the AMC band moves oppositely to the FSS resonance frequency. On the contrary, it is shown that the EBG frequency follows the trend of the FSS resonance [2].

2.3. Complementary arrays

It can be shown that the specular reflection coefficient for one array equals the transmission coefficient for its complementary array. This is a simple case of the general "Babinet's principle." Based on this observation, it is often expected that the investigation of one of the two cases is enough. However, this is in general not the case. First of all, the conducting screen must be a perfect conductor and "infinitely" thin, typically less than 1/1000 wavelength. If the screen is thick, the bandwidth of the dipole array will be larger while the bandwidth of the slot array will be smaller. Furthermore, if a thin layer of dielectric is added, the resonant frequency will be lowered somewhat for both the dipole and the slot arrays, but for a dielectric thickness of the order of $\lambda/4$ or more, the two cases behave vastly different [3].

3. FSSs in antenna engineering

FSSs' valuable features emphasized through the analysis above have encouraged their use in antenna engineering to improve antenna performance and create further properties that would not be achievable otherwise. They have been used, to widen the operating band of backing reflectors and to enhance the performance of broadband reconfigurable antennas, as superstrates and as reflectors.

3.1. FSSs as reflectors and ground planes

Extending the bandwidth of backing reflectors is among the rich utilizations of FSSs. In [4], an FSS is sandwiched between a tightly coupled array and a metallic plane, providing an additional reflecting plane for a higher frequency band. In this way, the metallic ground plane will operate at lower frequencies and the FSS will cover higher frequencies, which leads to an extended bandwidth, while the location of the metallic plane without an FSS would be suitable only for a relatively limited frequency range.

Placement of the metallic plane at a quarter wavelength distance from the antenna allows obtaining a good matching with only modest degradation of the achievable gain, but the improvement of the front-to-back ratio will come at the expense of the antenna bandwidth. The targeted application in [4] forces the integration of two frequency bands: one corresponding to the typical radar X-band, 8.50–10.50 GHz, and the other corresponding to a Tactical Common Data Link (TCDL) system, 14.40–15.35 GHz. Therefore, the used FSS was designed to be reflective at the higher frequency range and to be practically transparent for the lower band where the metallic ground plane is in charge of the reflection. More importantly, the FSS should separate the two frequency bands. Therefore, a special FSS has been chosen to serve the design purposes. The chosen element exhibits a good performance against angular variation and allows a packed lattice, with a further gain in angular independence.

In [5], a novel FSS design aimed at enhancing the performance of a broadband reconfigurable antenna has been presented. Designing FSSs' subject to phase requirements was also elaborated, revealing that some compromise, in the response magnitude, should be made to achieve the desired phase requirements. The broadband requirements also presented the need for noncommensurate FSS designs, contrary to previous FSSs that were primarily designed on the basis of the reflection coefficient amplitude and were intended for radome applications rather than substrates. When traditional broadband antennas such as log-periodic are printed on substrates, their bandwidth characteristics are altered, and one approach to regain the broadband behavior of the antenna element is to employ frequency-dependent substrates or ground planes (GPs). From here comes the suggestion of using FSSs to create substrates on which broadband antennas can be printed without affecting their broadband behavior. This can be achieved by using multiple layer FSSs as part of the substrate in a similar manner to that used for designing broadband microwave filters. Each screen is resonant at a given frequency and is placed at a distance, of a quarter of the wavelength at the screen's resonance frequency, away from the antenna's surface.

3.2. FSSs as UWB reflectors

In [6], a reflector consisting of two layers separated by an air gap of a width of 9.5 mm has been proposed. The upper layer was designed to be reflective over high frequencies of the UWB band and the second layer (lower layer) was used to reflect the transmitted waves through the upper layer. In other words, the upper layer operates as a band-stop filter for higher frequencies and a band-pass filter for lower frequencies, and the lower layer has an opposite operation.

In order to gain insights into the operation mechanism of multilayer FSS/antenna combination, a schematic describing the operating principle is presented in **Figure 2**. Two reference planes have been defined, namely, plane R and plane T. To obtain a prescribed phase variation, the dual-layer FSS has been optimized over the ultra-wide band. The upper layer, which is responsible for providing reflection at higher frequencies, is formed by a set of cross dipoles and square loops. The reflection phase from upper layer is noted by ϕ_1, ϕ_2 is the reflection phase provided by the lower layer, and ϕ_R is the overall phase reflected from the multilayer FSS at the reference plane R.

When an antenna is placed at a distance L (mm) above the FSS, the wave radiated toward the FSS is reflected. This reflected radiation would be added to the direct outgoing wave radiated

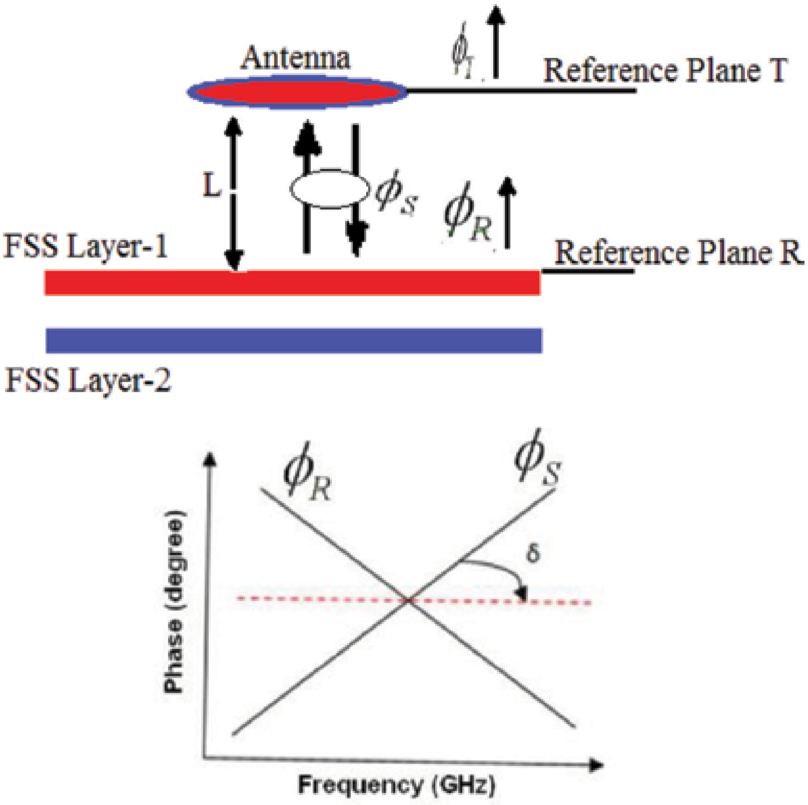

Figure 2. Operation mechanism of the dual-layer UWB reflector in [6].

from the antenna in the opposite direction to the FSS reflector. It is expected that the gain of the antenna in the presence of the FSS reflector will be maximum when the two wave components are added in phase, giving rise to constructive interference.

The evaluation of the phase at the reference plane T is described by the following equations:

$$\phi_T = \phi_R + \phi_S \tag{1}$$

where $\phi_R = f(\phi_1; \phi_2)$ at reference plane R and $\phi_S = 2 \times \frac{2\pi f}{C} L$ is the round-trip free-space propagation phase delay between the antenna and the top of the FSS reflector.

Note that, for phase coherence, ϕ_T should be zero (or an integral multiple of π) at all frequencies.

Since the phase delay is frequency dependent and increases with frequency, the ideal FSS reflection phase should decrease with frequency at the same rate, which is associated with the slope of the curve (lower plot in **Figure 2**) that is controlled by the spacing between the antenna and reflector.

Several UWB antennas have been located above this reflector to verify its functionality. In [7], the antenna was located at 10 mm, which is approximately λ/4 at the center frequency of 6 GHz, above the reflector and a maximum gain of 9.5 dBi was achieved at 4.2 GHz. The gain variation, over the frequency band from 3 to 10 GHz, was ±1.5 dB. In [8], a rectangular slot antenna, fed through microstrip rectangular patch, was employed as a radiator. An optimized height of 10 mm was chosen to separate the antenna structure from the FSS. It was revealed that the optimized UWB FSS reflector has a very small effect on the impedance bandwidth of the radiator, which is 145% with reflector and 149% without it, while the gain was significantly improved due to the reflector. The average peak gain achieved by the slot antenna alone is 5.7 dBi, while with the FSS reflector, the average peak gain is 10.9 dBi.

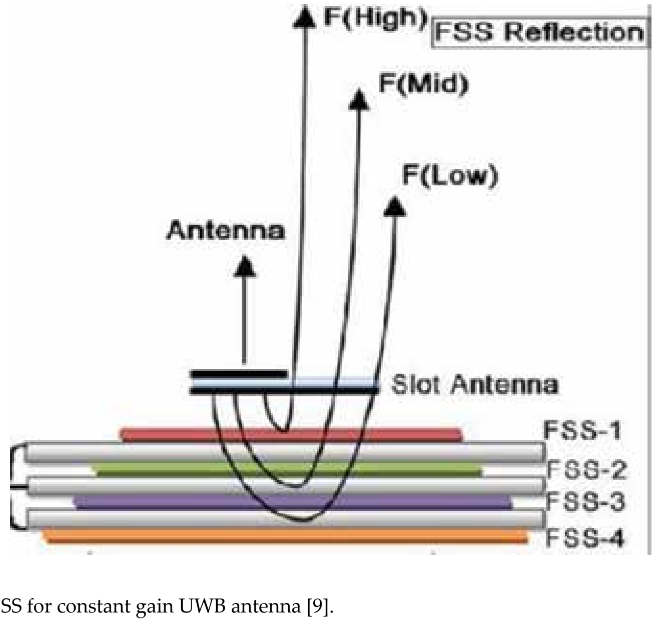

Figure 3. Multilayer FSS for constant gain UWB antenna [9].

In [9], a four-layer FSS has been used to form a UWB reflector. The four layers are separated by dielectric layers of thickness of 1.58 mm, and a UWB microstrip slot antenna is placed at a distance of 19 mm above the FSS reflector. With this structure, an average peak gain of 9.3 dB was achieved with an oscillation of ±0.5 dBi, versus an average peak gain of 4 dBi and a variation of ±2 dB of the UWB microstrip slot antenna without the reflector. **Figure 3** illustrates the structure in [9].

4. Design of FSS-based reflectors

In this section, we aim to design reflectors to be able to reflect the incident waves over the entire UWB band. A perfect electrical conductor (PEC) plane can be used as a reflector, but its performance cannot be guaranteed over a broadband frequency range as UWB band, especially over the higher frequencies. Frequency selective surfaces can be employed to alleviate this limitation as in [4]. As a result, a grounded FSS will serve as a broadband reflector. Also, this reflector needs to have a reflection coefficient that varies with frequency in a manner that stabilizes the gain of the UWB antennas over the entire operating band. Therefore, a grounded FSS with high resonance frequency is used to achieve these two features. Furthermore, a single-layer UWB stop-band FSS is designed and will be used as a UWB reflector, and its behavior will be compared with that of the other reflectors.

4.1. Grounded FSS reflector

An FSS with an array of conductors is fully reflective at resonance frequency where it acts as a metallic sheet, and it remains transparent at other frequencies. This feature of FSS with conductor array can be used to design partial reflector with a desirable reflection coefficient by choosing the location of its resonance frequency.

An FSS of conductor elements, at a high resonance frequency, is mostly transparent with a reflection magnitude that increases with frequency. After that, the transmitted waves can be reflected totally using a PEC ground plane. In this way, the grounded FSS will improve the gain of the used radiator across the entire UWB band with different amount of enhancement; hence, a constant gain can be achieved.

A grounded FSS can also be considered as a grounded dielectric slab loaded with periodic patches, which is similar to a high impedance surface with removed vertical vias. Although removing the vertical vias from HIS mushroom-like structures leads to the disappearing of the EBG, the surface waves can exist over the entire frequency band, and it has little effect on the in-phase reflection feature or AMC feature when the plane wave is normally incident, which is the main interest for our purpose.

Therefore, as a starting point, we used the initial parameters (2), suggested in [10] to analyze EBG ground planes, to design a grounded slab loaded with periodic square shape patches of width W and gap width g between the unit cells, as indicated in **Figure 4**.

$$W = 0.12\ \lambda o, g = 0.02\ \lambda o, hu = 0.04\ \lambda o, \varepsilon r = 2.20 \tag{2}$$

where λo is the wavelength at 7 GHz, which is around the center frequency of the UWB band, and hu is the thickness of the substrate of dielectric constant εr.

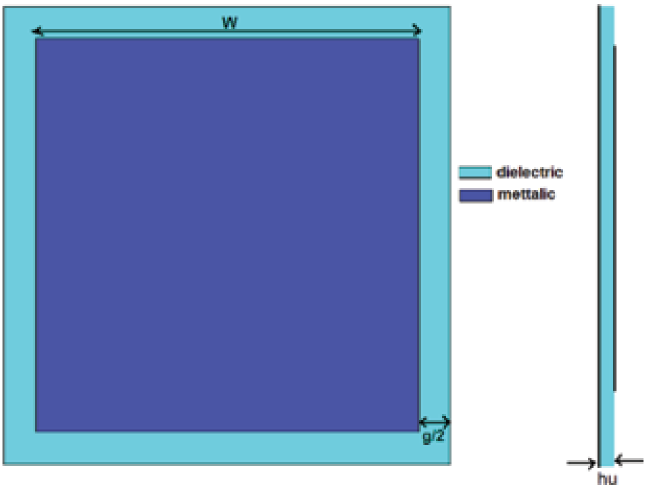

Figure 4. Structure of the FSS unit cell.

The dimensions of the unit cell control the width of the band over which the reflection phase varies between −90° and 90°, which can be called the in-phase band [10]. The choice of the used substrate is also an effective factor for enhancing the in-phase band. Therefore, we chose RT/duroid 5880, of a dielectric constant of 1.96, a dielectric loss tangent of 0.0004, and a thickness of hu =3 mm, to obtain a wide in-phase band. For the same purpose, parametric studies of both parameters W and g, around their initial values obtained from (2), were performed, from which the values that give a wide in-phase band centered at 7 GHz are selected. These values are W = 5 mm and g = 0.25 mm.

Figure 5a shows the reflection phase of the grounded unit cell with the selected parameters, computed using CST-MWS by considering the "unit cell" boundary conditions and Floquet port. From **Figure 5a**, we can see that broad in-phase band from 5.5 to 8.5 GHz, and AMC feature at 7 GHz are achieved as required.

The reflection magnitude of the unit cell without a ground plane varies, over the UWB band, from 0.3 at the lower frequency to 0.8 at the higher frequency, and it is totally reflective around 45 GHz, as shown in **Figure 5b**. As a result, the reflected amount by the ground plane is unequal, and it is proportionally decreasing with frequency. This unequal amount of transmission is the key feature to achieve a constant gain across the entire UWB, especially if the gain of the used radiator is higher at upper frequencies than it is at lower frequencies, which is the case for most UWB planar antennas.

In [9], the stability of the gain is obtained by allowing the transmission through no backed multilayer FSS, while here it is achieved by only one partially reflective FSS.

4.2. Complementary reflector

The operation mechanism of the grounded FSS reflector treated in the last subsection can be realized differently, in a manner that leads to further improvement, by using the complementary technique.

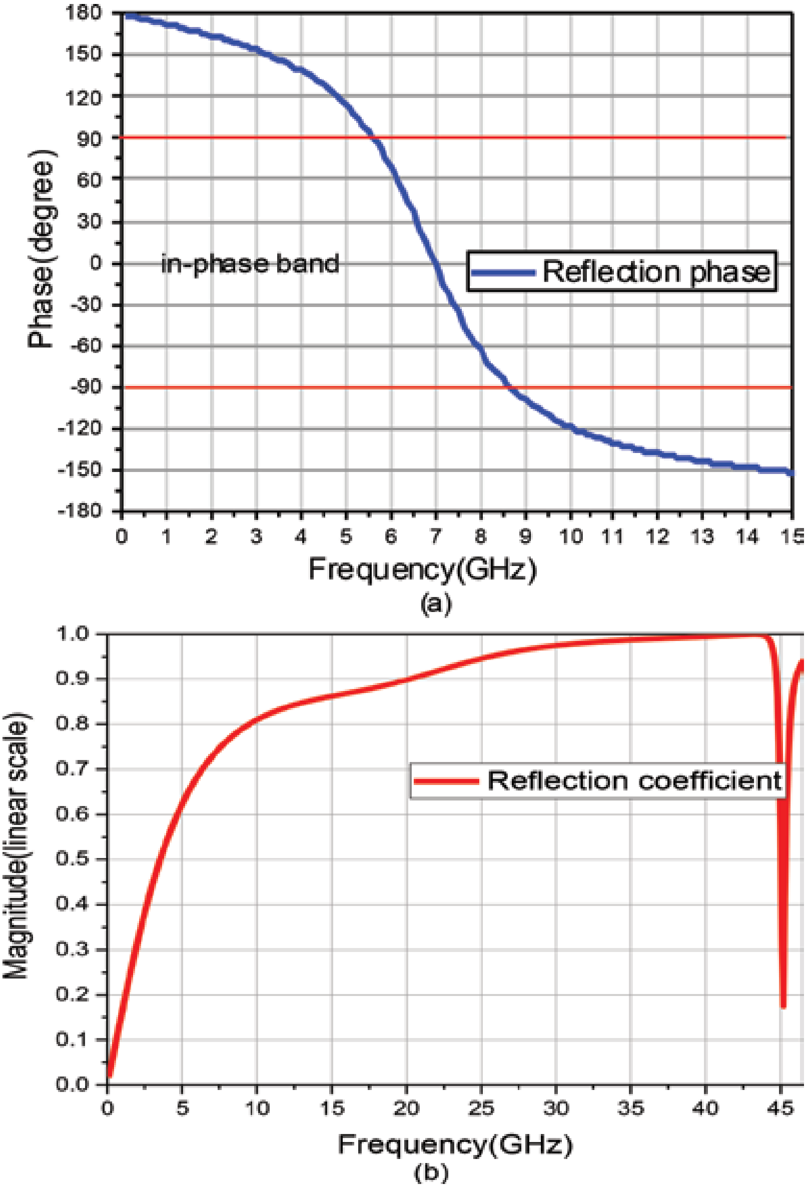

Figure 5. Reflection characteristics of FSS. (a) Phase reflection of the grounded FSS with optimized dimensions, (b) reflection magnitude of the FSS without a ground plane.

The complementary structure of the previously used FSS is an array of square slots of width Wc and metallic gap width gc, where Wc and gc have the same values as those of W and g of the grounded FSS. The complementary FSS is printed on a similar substrate to that of the grounded FSS. **Figure 6** shows the structure of the complementary unit cell as in comparison with the grounded one.

This complementary structure will have interchanged S-parameters with the original one according to Babinet's principle. As a result, a reflector with similar behavior as the grounded FSS can be obtained.

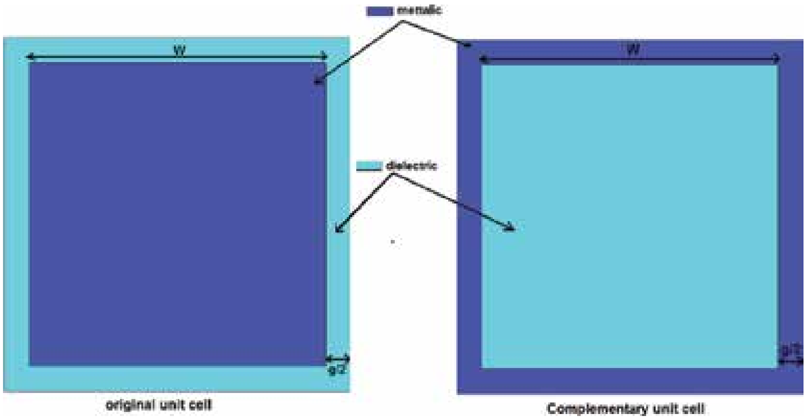

Figure 6. Structure of the complementary unit cell in comparison with the original unit cell.

While the ground plane of the grounded FSS reflects the partially transmitted waves through the square conductor unit cells, the complementary FSS operates by partially transmitting the incident waves and reflects most of them with different amount across the frequency band.

As the FSS with aperture unit cells has a high resonance frequency, its reflection magnitude decreases with frequency, which can be clearly seen in **Figure 7**. As a consequence, the amount of the transmission through the FSS will be smaller, at lower frequencies than it is at higher frequencies.

4.3. UWB FSS reflector

It has been proved, in Section 3.2 that an FSS with UWB stop-band response can serve as a good UWB reflector when it can provide linearly decreased reflection phase over the UWB band. The proposed UWB FSS offers UWB stop-band response and linearly decreased reflection phase across the UWB band; hence, it owns the ability to serve as a UWB reflector. To design an FSS with UWB stop-band response, we follow the idea of merging two structures with the ability to resonate at adjacent frequencies while their dimensions and geometries can allow them to be integrated together. So the first step is to find such structures. Loop types resonate when their circumference is approximately a wavelength that makes them a good choice for our purpose especially that their geometries are flexible enough to be combined with each other or even with other types.

The square loop resonates when its four sides' length takes a quarter of the wavelength as its value and the circular ring resonates with a diameter of $D = \frac{\lambda}{\pi}$. Hence, the square loop resonates with a total length smaller than that of the circular ring. Combining these two structures leads to the construction of a dual-band response where the lower resonance frequency is dictated by the square loop, and the higher frequency is controlled by the circular ring. The pass-band between the two resonance frequencies is governed by the distance separating the two structures. As made known in the previous section, the dielectric substrate, over which the FSS is printed, plays a vital role in determining the FSS characteristics, especially its size at resonance. Therefore, the choice of the FSS dielectric substrate can be beneficial in miniaturizing unit cell size, as a high dielectric constant substrate can reduce the size of the unit cell

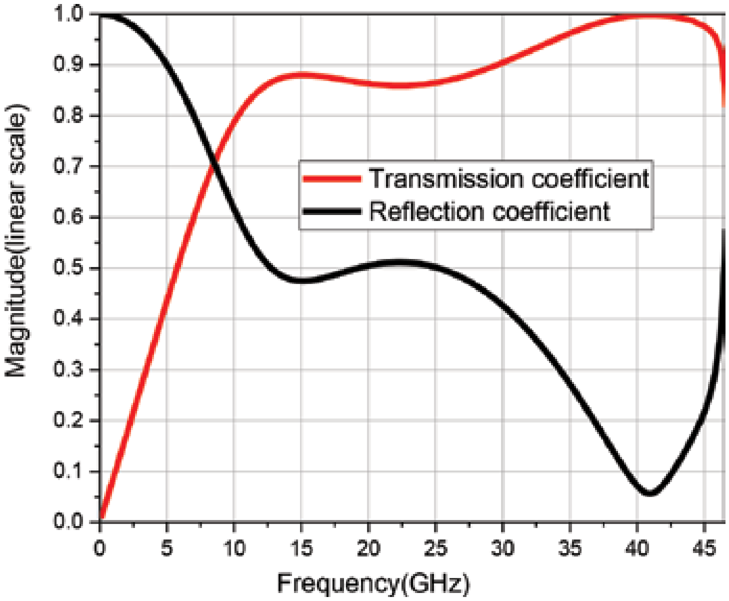

Figure 7. Reflection and transmission magnitude of the complementary unit cell.

by a factor of $1/\sqrt{(\epsilon_r + 1)/2}$ compared with a unit cell printed on a foam substrate (with dielectric constant equals unity). Consequently, RT/duroid 6010.2LM with a dielectric constant of 10.2, a tangent loss of 0.0023, and a thickness of 0.625 mm has been chosen as the dielectric substrate over which the proposed FSSs are printed.

After choosing the geometries of the FSS unit cells that serve our purpose, we need to study these unit cells using a 3D simulator for a further investigation of their behavior and how they react to the parameter variations.

It is important to mention that all the graphs presented in the next subsections are for a normal incidence. Due to the symmetry of all these FSSs, the obtained responses under TE-polarization are similar to those obtained under TM-polarization. Hence, for the sake of brevity, only the responses obtained under TE-polarization is presented.

We have studied the effects of varying the parameters of the square and circular ring unit cells, more details can be found in [11, 12], from which the design guides can be derived. Now, we shall study the effect of combining them. Although they respond to the variation of their parameters in similar ways, the square loop resonates at smaller dimensions compared to the circular ring. Consequently, for a miniaturized unit cell, the circular ring should be integrated into the square loop as depicted in **Figure 8**.

To visualize the effect of the spacing between the two elements, only "R_{out}" is varied while all the other parameters are kept constant, and the transmission coefficient is calculated for each case. The results of this study are illustrated in **Figure 9**.

As "R_{out}" increases, the resonance frequency of the circular ring decreases, approaching that of the square ring. Thus, the band-pass between the two resonance frequencies gets narrower while merging both structures results in a UWB band-stop response.

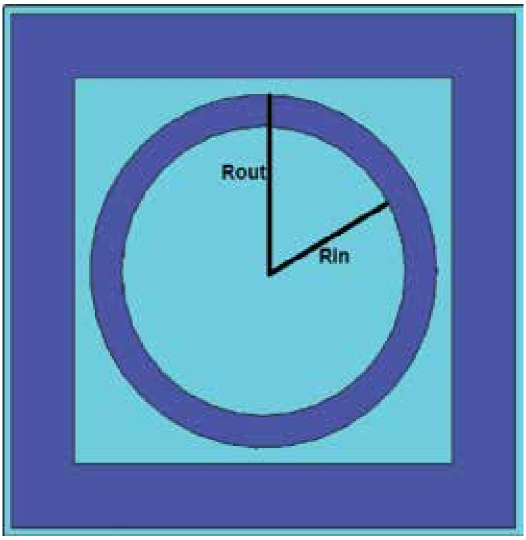

Figure 8. Circular ring inserted within square loop unit cell.

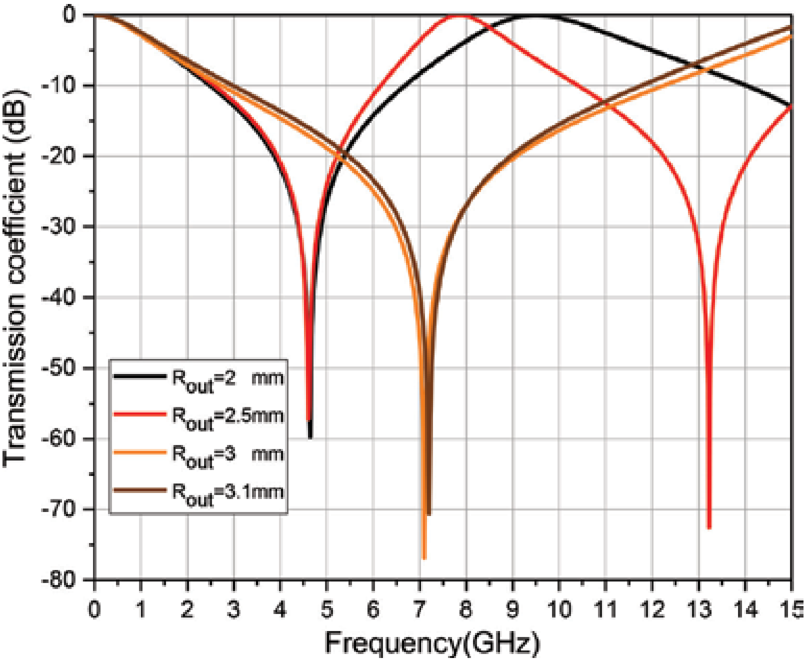

Figure 9. Parametric study of transmission coefficient for different values of R_{out}.

The results of the previous studies can help deliver a design guide of the combined UWB FSS as follows:

- The square loop resonates at smaller dimensions compared to the circular ring. As a result, the circular ring should be integrated into the square loop to obtain a miniaturized unit cell.

- The lower edge of the stop-band of an FSS, consisting of square loop unit cells, is governed by the external length of the square loop and the gap width between the unit cells; hence, they should be chosen so that the desired lower edge of the stop-band is obtained.
- After fixing the external length along with the gap width, for a desired lower edge of the stop-band, the width of the band as well as the resonance frequency can be adjusted through the variation of the internal length.
- The two element structures can be merged to obtain a UWB band-stop response.
- The outer radius of the circular ring controls the lower edge of its operating band but, in here, it also controls the spacing between the combined elements.
- The outer diameter of the circular ring should be equal or slightly superior to that of the internal length of the square loop for them to be merged.
- The inner radius of the circular ring can be used to set the desired overall upper frequency.

Taking into consideration the entire design guide mentioned above, the geometry of the proposed UWB stop-band FSS unit cell and its final parameters are illustrated in **Figure 10** and **Table 1**, respectively. It is worth mentioning that the above design guide can be generalized to implement UWB FSSs with combined elements of different geometries.

Figure 11 indicates the computed reflection and transmission coefficients of the proposed FSS. These graphs prove the ability of the proposed UWB FSS to act as a stop-band filter over a wide-band from 3 to 12 GHz, which includes the entire UWB band, with a reflection magnitude of 0 dB and a transmission magnitude less than -10 dB. At the main resonance frequency, around 7 GHz, the transmission magnitude becomes less than –75 dB. The computed

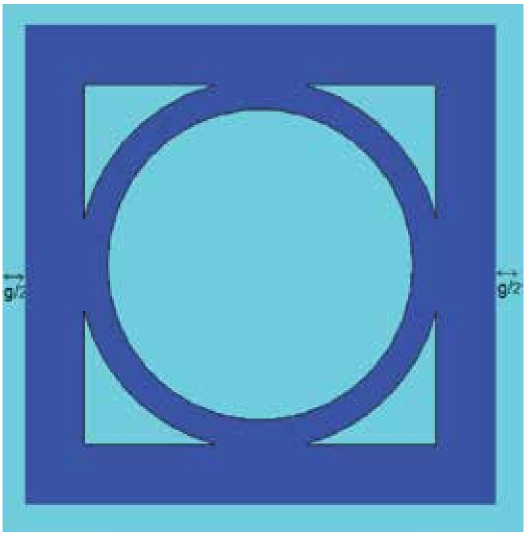

Figure 10. Structure of the proposed unit cell.

L_{out}	L_{in}	R_{out}	R_{in}	G
8 mm	6 mm	3.1 mm	2.5 mm	0.25 mm

Table 1. Final dimensions of the proposed FSS unit cell.

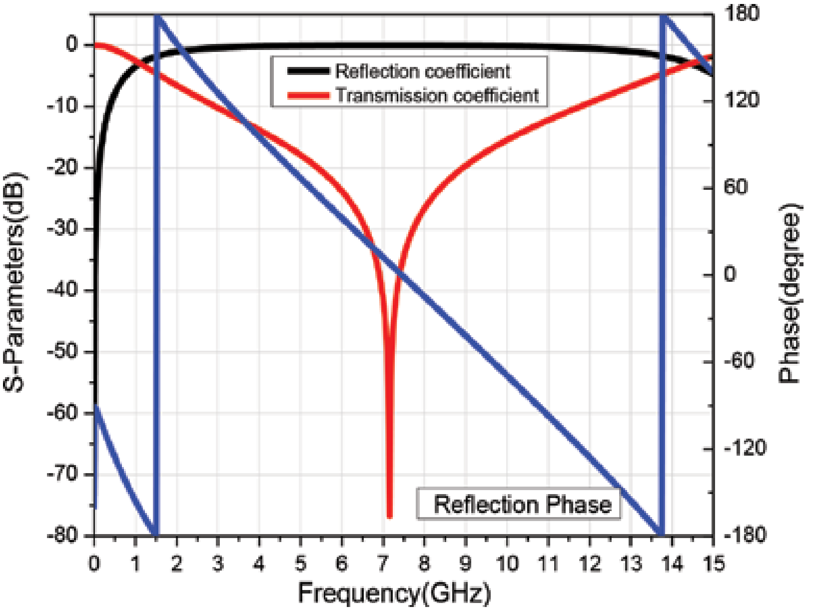

Figure 11. Reflection and transmission coefficients of the proposed FSS.

reflection phase of the FSS decreases linearly with frequency and has zero value around 7 GHz, where the transmission magnitude takes its lowest value.

The linearity of the reflection phase of the proposed FSS is satisfied across the whole band from 2 to 14 GHz. This special feature extends the recommended applications of our proposed FSS to include a variety of systems where a linearly decreasing phase is required.

5. Reflectors with UWB radiator

For better evaluation of the proposed design concept, a UWB planar antenna is used as a radiator. The original design of this UWB planar antenna has been proposed in [13]. It is a CPW-fed circular disc antenna printed on a dielectric substrate as shown in **Figure 12**. In here, the employed substrate is RO4003C with a dielectric constant of 3.38, a dielectric tangent loss of 0.0027, and a thickness of 0.508. The dimensions of the CPW line are $w_f = 3$ mm and $s_f = 0.28$, where the former is the width of the main line, the latter is the gap between the main line of the CPW and the ground plane, and ‘s’ is the slot gap between the circular patch and the ground plane.

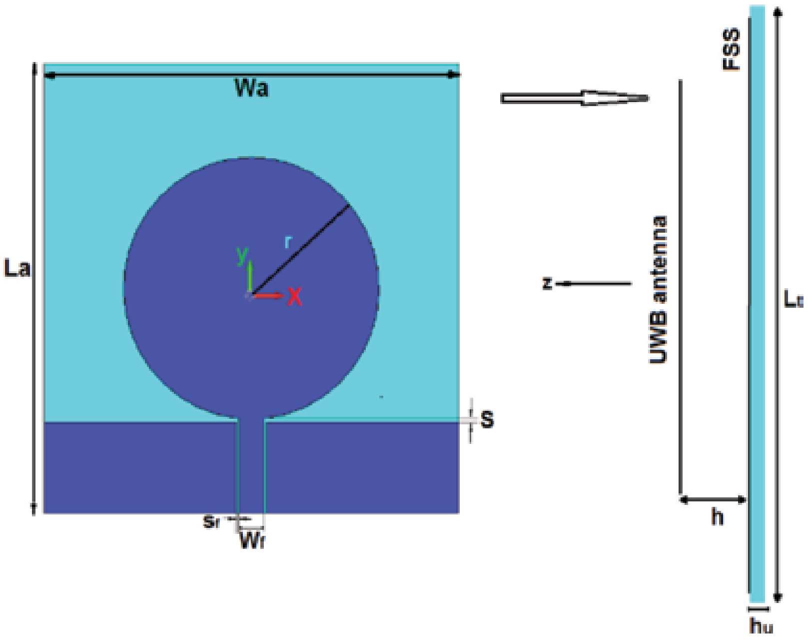

Figure 12. Structures of the used UWB antenna and the proposed structure.

The dimensions of the used radiator are illustrated in **Table 2**. The radiator is located at a distance "h" above the grounded FSS, complementary FSS, and UWB FSS, as indicated in **Figure 12**.

Many parameters affect the overall performance of the combined structures such as the distance between the antenna and the reflector and the number of the unit cells that constitute the latter.

The parameters of the grounded reflector include W, g and the number of cells n1 that is constituted of, along with the distance "h1" were optimized in terms of maximizing the operating band and minimizing the peak gain variation over frequency. Thus, the optimized values that give the best performance were selected, and they are given in **Table 2**. The dimensions of the complementary reflector are the same as those of grounded reflector.

The optimization of the grounded reflector parameters reveals that the best results are obtained when the length of the square patches is very small (W = 3 mm), which results in a higher resonance frequency compared with that associated with the initial value W = 5 mm

W	g	La = Wa	R	S	h1	n1
3	0.25	50	14.5	0.35	15.5	24

Table 2. Optimized values of the parameters of grounded and complementary reflectors along with the dimensions of the UWB radiator (in mm).

and hence, a less amount of transmission through the FSS. Moreover, it can be noted that for stabilizing the gain, the in-phase reflection should not necessarily be at the center frequency of the UWB band and that its location depends on the scattered waves from the ends of the reflectors and the different factors that set the added phase through the distance between the radiator and the reflector, which is a function of frequency.

Regarding the UWB reflector, the same dimensions of its unit cells, found in **Table 1**, were kept and parametric studies were performed to choose the best values of its distance from the radiator and the number of cells. The results of these studies are shown next.

First, the effect of the distance between the radiator and the UWB reflector on the operating band is studied through a parametric study of the reflection coefficient of the antenna for different values of "h2," as shown in **Figure 13a**. As expected, the FSS affects the matching band of the radiator as when "h2" increases, the bandwidth of the antenna increases. Furthermore, the influence of this parameter on the radiation behavior of the antenna is clearly illustrated in **Figure 13b** where the peak gain, across UWB band, is computed for different values of "h2." This points out that the gain changes differently over frequency, which can be explained by the fact that the phase shift added by h2 is a function of frequency.

As a summary, we can derive that the operating band, stability, and the value of the maximum gain of the antenna are highly dependent on how far the radiator is from the reflector.

The size of the FSS determines the overall size of the antenna. Therefore, a deep study of the effects of the installed FSS size on the provided performance was performed. The results of this study are shown in **Figure 14**. **Figure 14a** contains the reflection coefficient of the antenna for different numbers of cells (n2), which models the size of the FSS, revealing that the matching band of the antenna is mainly affected by the part of the FSS that is located directly under the radiator. In other words, when FSS dimensions exceed those of the radiator, the bandwidth of the antenna becomes independent of the FSS size.

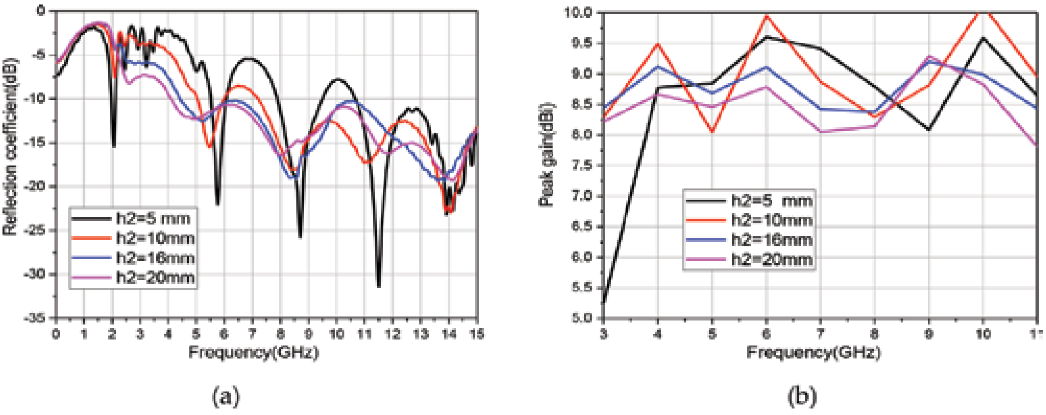

Figure 13. Parametric studies of the parameter h2. (a) Reflection coefficient, (b) peak gain.

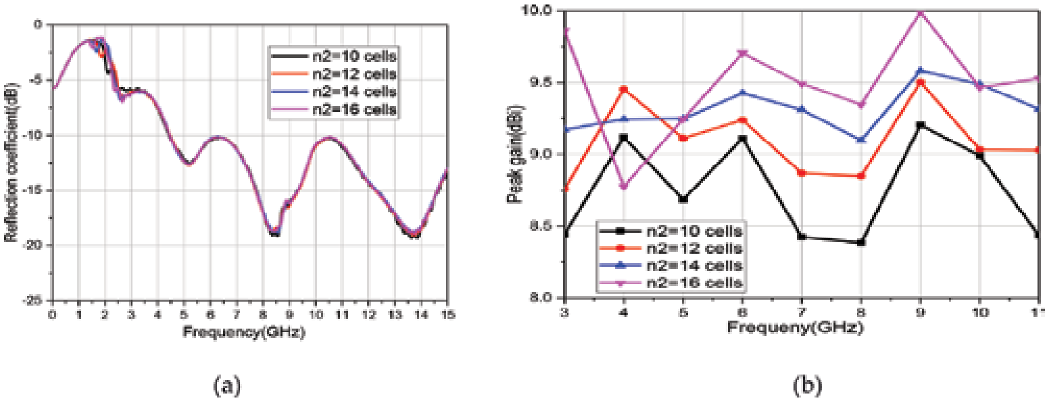

Figure 14. Parametric studies of different values of number of cells n2 of UWB reflector. (a) Reflection coefficient, (b) peak gain.

The reflective behavior of the UWB FSS is computed by considering infinite FSS dimensions, which cannot be realized in practice where finite size structures are required. However, with a large number of cells, infinite dimensions can be approximated. Nonetheless, the size of the FSS affects mainly the radiation behavior of the antenna, which is shown in **Figure 14b** through a parametric study of the antenna peak gain, illustrating that as the number of cells increases, the gain also increases over the entire UWB band. A smaller reflector can be used but at the expense of the achieved gain.

Therefore, we chose the value of “h2” that gives a wide operating band and the number of cells that is associated with high gain and minimum gain variation across the achieved band. Finally, the parameters of the structure were optimized, using CST-MWS, to achieve UWB matching band with a quasi-constant gain. The final dimensions of the UWB FSS reflector are indicated in **Table 3**.

5.1. Numerical and experimental results

The three proposed reflectors, with the optimized dimensions, along with the used radiator were fabricated and their photographs are shown in **Figure 15**.

In the three cases, the reflection coefficient of the UWB antenna and its peak gain and radiation patterns were computed numerically and measured.

It is worth mentioning that the peak gain is chosen for the evaluation rather than the gain at a specific direction because the radiation behavior of the used radiator is unstable, by nature, meaning that the direction of its mean radiation varies with frequency. Hence, the peak gain

Lout	Lin	G	n2	h2
8	6	0.25	14	16

Table 3. Final dimensions of the UWB FSS reflector used with the UWB radiator with single polarization (mm).

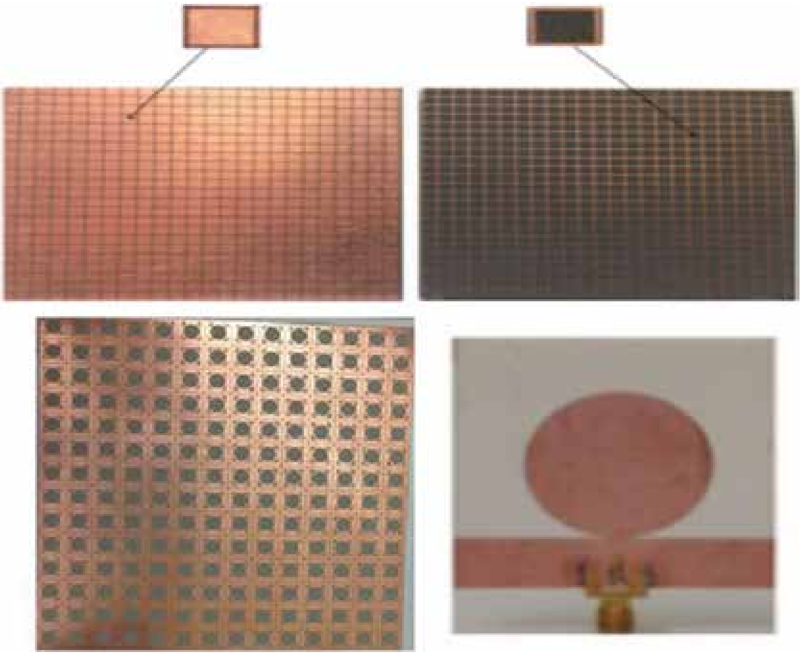

Figure 15. Fabricated prototypes.

will show, in more general way, the ability of the proposed reflectors to enhance the gain over the entire UWB band.

Figures 16–19 illustrate the final results of the simulation and measurement of the proposed designs. **Figure 16** shows the reflection coefficient of the UWB antenna mounted above the proposed reflectors, while **Figure 17** indicates the simulated peak gain over frequency, which is

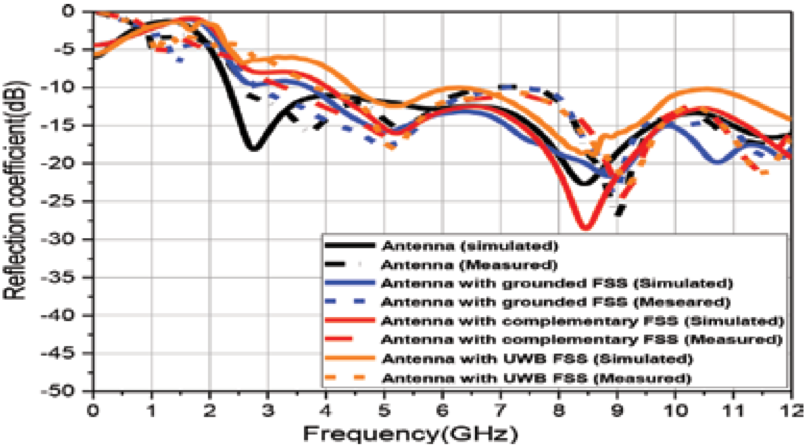

Figure 16. Reflection coefficient of UWB antenna with and without reflectors.

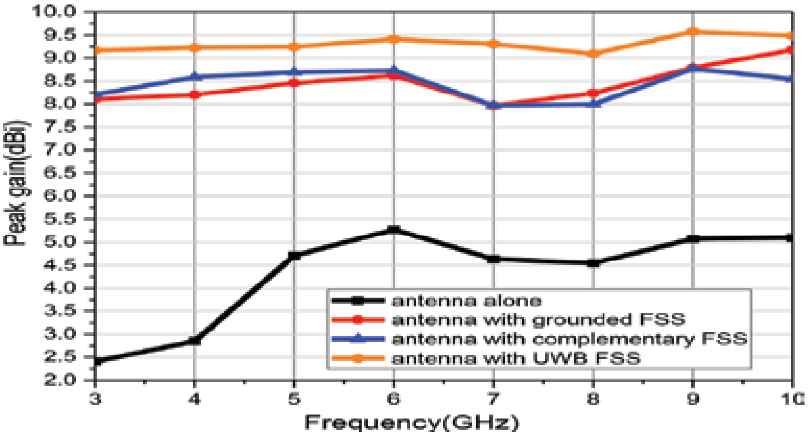

Figure 17. Peak gain of the UWB antenna with and without reflectors.

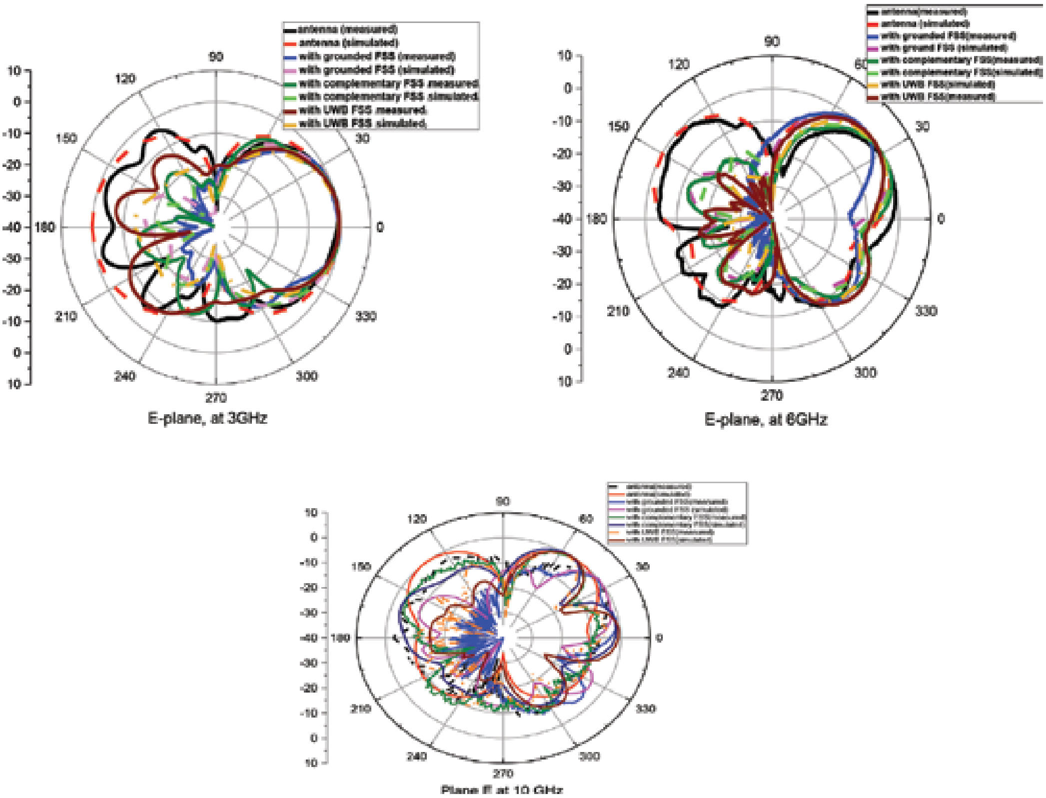

Figure 18. Radiation patterns in E-plane (YZ) at different frequencies.

extracted from the 3D radiation patterns calculated at each frequency. The direction of the maximum radiation can be shown clearer through the 2D radiation patterns, which will be shown later on. These figures also contain the corresponding results of the UWB antenna without reflectors to allow a clear visualization of the achieved improvement owing to the reflectors.

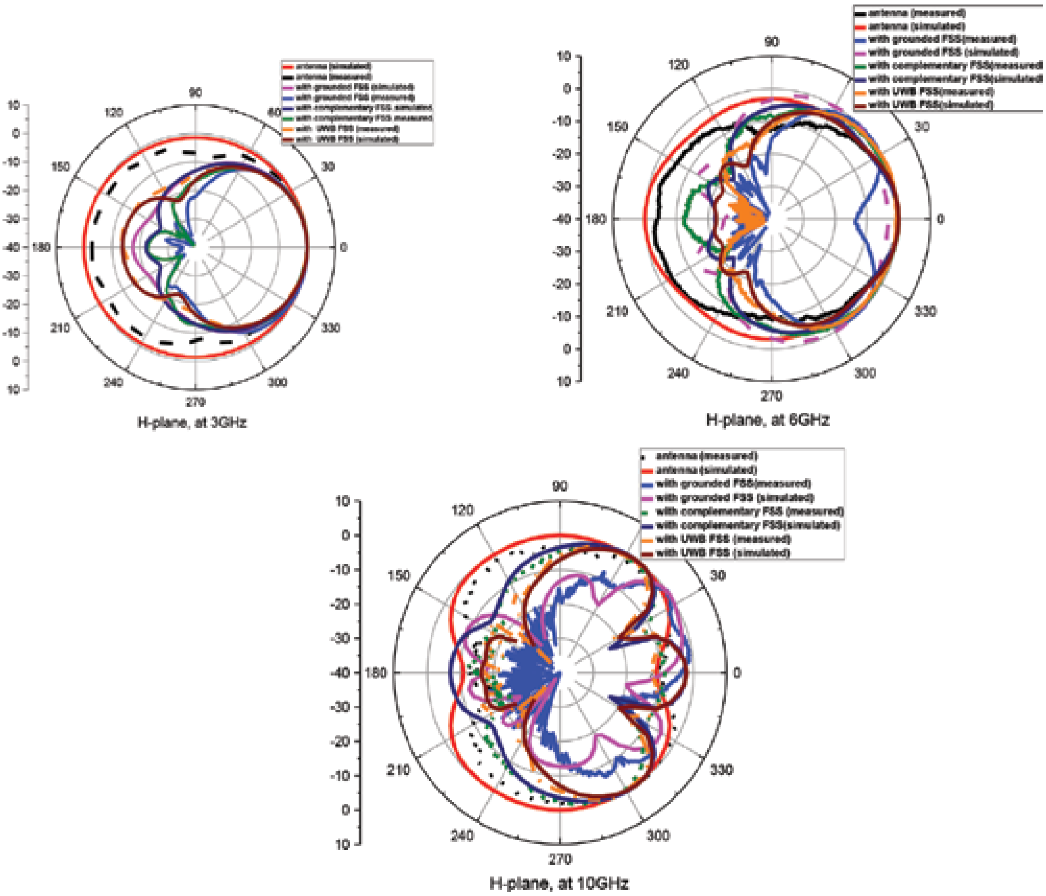

Figure 19. Radiation patterns in H-plane (XZ) at different frequencies.

These results prove that the provident choice of the different dimensions gives antennas with operating band covering the FCC authorized band from 3.1 to 10.6 GHz and an average peak gain of 8.5 dBi with a maximum variation of 0.6 dBi for the first two reflectors.

The comparison between the reflection coefficient of the radiator installed at the chosen value of h2 (h2 = 16 mm) from the UWB FSS reflector and that of the radiator alone without reflector reveals that at this height the FSS affects the matching level of the antenna, especially over the lower part of the UWB band. Regarding the gain, **Figure 17** illustrates the maximum gain of UWB antenna with and without UWB FSS. It is evident that the antenna gain is enhanced across the UWB band as a result of using the UWB FSS. The amount of enhancement varies, across the band, from 6 dBi at 3 GHz to 3.5 dBi at 10 GHz, which led to a quasi-constant gain with a maximum variation in gain of 0.7 dBi. As a result, a planar UWB antenna with enhanced quasi-constant gain is obtained.

It can also be noticed that the antenna above the three reflectors shows a similar behavior, except small differences, over the UWB band. The simulation and measurement results show an acceptable agreement.

The radiation patterns simulated and measured in E and H planes, which correspond to (YZ) and (XZ) as indicated in **Figures 18** and **19**, respectively, show the good effects of the reflectors on the radiation behavior of the antenna and confirm the gain enhancement, which is basically because of the back radiation reduction.

At higher frequencies, the radiation patterns start to be distorted with multiple side lobes due to the distortion and mean radiation tilt of the used radiator, which is a common behavior of UWB monopole antennas. However, the proposed reflectors have the ability to stabilize the peak gain despite the radiation distortion at higher frequencies, suggesting that using a more stable radiator can lead to constant and stable radiation. By taking into account their particularity and by following the proper design methodology, similar results can be obtained using other UWB monopole antennas as radiators.

Each one of the proposed reflectors has a special operation mechanism. The first one uses the ground plane to reflect the incident waves transmitted through the FSS, where the main role of the latter is to stabilize the gain by controlling the transmission over UWB band. This reflector occupies both sides of the dielectric substrate and because of the ground plane, it is fully reflective at all frequencies even those outside the UWB band. This can be inconvenient for the nearby radiators as their radiation will be blocked even if they are not sources of interference.

On the other hand, the complementary FSS, which covers only one side of the dielectric substrate, has a lower effect on the nearby radiators that operate outside the UWB band. Meanwhile, the mounted radiator will not be completely isolated from surroundings.

The third reflector gathers the best characteristics of the two previously mentioned reflectors as its structure occupies a single side of the dielectric substrate and it is fully reflective over UWB band. Hence, it will isolate the radiator from surroundings without being an obstacle for the out of UWB band radiators because it is transparent outside UWB band.

Due to the superiority that UWB FSS reflector shows, it will be used to design UWB FSS-based antenna.

6. UWB FSS-based antenna

The plane wave analysis is the most common way to study and emphasize the performance of frequency selective surfaces where the incident waves are considered planar with angles of incidence around the normal on the FSS plane. Although this analysis method is useful for most of the applications that use FSSs as radomes and space filters, it is not that much useful when the FSSs are to be integrated into the near-field zone of an antenna.

However, several references used the plane wave approach to give a design guide for the FSS-based antennas [8, 14]. On the other hand, Ref. [15] showed that the interactions between antennas and FSSs could not be sufficiently addressed without a full-wave analysis of the actual antenna structure in the presence of the FSS.

Therefore, instead of using the FSS to enhance the bandwidth of narrowband radiators as in [15] or using FSS-based reflectors to improve the gain of predesigned UWB radiators as in [8, 9] and the previous section, we follow an approach that gathers the best of all, where the UWB radiator along with the FSS is designed together to achieve UWB, low profile, and high quasi-constant gain antenna. In the previous section, the study of effects of "h2" on the matching band of the antenna showed that as this parameter increases, the bandwidth of the antenna increases. However, one should pay attention to the fact that the parameter "h2" sets the profile of the antenna and hence, a minimum value of this parameter is needed to achieve a low profile. Therefore, we set "h2" to be 10 mm, which is $\frac{\lambda}{10}$ at the lower frequency of UWB band, instead of 16 mm as in the previous section. Then, the new current distribution, over the structure of

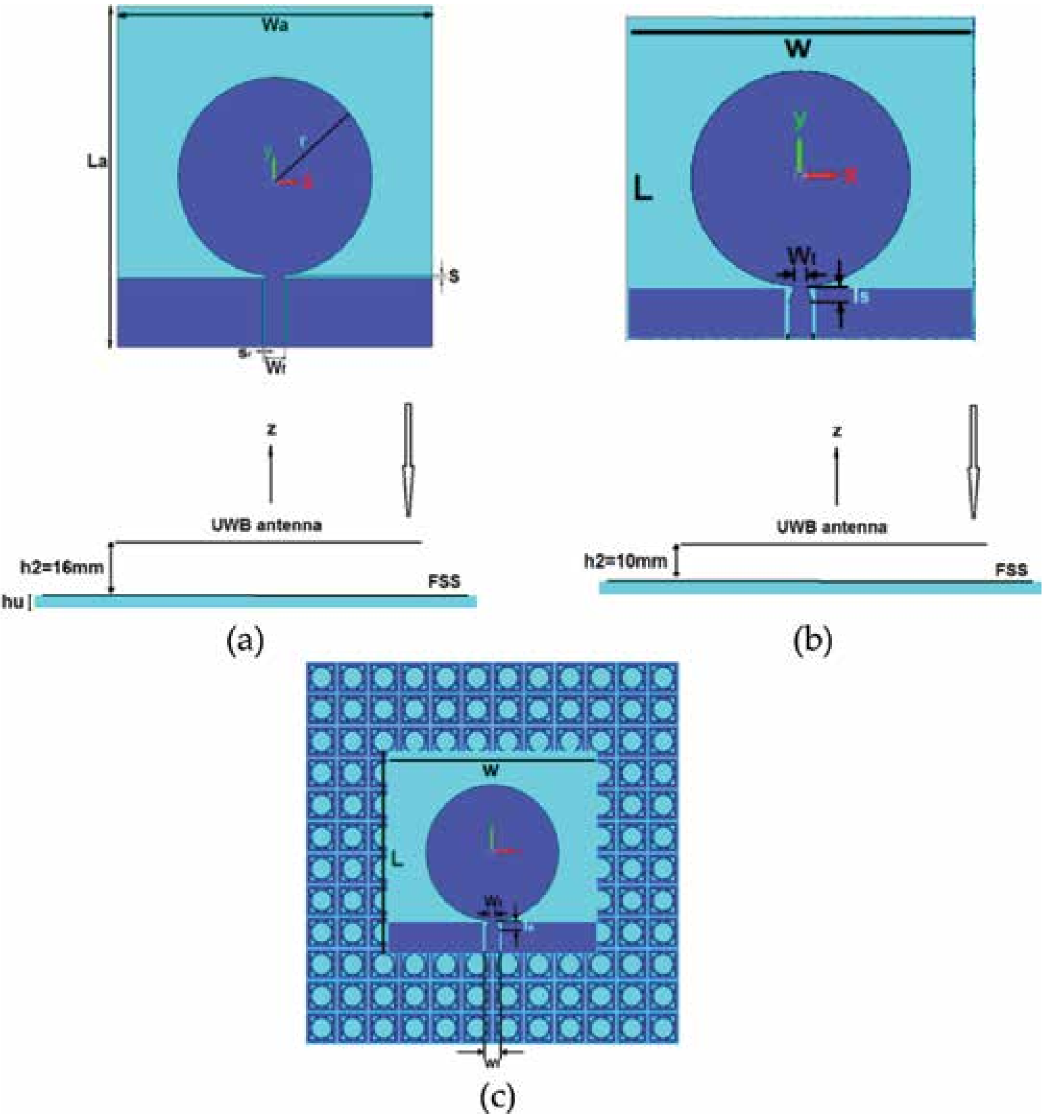

Figure 20. Proposed structure of UWB FSS-based antenna. (a) UWB antenna above UWB reflector, (b) UWB FSS-based antenna, (c) UWB FSS-based antenna (front view).

the radiator, imposed by the integration of the FSS was studied and analyzed. The previous analysis of the effect of the reflector size on the matching band of the antenna revealed that the matching band of the antenna is mainly affected by the part of the FSS that is located directly under the source. Consequently, to reduce the time of simulation, we used an FSS consisting of only 8*8 cells during the analysis process to achieve a wide operating band. Subsequently, the radiator was designed to have a wide matching band, and the reflector was designed for high and stable gain. Hence, the parameters of both structures were modified.

The structure of the proposed FSS-based antenna is illustrated in **Figure 20**. The feeding CPW line was tapered and its new parameters are defined in **Figure 20b**.

The modification of the feeding line is necessary to compensate some of the effects of the FSS on the matching band of the source antenna, especially that the tapered area has the most control on the matching band of the antenna due to the high current distribution around this area. This fact can be noted in **Figure 21** where the current distributions over the structure of the initial radiator, the initial radiator at distance 10 mm from FSS with 8*8 cells, and the redesigned radiator with FSS of the same number of cells are shown at 4 GHz. The current distributions are studied at 4 GHz because an impedance mismatch appears at this frequency when the FSS is located at 10 mm from the initial radiator.

Tapering the CPW feeding line and changing the dimensions of the structure lead to the redistribution of the current in a similar manner to that of the antenna without FSS. Also, the current distribution over the FSS is weaker around the redesigned antenna compared with that over the FSS located at 10 mm from the initial antenna.

All the main parameters that control the matching band of the monopole antenna, such as r, w, s, the new feeding dimensions, as well as the dimensions of the FSS unit cells were optimized using CST-MWS.

After finding the parameters of the radiator that give the best performance, the number of cells was parametrically studied, as shown in **Figure 22**, to select the number of cells that gives a high gain with a minimum variation through the operating band. The final optimized dimensions of the proposed antenna are given in **Table 4**.

6.1. Final results of FSS-based antenna

Figure 23 indicates the computed reflection coefficient of the proposed antenna, which shows that a reflection magnitude inferior to −10 dB is achieved along the band from 3.5 to 10.6 GHz. This matching band is obtained for overall profile thickness of 10 mm, which is around $\lambda/10$ at the lower operating frequency, which is wider than that achieved in previous section though the latter has a higher profile of 16 mm.

Regarding the radiation behavior, the peak gain of the proposed antenna and that of previous section, across the frequency, are indicated in **Figure 24**. It is clear that the proposed antenna gain is higher, over higher frequencies of the UWB band than that of the antenna with FSS reflector of the previous section, and it is lower over lower frequencies of UWB band. This is due to the size of the FSS chosen that is smaller in the latter case. However, a quasi-constant gain with a maximum variation of 0.7 dBi across the UWB band is still provided.

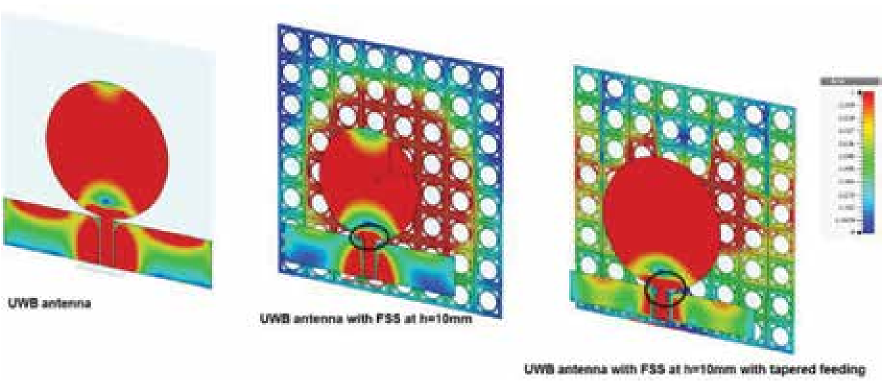

Figure 21. Surface current distribution at 4 GHz.

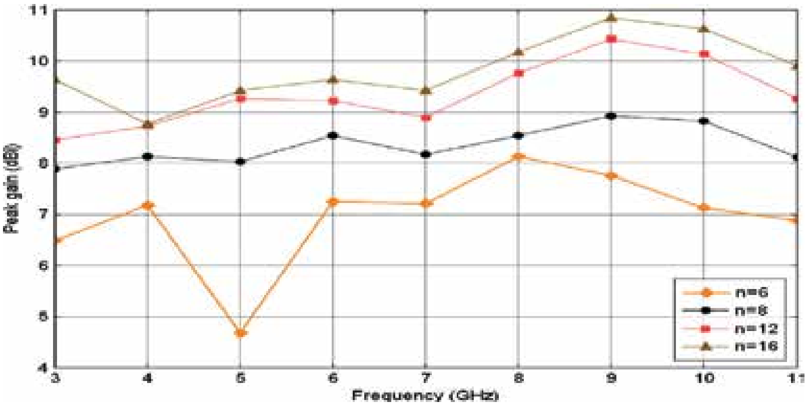

Figure 22. Gain for different numbers of cells.

L_{out}	L_{in}	R_{out}	R_{in}	G	L	W	R	Wt	Hs	N	h2
8	6	3.1	2.5	0.25	52	55	17.5	2	3	12*12	10

Table 4. Dimensions of the proposed FSS-based antenna (in mm).

Different factors such as the linearly decreasing reflection phase of the proposed FSS and the small distance between the FSS and the radiator, which cannot be obtained using a flat metallic reflector, contribute in achieving the reached high quasi-constant gain. As a result, a low profile planar UWB antenna with enhanced quasi-constant gain is obtained.

It should be mentioned that the proposed FSS reflectors through this chapter can be integrated with other UWB antennas to achieve further features such as reported in [16, 17], where a UWB dual-polarized antenna [18] was used as radiator to develop UWB FSS-based antennas with diversity operation.

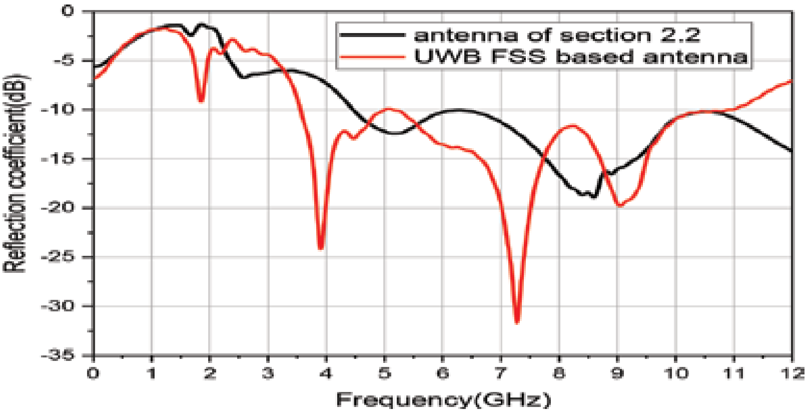

Figure 23. Reflection coefficient of the proposed antenna and that proposed in the previous section (UWB antenna with UWB FSS).

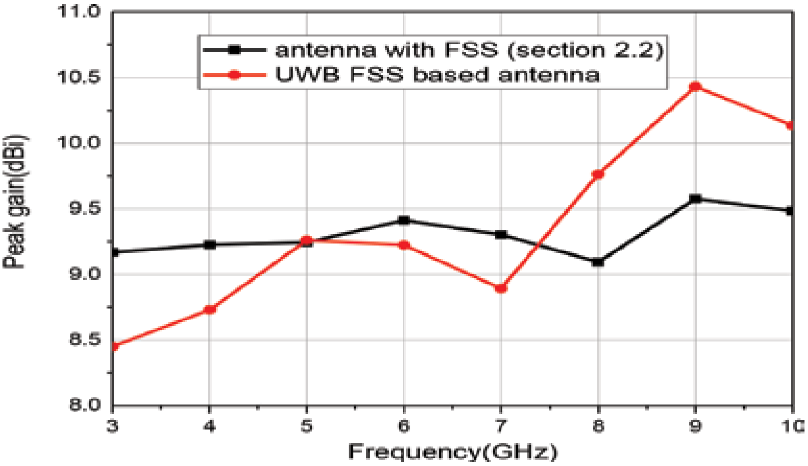

Figure 24. Peak gain of the proposed antenna and the one proposed in the previous section (UWB antenna with UWB FSS).

7. Conclusion

The elaborate examples of the different utilizations of the FSSs in antenna engineering prove without any doubt the reliability and flexibility of these structures and their ability to enrich antenna research field, which can lead to further innovations. Meanwhile, the reliability and flexibility of FSSs make them very sensitive. Hence, their design should be performed carefully to attain the desired purposes.

In this chapter, we presented a proposed technique to gradually increase the gain of UWB planar antennas over frequency by using FSSs with low-profile subwavelength unit cells, thus eliminating the restriction of the UWB planar antennas to be used only for one to multiuser applications and extending their potential applications to include the ones where constant and improved gain is required. The effectiveness of the proposed FSS-based reflectors has been proved using CPW-fed circular disc monopole as a radiator. A peak gain of 8.5 dBi with a maximum variation of 0.5 dBi across the UWB band has been achieved with a maintained wide bandwidth.

The proposed reflectors can also be of great importance for applications where the operation environment of the antennas can impact their behavior. The proposed reflectors can be used as shields to prevent the distortion of antenna behaviors. These reflectors, specially the UWB FSS reflector, can be used separately for UWB applications; therefore, a design guide of these types of structures has been proposed, which can be generalized to serve designing further UWB FSSs.

For further improvement of the UWB FSS-based antenna design, a new methodology of design was followed, which consists of designing the UWB FSS reflector and the UWB radiator together. As a result, an antenna with a small size (10*10 cm^2) and low profile of 10 mm, which corresponds to λ/10 at the lower frequency of operation, was obtained. This antenna can operate over the entire UWB band with unidirectional radiation characteristics and a peak gain varying from 8.5 to 10.5 dBi.

Author details

Rabia Yahya*, Akira Nakamura and Makoto Itami

*Address all correspondence to: rabiamintsidi@yahoo.fr

Tokyo University of Science, Tokyo, Japan

References

[1] Capolino F. Theory and Phenomena of Metamaterials. Boca Raton: CRC Press, Taylor and Francis Group; 2009

[2] Goussetis G, Feresidis AP, Vardaxoglou JC. Tailoring the AMC and EBG characteristics of periodic metallic arrays printed on ground dielectric substrate. IEEE Transactions on Antennas and Propagation. 2006;**54**(1):82-89

[3] Munk BA. Frequency Selective Surfaces: Theory and Design. New York: John Wiley & Sons Inc; 2000

[4] Pasian M, Monni S, Neto A, Ettorre M, Gerini G. Frequency selective surfaces for extended bandwidth backing reflector functions. IEEE Transactions on Antennas and Propagation. 2010;**58**(1):43-50

[5] Erdemli YE, Sertel K, Gilbert RA, Wright DE, Volakis JL. Frequency-selective surfaces to enhance performance of broad-band reconfigurable arrays. IEEE Transactions on Antennas and Propagation. 2002;**50**(12):1716-1724

[6] Ranga Y, Matekovits L, Esselle KP, Weily AR. Multioctave frequency selective surface reflector for ultra wideband antennas. IEEE Antennas and Wireless Propagation Letters. 2011;**10**:219-222

[7] Ranga Y, Esselle KP, Matekovits L, Hay SG. Increasing the gain of a semicircular slot UWB antenna using an FSS reflector. Antennas and Propagation in Wireless Communications. 2012

[8] Ranga Y, Matekovits L, Esselle KP, Weily AR. Design and analysis of frequency-selective surfaces for ultrawideband applications. EUROCON. 2011

[9] Ranga JY, Matekovits L, Weily AR, Esselle KP. A constant gain ultra-wide band antenna with a multi-layer frequency selective surface. Progress in Electromagnetics Research Letters. 2013;**38**:119-125

[10] Engheta N, Ziolkowski RW. Metamaterials Physics and Engineering Explorations. John Wiley & Sons, Inc; 2006

[11] Yahya R, Nakamura A, Itami M. Single-layer UWB FSS for enhancing the gain of UWB monopole antenna. In: 2015 IEEE International Conference on Ubiquitous Wireless Broadband (ICUWB). 2015. pp. 1-5

[12] Yahya R, Nakamura A, Itami M. Compact single-layer UWB frequency selective surface. In: AP-S/URSI 2016. 2016. pp. 957-958

[13] Liang J, Guo L, Chiau CC, Chen X, Parini CG. Study of CPW-fed circular disc monopole antenna for ultra wideband applications. IEE Proceedings-Microwaves, Antennas and Propagation. 2005;**152**(6):520-526

[14] Yang F, Rahmat-Samii Y. Electromagnetic Band Gap Structures in Antenna Engineering. UK: Cambridge University Press; 2008

[15] Foroozesh A, Shafai L. Investigation into the application of artificial magnetic conductors to bandwidth broadening, gain enhancement and beam shaping of low profile and conventional monopole antennas. IEEE Transactions on Antennas and Propagation. 2011;**59**(1):4-20

[16] Yahya R, Nakamura A, Itami M. Dual-polarized UWB antenna with unidirectional radiation. In: 2016 IEEE International Conference on Ubiquitous Wireless Broadband (ICUWB). 2016. pp. 1-3

[17] Yahya R, Nakamura A, Itami M, Denidni TA. A novel UWB FSS-based polarization diversity antenna. IEEE Antennas and Wireless Propagation Letters. 2017;**16**:2525-2528

[18] Yahya R, Nakamura A, Itami M, Denidni TA. Dual-polarized ultra-wideband antenna with improved polarization purity. ITE Transactions on Media Technology and Applications. 2016;**4**(4):363-368

Slot-Line UWB Bandpass Filters and Band-Notched UWB Filters

Xuehui Guan

Additional information is available at the end of the chapter

http://dx.doi.org/10.5772/intechopen.80004

Abstract

Slot-line ultra-wideband (UWB) bandpass filters and band-notched UWB filters are presented for UWB systems. Three types of slot-line multimode resonators are proposed and studied. Microstrip feed lines are used to realize the desired strong external coupling in a simple manner. By properly allocating the resonant modes of resonator and external coupling, UWB bandpass filters have been realized. Next, microstrip resonators, i.e., open-loop resonator, stub-loaded dual-mode resonator, and triangular dual-mode ring resonator, are loaded to the slot-line; notched bands are realized in the UWB passbands. The design methodology has been verified by the measured results.

Keywords: stepped-impedance resonator, notch band, stub-loaded resonator, slot-line resonator, multimode resonator

1. Introduction

Ultra-wideband (UWB) technology is strongly desired in high-speed transmission systems. Since the US Federal Communications Commission (FCC) authorized the unlicensed use of UWB devices in 2002 [1], research on UWB components such as UWB bandpass filters (BPFs) becomes a hot spot. Many methods have been proposed to design various UWB bandpass filters (BPFs) including multimode resonators (MMRs) [2] and stub-loaded resonators [3, 4]. To achieve the desired external coupling, extreme narrow gap between microstrip resonator and I/O feed lines is necessarily needed, which increases the difficulty of manufacturing. To keep the gap width in a moderate scale that can be realized easily by using PCB process, an aperture-backed parallel-coupled microstrip line with enhanced coupling degree is constructed to allocate the coupling peak [5, 6]. For the indoor and handheld UWB systems, the

FCC required that the UWB bandwidth must be strictly contained between 3.1 and 10.6 GHz. However, there is a need to avoid the interference from existing wireless communication systems such as wireless local area network (WLAN) in 5.2-GHz band. Generating a notch band in a UWB BPF is an effective and feasible method to solve this problem. As usual, an external resonator is used to create a notch band in the core of the UWB BPF at the cost of enlarged size [7]. In [8, 9], a stepped-impedance resonator (SIR) is embedded to achieve a band-notched characteristic without increasing the circuit size. Band-notched filtering effect was achieved by adding a meander line slot to reject the undesired WLAN radio signals [10]. In [11], two spurline sections are employed to create a sharp band-notched filter for suppressing the signals of 5-GHz WLAN devices. In [12], a dual-mode fractal defected-ground structure (DGS) bandstop filter is realized and connected with MMR; band-notched characteristics are realized. To avoid the interference of the wireless local area network (WLAN) at 5.25 and 5.775 GHz, two different quarter-wavelength lines are arranged on the ground of UWB BPF to generate dual narrow stopbands [13]. Obviously, combined bottom layer and top layer can make fully use of the circuit board, increasing the coupling between resonator and feed line, while keeping the circuit size [14].

In this chapter, slot-line multimode resonators are studied and applied in UWB BPFs. Microstrip feed lines are used to realize the desired external coupling in a simple manner. Microstrip resonators, such as open-loop resonator, stub-loaded dual-mode resonator, and square ring dual-mode resonator, are loaded to the slot-line; notch bands are realized in the UWB passbands.

2. Open-loop resonator-loaded slot UWB filter

2.1. Stepped-impedance slot-line UWB BPF

A diagram of the original UWB BPF using stepped-impedance slot-line resonator is shown in **Figure 1**. A multimode resonator is realized by using the stepped-impedance slot-line on the ground plane. By setting the impedance ratio and the length of the slot-line resonator, the first three resonant modes are equally allocated in the UWB passband. In other words, the

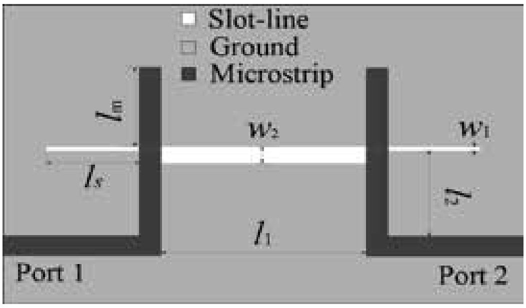

Figure 1. The schematic of original UWB filter using stepped-impedance slot-line resonator.

central resonant frequency of the multimode slot-line resonator is determined by the length l_1; the location of first and third resonant frequency is determined by the width ratio w_2/w_1. l_s is approximately $\lambda_g/4$ of slot-line in center frequency, and l_m is approximately $\lambda_g/4$ of microstrip line in center frequency. To decrease the return loss in the passband of UWB, the coupling must be very strong, and microstrip feed lines are placed right on the top and orthogonal to the slot-line resonator.

2.2. Band-notched UWB filter

To effectively decrease the interference between UWB system and WLAN system, a notch band shall be produced in the UWB band. To avoid the size increment of the circuit, the open-loop resonator is placed right on the top of stepped-impedance slot-line resonator, and the circuit volume can be fully used. **Figure 2(a)** shows the physical layout of an open-loop resonator-loaded slot-line. Frequently used structures for creating notch band include conventional open stub, spurline, embedded open stub (EOS), and open-loop resonator (OLR). **Figure 3** provides a comparison of transmission characteristic at 5.25 GHz between these methods. Open-loop resonator can produce the sharpest notch band, and conventional open stubs produce the widest notch band. The spurline and embedded stub do not increase the size of the circuit, while open-loop resonator and conventional open stub may increase the circuit size. With respect to that, the WLAN passband is quite narrow, the transition band shall be very sharp, and the open-loop resonator is preferred.

The microstrip open-loop resonator provides a bypass for the signal at its resonant frequency, and a notch band is produced. The resonant frequency of the open-loop resonator is approximated by

$$f_1 = \frac{c}{2\sqrt{\varepsilon_{eff}}(4a-g)} \tag{1}$$

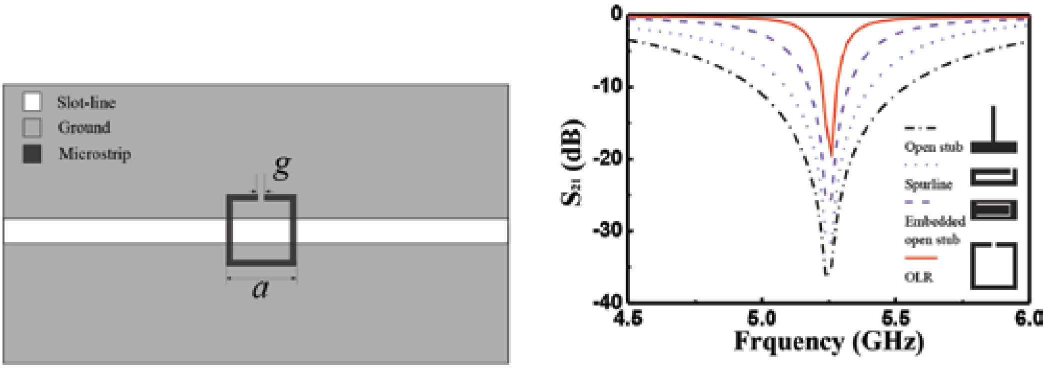

(a) (b)

Figure 2. (a) Open-loop resonator-loaded slot-line resonator and (b) simulated frequency responses of the four frequently used structures.

where *c* is the speed of light in vacuum, ε_{eff} is the effective dielectric constant, and *a* and *g* are the side length and the gap width of the microstrip open-loop resonator, respectively.

2.3. Experimental results and discussions

A UWB BPF with notch band is designed based on the abovementioned method. To further increase the attenuation of the notch band in the UWB band, two microstrip open-loop resonators are loaded to the slot-line resonator. By proper setting the position of the two open-loop resonators, a narrow notch band can be achieved in the UWB passband. The layout of the proposed notched UWB BPF is shown in **Figure 3(a)**. **Figure 3(b)** illustrates a full-wave

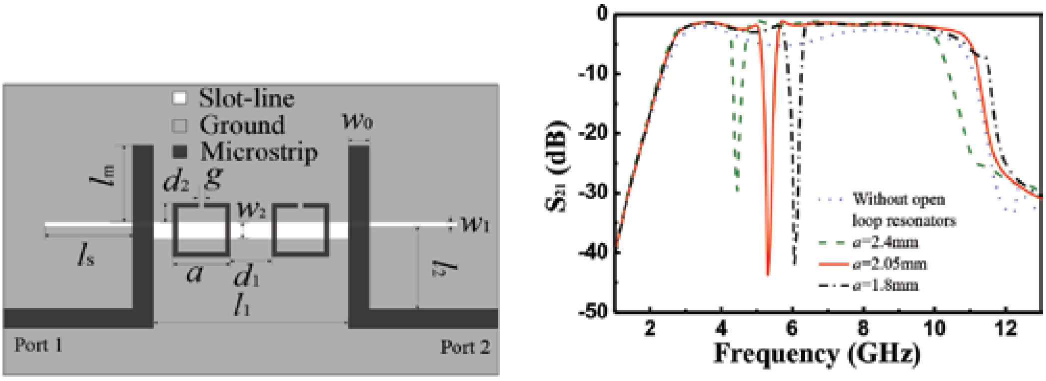

(a) (b)

Figure 3. (a) Layout of the proposed band-notched UWB BPF using open-loop resonator-loaded stepped-impedance slot-line resonator and (b) simulated result of the band-notched UWB BPF with varying *a*.

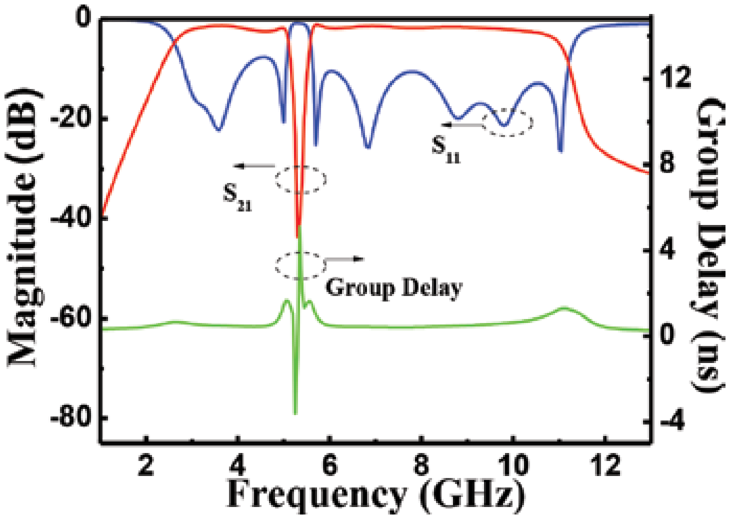

Figure 4. Measured frequency responses of proposed band-notched UWB BPF using open-loop resonator-loaded stepped-impedance slot-line resonator.

simulated result of the location of notch band against the side length *a*. Increment of slot-line width will increase the insertion loss in the passband. It is also observed that loaded microstrip open-loop resonator produces a notch band and decreases the insertion loss in the passband.

The UWB bandpass filter with improved performance is designed, fabricated, and measured. A substrate with relative dielectric constant of $\varepsilon_r = 4.5$ and a thickness of h = 0.8 mm is used in the design. The parameters of the proposed filter in **Figure 3** are $l_1 = 12$ mm, $l_2 = 5.6$ mm, $l_s = 6.2$ mm, $l_m = 5.9$ mm, $w_0 = 1.5$ mm, $w_3 = 0.2$ mm, $w_4 = 1.2$ mm, $w_r = 0.2$ mm, $d_1 = 1.9$ mm, $d_2 = 1.55$ mm, $a = 4.1$ mm, and $g = 0.2$ mm. Measured frequency responses of the filter are plotted in **Figure 4**. The results exhibit attractive UWB bandpass behaviors in the 3.1–10.6-GHz band; the narrow notch band locates in 5-GHz band. Its insertion is greater than 29 dB and the 3-dB bandwidth is about 300 MHz. The insertion loss is about 1.2 dB at the center frequency of 6.85 GHz. The group delay is below 2 ns within the passband.

3. UWB BPF with three-stub-loaded slot-line multiple mode resonator (MMR)

3.1. Three-stub-loaded slot-line UWB BPF

Figure 5 shows the configurations of the proposed UWB BPF with three-stub-loaded slot-line MMR. Three-stub-loaded slot-line MMR is fed by microstrip feed line. The MMR and the feed lines are folded and orthogonal coupling is applied.

The slot-line MMR consists of a stepped-impedance resonator and three loading stubs, with one located at the middle of the resonator. Compared with traditional SIR and stub-loaded resonator (SLR), the proposed one has more degrees of freedom to control its resonant frequencies. Once the original parameters of the slot-line resonator are determined, EM solver is invoked to tune the structure to achieve an optimized characteristic. **Figure 6** depicts the simulated transmission characteristics of the resonator with and without additional stub. The solid line and dashed line indicate the transmission characteristic of the resonator with and without additional stub, respectively. Additional stub increases the electrical length of the stub, and an additional resonant mode is shown in the UWB frequency range.

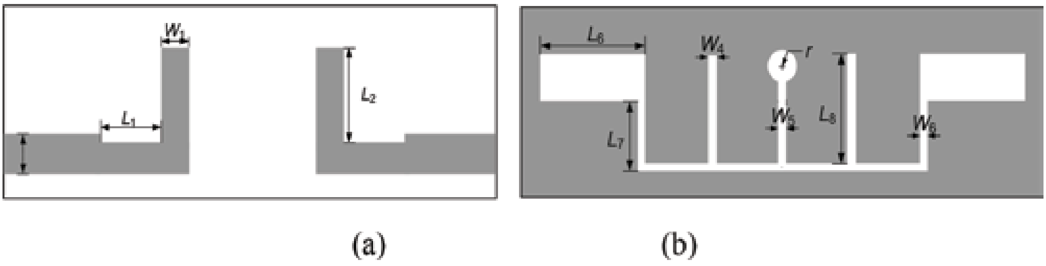

Figure 5. Configurations of the proposed UWB filter with three-stub-loaded slot-line MMR. (a) Top view and (b) bottom view.

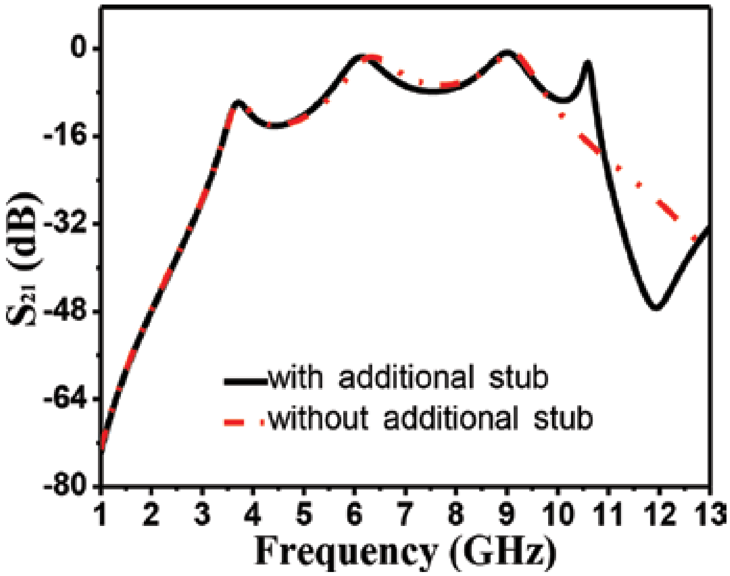

Figure 6. Characteristics of the slot-line MMR with and without the additional stub.

Next, the influence of two parameters of the resonator on the resonant mode of the resonator is studied. **Figure 7** shows the variation of resonant-mode frequencies against L_8, length of the stub, and r, radius of the additional stub. As can be seen from **Figure 7**, four resonant modes (i.e., f_1, f_2, f_3, and f_4) are created in the studied frequency range, which are applied to generate the UWB transmission characteristic. **Figure 7(a)** shows the variation of resonant mode against the length of the stub. As L_8 increases from 2.8 to 4.8 mm, f_3 drops from 10.5 to 8 GHz, and f_4 drops from 11.5 to 10 GHz, which are located in the UWB range, while f_1 and f_2 keep almost unchanged. **Figure 7(b)** depicts the variation of resonant-mode frequencies against the radius of the additional stub. As r increases from 0.4 to 1.0 mm, f_1, f_2, and f_3 remain stationary, while f_4 drops from 12.5 to 10.5 GHz. These resonant frequencies are basically related to the stepped-impedance resonator, and some ones also can be separately controlled by tuning the loaded stubs, which shows great convenience in relocating the required resonant modes of the resonator.

3.2. Band-notched UWB BPF

Based on the UWB filter mentioned above, a notch band is produced and a band-notched UWB BPF is designed. **Figure 8(a)** illustrates the circuit model of a dual-mode resonator-loaded slot-line, where the white section indicates the slot-line, the gray part is the ground, and the black one is a microstrip dual-mode resonator. Equivalent circuit of dual-mode resonator-loaded slot-line is provided in **Figure 8(b)**. Two resonant modes of the stub-loaded resonator are coupled to the slot-line, providing a bypass for the adjacent signal of its resonance. The degree of separation of two modes determines the bandwidth of the notch band, and the coupling between resonator and slot-line influences the amplitude of the attenuation.

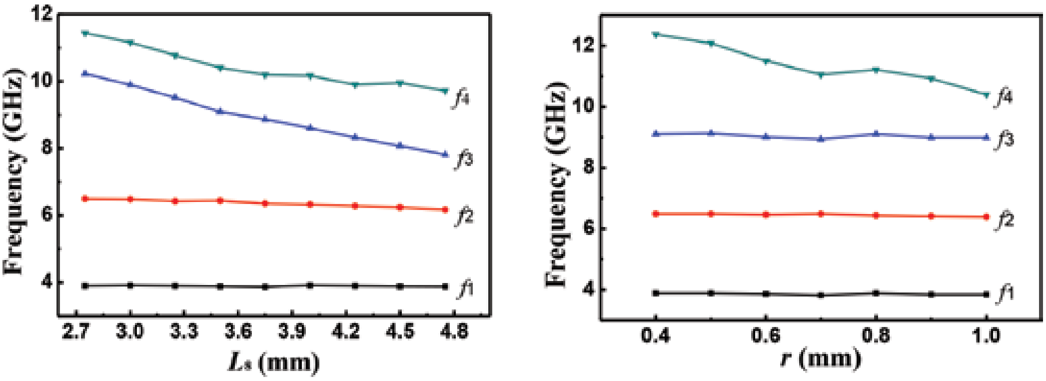

(a) (b)

Figure 7. Resonant-mode frequencies against (a) L_8 and (b) r.

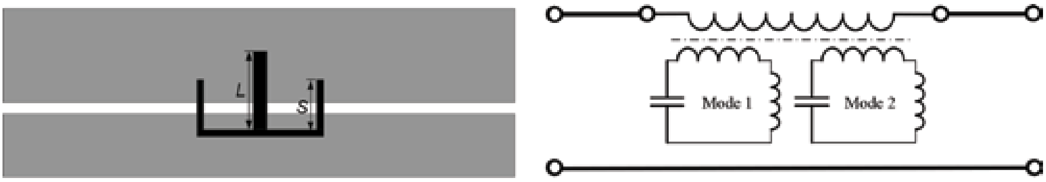

(a) (b)

Figure 8. Dual-mode microstrip resonator-loaded slot-line. (a) Structure and (b) its equivalent circuit model.

EM solver is invoked to analyze the relationship between the parameters and the transmission characteristic of the bandstop filter. **Figure 9(a)** shows the transmission characteristics of the resonator versus *L*, the length of the loading stub. When *L* increases from 4.5 to 6.0 mm, the lower resonant mode keeps unchanged, and the higher mode decreases from 3.06 to 2.84 GHz.

As we all know that the bandwidth of the bandstop filter is determined by the separation of two poles and the band position of the bandstop filter can be adjusted by the length of the stub *L*, a transmission pole is also created, which is located near the lower transmission zero, sharping the transition band. **Figure 9(b)** illustrates the effect of varying S on the two modes of the dual-mode resonator. When *S* increases from 3.0 to 4.5 mm, the bandwidth of the filter increases from 60 to 480 MHz, and the central frequency decreases from 4.6 to 4.2 GHz. Obviously, modifying *S* and *L* can change the position and the bandwidth of the stopband.

3.3. Filter implementation and results

Based on the proposed structure, a UWB BPF with notch band from 5.15 to 5.35 GHz is designed and fabricated. The feed lines and the MMR in slot-line are folded and orthogonally coupled to acquire the desired strong coupling. A dual-mode loaded-stub open-loop

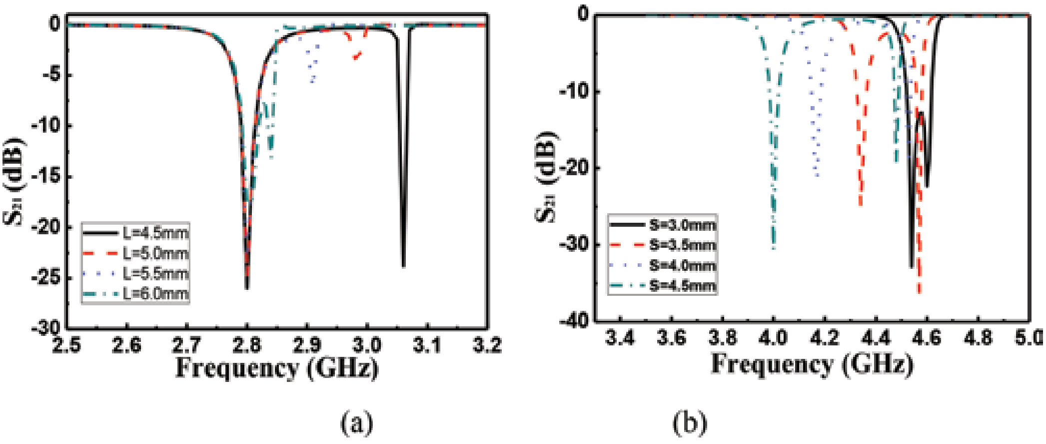

Figure 9. The transmission characteristic of the simplified resonator with varied parameters. (a) L and (b) S.

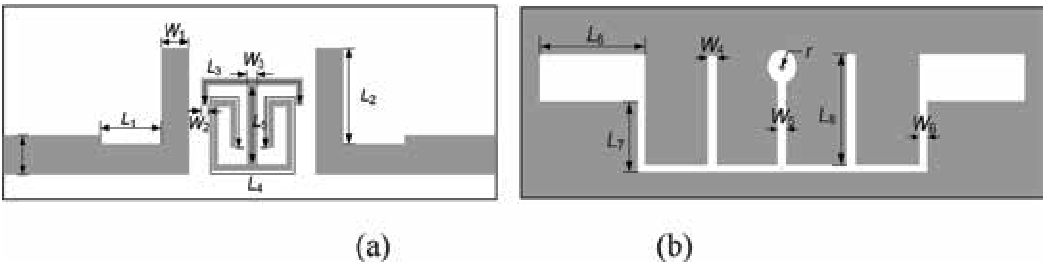

Figure 10. Configurations of the proposed band-notched UWB BPF using dual-mode microstrip resonator-loaded three-stub-loaded slot-line MMR. (a) Top view and (b) bottom view.

resonator is loaded to the slot-line, and a notch band for WLAN is produced, as shown in **Figure 10**. The dual-mode resonator is folded in order to improve the slow-wave effect for miniaturization. A substrate of 28 mm × 18 mm with a relative dielectric constant of $\varepsilon_r = 3.5$ and a thickness of h = 0.8 mm is used in the design. Finally obtained parameters of the filter shown in **Figure 1** are $W_0 = 1.80$ mm, $L_1 = 3.80$ mm, $L_2 = 4.70$ mm, $W_1 = 1.50$ mm, $L_3 = 8.00$ mm, $W_2 = 0.30$ mm, $L_4 = 17.40$ mm, $W_3 = 0.60$ mm, $L_5 = 3.70$ mm, $W_4 = 0.50$ mm, $L_6 = 3.80$ mm, $W_5 = 0.30$ mm, $L_7 = 2.50$ mm, $W_6 = 0.30$ mm, $L_8 = 3.50$ mm, and $r = 0.55$ mm. Measurements are performed by using vector network analyzer AV3926.

A comparison between the simulated and measured results is shown in **Figure 11**, where the solid lines and the dashed lines indicate the EM-simulated results and measured results, respectively. Simulated results show that the 3-dB bandwidth of the filter covers from 3.1 to 5.15 GHz and from 5.35 to 10.6 GHz, while the measured ones show that the 3-dB bandwidth covers from 3.2 to 5.15 GHz and from 5.35 to 10.6 GHz. Simulated and measured insertion losses of each passband are about 2 dB; return losses are −12 dB/−18 dB and − 18 dB/−10 dB. Return loss in the notch band is greater than 15 dB. Except for the deviation that may be caused by the fabrication, the simulated results agree well with the measured results.

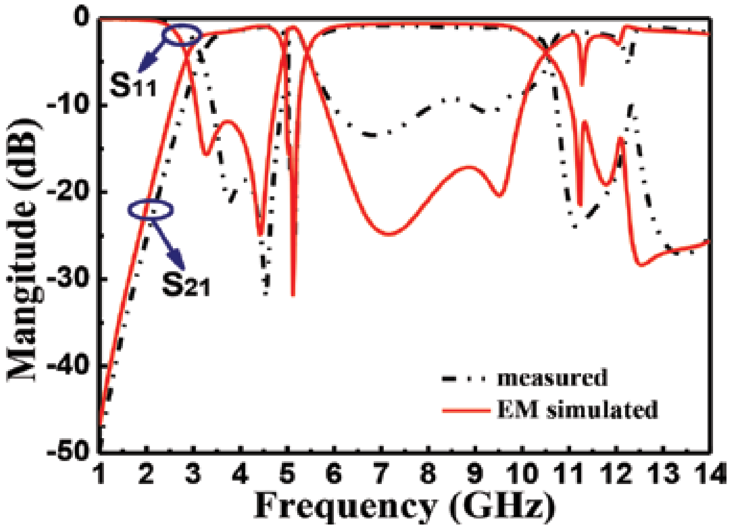

Figure 11. Comparison between measured and EM-simulated results of the band-notched UWB BPF.

4. Triangular loop-loaded band-notched UWB filter

4.1. Dual-stub-loaded slot-line MMR

Two stubs are symmetrically loaded to slot-line, which forms a dual-stub-loaded slot-line MMR, as shown in **Figure 12(a)**. Because the proposed slot-line MMR is a symmetrical structure, even-odd mode theory can be applied to analyze its resonant characteristics. **Figure 12(b)** and **(c)** gives equivalent circuits of the slot-line MMR.

Under odd-mode excitation, the symmetrical plane can be seemed as short-circuited, and its resonant condition can be derived as

$$Z_B \tan\theta_B \tan\theta_C + Z_B \tan\theta_B \tan\theta_A + Z_A \tan\theta_A \tan\theta_C = 0 \tag{2}$$

where Z_A and Z_B and θ_A, θ_B, and θ_C are the characteristic impedance and electrical length of the dual-stub-loaded MMR, respectively.

Under even-mode excitation, the symmetrical plane can be seemed as open-circuited, and its resonant condition can be summarized as

$$Z_A \tan\theta_A + Z_B \tan\theta_B = Z_B \tan\theta_A \tan\theta_B \tan\theta_C \tag{3}$$

Resonant modes of the resonator can be controlled and allocated according to the requirements by changing the parameters of the resonator.

To have a clear knowledge of slot-line resonator, resonant characteristics of the dual-stub-loaded slot-line resonator are performed by invoking the 3D EM simulator. Resonant modes

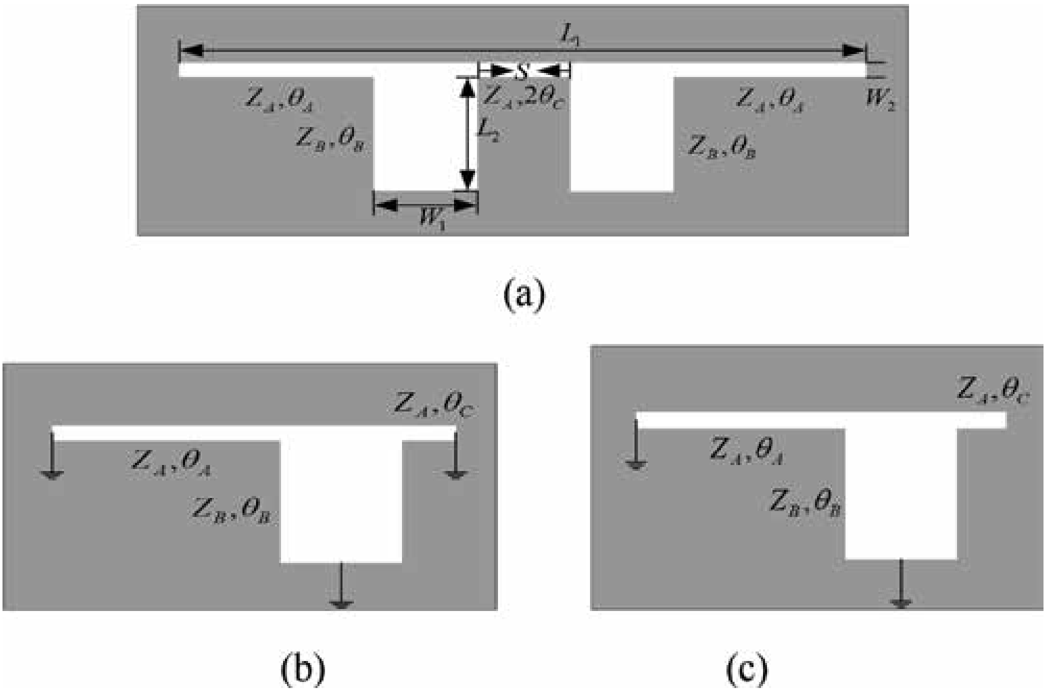

Figure 12. (a) Dual-stub-loaded slot-line MMR and its equivalent circuits: (b) odd mode and (c) even mode.

of slot-line resonator against S, L_1, and L_2 are plotted in **Figure 13**, where f_1, f_2, and f_3 indicate the first, second, and third resonant modes of resonator, respectively. When S increases from 0.2 to 2.2 mm, f_3 decreases from 9.6 to 8.2 GHz, while f_1 and f_2 shift slightly. When L_1 increases from 23 to 25 mm, both f_1 and f_2, together with f_3 decrease steadily. When L_2 increases from 1 to 6 mm, f_2 drops from 8.2 to 6.5 GHz, f_3 drops from 13.5 to 8 GHz, and f_1 keeps unchanged. Obviously, three resonant modes of the resonator can be designed intuitively and well set in the UWB passband.

4.2. Ultra-wideband BPF using dual-stub-loaded slot-line MMR

Layout of a proposed UWB BPF is depicted in **Figure 14**, which is constructed by a slot-line resonator and two microstrip feed lines. On the bottom layer, a dual-stub-loaded slot-line resonator is formed firstly, where two identical stubs are symmetrically loaded to a uniform slot-line resonator. **Figure 15** illustrates the frequency responses of the slot-line UWB BPF with different lengths of feed line (L4) under all the other sizes fixed. When the slot-line resonator is fed under weak coupling case with L_4 = 4.8 mm, three resonant modes with peak S21 magnitudes are observed at about 4.08, 6.41, and 9.5 GHz, respectively. As L_4 increases to 10 mm, the S21 magnitude realizes an almost flat frequency response over a UWB passband. After its sizes are slightly adjusted, an UWB frequency response is satisfactorily realized. Under the use of this hybrid microstrip/slot-line structure, the desired strong coupling between feed lines and MMR can be easily achieved by properly selecting the relative position between them.

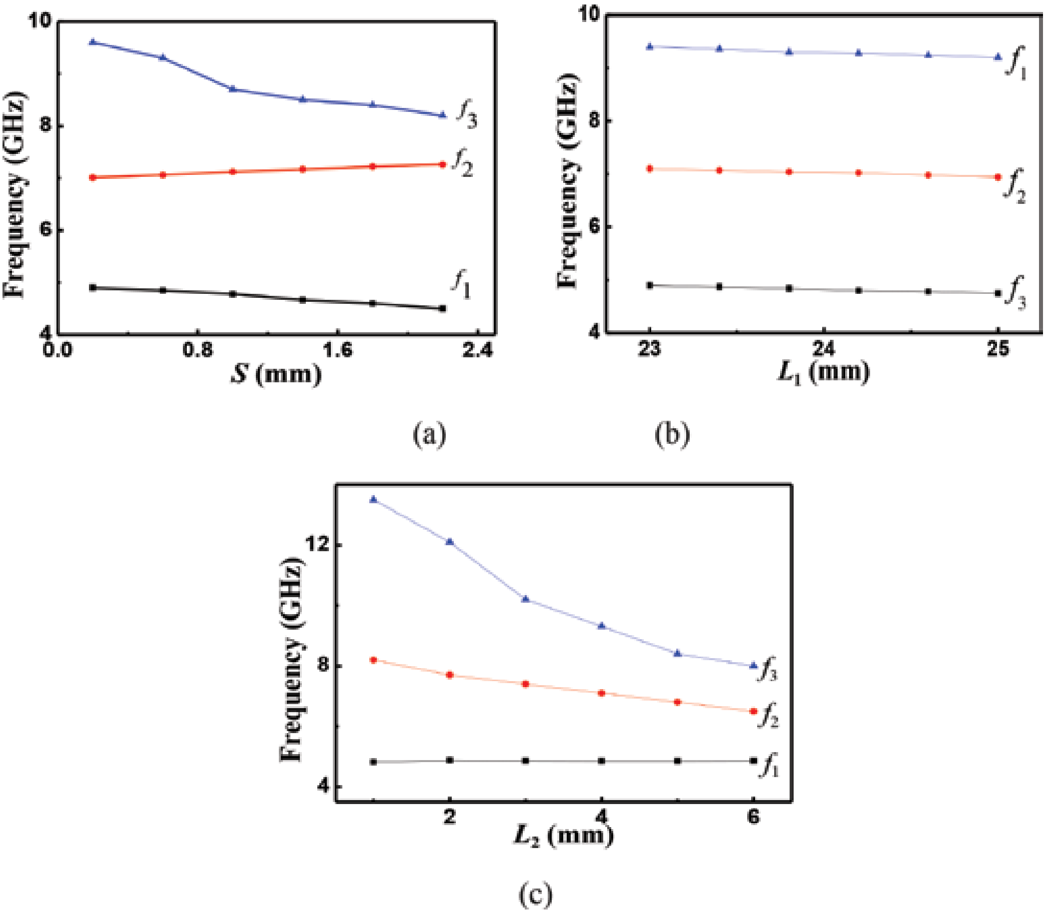

(a) (b)

(c)

Figure 13. Resonant modes of dual-stub-loaded slot-line resonator with fixed W_1 = 2.0 mm, W_2 = 0.3 mm, and varied (a) S (L_1 = 23 mm, L_2 = 3 mm), (b) L_1 (S = 0.6 mm, L_2 = 3 mm), and (c) L_2 (S = 0.6 mm, L_1 = 23 mm).

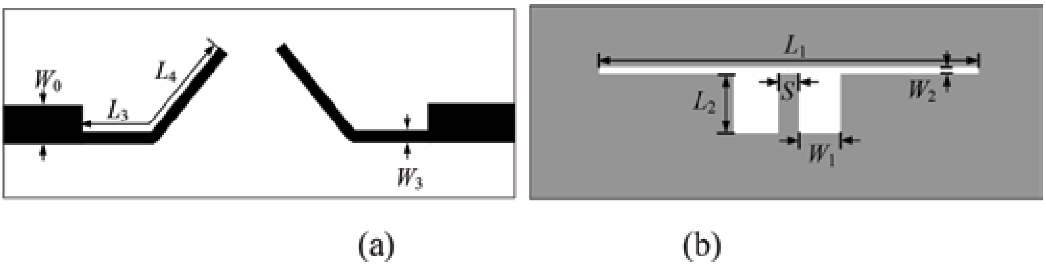

(a) (b)

Figure 14. Schematic of the UWB BPF using dual-stub-loaded slot-line MMR. (a) Top layer and (b) bottom layer.

4.3. Realization of notch band

Considering the fact that the above-achieved UWB passband range may interfere with the existing wireless systems such as wireless local area network (WLAN), a notch band may be highly demanded in various practical applications. For this purpose, a microstrip dual-mode triangular loop resonator is formed on the top layer of a dielectric substrate and loaded to the dual-stub-loaded slot-line MMR.

Figure 16 depicts the geometry, equivalent circuit model, and simulated frequency response of a slot-line loaded with back-sided microstrip triangular loop resonator, respectively. **Figure 16(a)** shows a simplified circuit geometry of the structure, where the white portion indicates the slot-line and the black ones are microstrip feed lines and a dual-mode triangular loop resonator with perturbations. Its equivalent circuit model is given in **Figure 16(b)**. Coupling between dual-mode resonator and source/load can be intuitively neglected because its value is quite small. **Figure 16(c)** plots the simulated results derived from the equivalent circuit model, where the solid and dashed lines indicate the simulated reflection and transmission coefficients, respectively. Two transmission zeros in the notch band are created by the resonant modes of the microstrip resonator.

Next, two small patches are symmetrically added as the perturbation element to the lower angles of the triangular loop resonator. These perturbations can accomplish the further separation of the two degenerate modes, creating the dual-mode behavior of the resonator. Resonant modes of the triangular loop resonator are coupled to the slot-line, providing a bypass for the adjacent signal of its resonance, and a notch band is thus created. **Figure 17(a)** shows the transmission characteristics of the resonator versus L_5, that is, the perimeter of a triangular loop resonator. As L_5 increases from 31 to 37 mm, the central frequency of notch band falls off from 6.25 to 5.39 GHz, and its absolute bandwidth decreases from 1.49 to 1.37 GHz. Obviously, the perimeter of triangular loop resonator can directly determine the position of the notch band. **Figure 17(b)** illustrates the influence on the frequency response from varied W_5 and width of two patches. As W_5 increases from 0.2 to 1.0 mm, the notch bandwidth goes up from 1.52 to 1.79 GHz. These exhibited characteristics can be used to determine the central frequency and bandwidth of the created notch band; thus the notch band of the UWB BPF can be fully controlled.

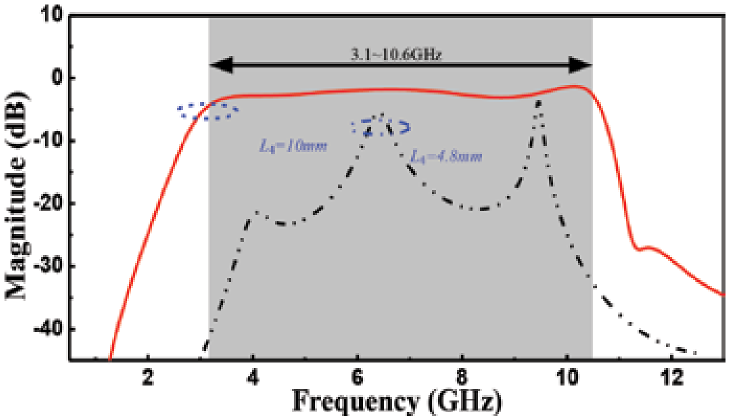

Figure 15. Frequency responses of transmission coefficient of the proposed UWB BPF with different feeding line lengths (L_4).

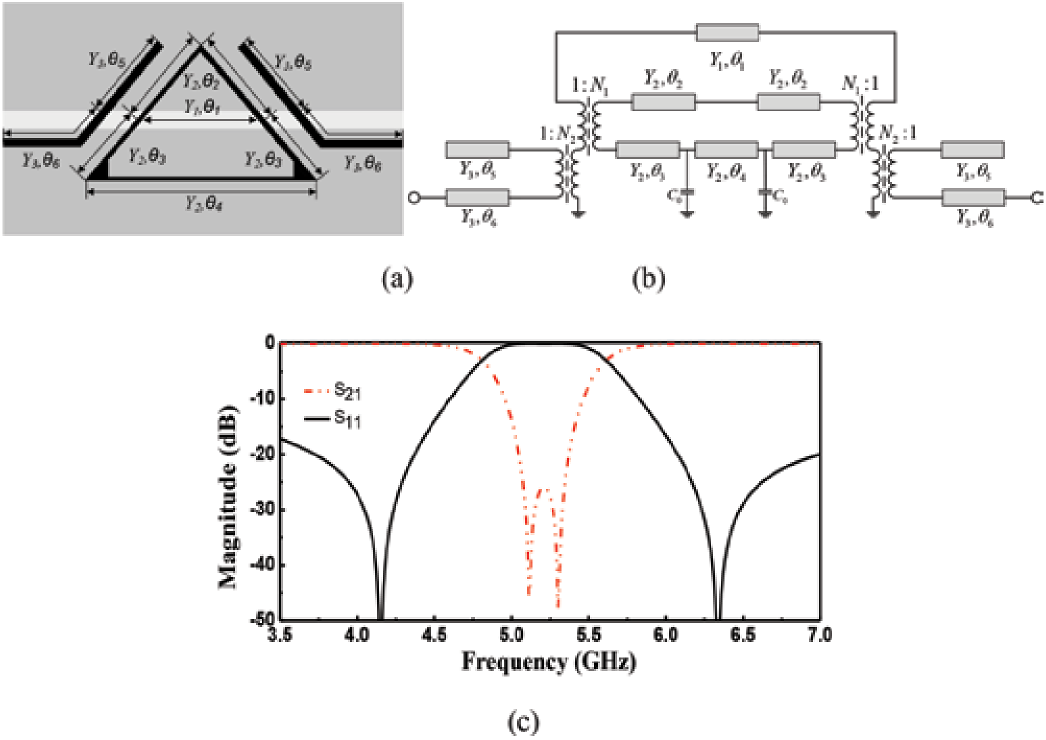

(a) (b)

(c)

Figure 16. A microstrip triangular loop resonator-loaded slot-line. (a) Diagram, (b) equivalent circuit model, and (c) simulated results.

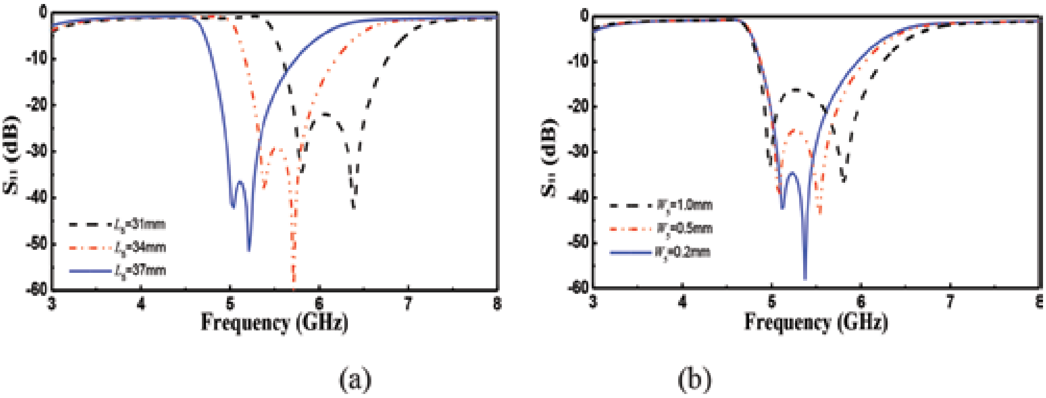

(a) (b)

Figure 17. Frequency-dependent transmission coefficient of the proposed dual-mode triangular loop resonator-loaded slot-line against (a) L_5 and (b) W_5.

4.4. Filter implementation and results

Based on the filter structure and analysis approach described above, a UWB BPF with a controllable notch band is designed and fabricated on a substrate with a dielectric constant of

$\varepsilon_r = 3.5$, loss tangent of 0.0018, and thickness of h = 0.8 mm. The layout of proposed UWB BPF with a notch band is depicted in **Figure 18**. As mentioned above, a dual-stub-loaded slot-line resonator is etched on the ground plane, and on the top layer, two folded microstrip feed lines and a microstrip triangular loop resonator are constructed. All the dimensions of the filter shown in **Figure 18** are W_0 = 1.8 mm, L_1 = 23.0 mm, W_1 = 2.0 mm, L_2 = 3.0 mm, W_2 = 0.3 mm, L_3 = 2.0 mm, W_3 = 0.8 mm, L_4 = 11.5 mm, W_4 = 0.6 mm, L_5 = 36 mm, W_5 = 0.3 mm, and S = 0.6 mm.

Simulated and measured transmission and reflection coefficients of the constructed filter are plotted in **Figure 19**. Simulated results show that the 3-dB passband of the filter covers the ranges of 2.83–4.78 GHz and 6.29–10.33 GHz, respectively, while measured ones show that the 3-dB passband covers the ranges of 2.49–4.91 and 6.29–9.2 GHz. Measured minimum insertion losses of the first and second passband are 1.1 and 1.5 dB, respectively. Measured maximum return losses in the first and second passband are 13.2 and 13.5 dB, respectively. Simulated and measured maximum insertion loss in the notch band is 25 and 35 dB,

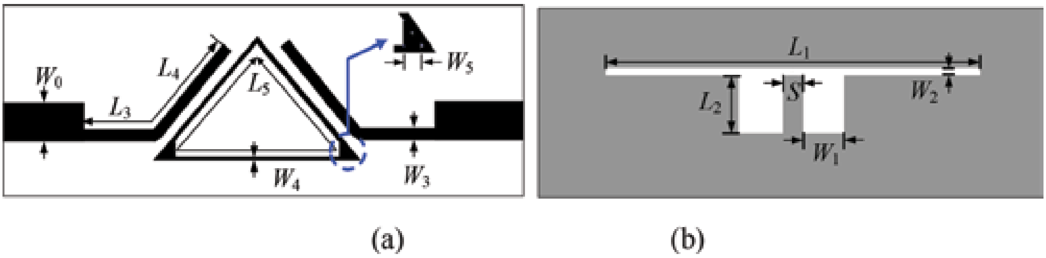

Figure 18. Schematic of the proposed band-notched UWB BPF with dual-mode triangular loop resonator-loaded dual-stub slot-line MMR. (a) Top layer and (b) bottom layer.

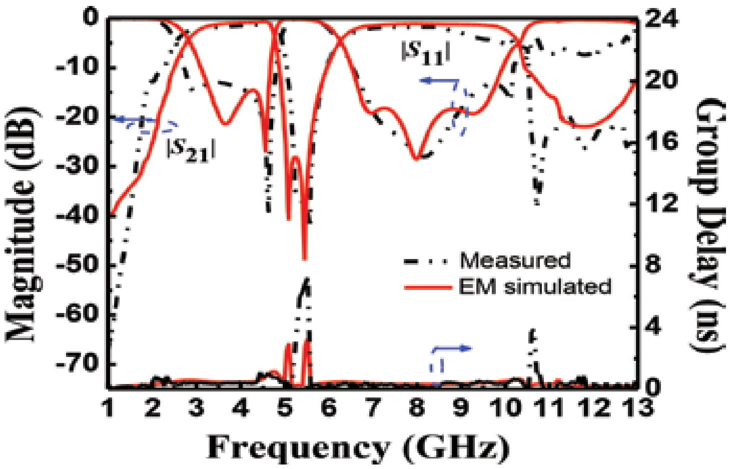

Figure 19. Simulated and measured frequency responses of the designed band-notched UWB BPF.

respectively. In general, the measured results agree well with the simulated results except the loss in the high-frequency band that may be caused by the dielectric loss and fabrication tolerance. Meanwhile, simulated and measured results indicate that the group delay within the passbands is varied between 0.3 and 0.7 ns.

5. Conclusions

Slot-line UWB BPFs and band-notched UWB filters are presented. UWB BPFs are implemented by using microstrip feed slot-line MMR. To acquire a notch band in the UWB passbands, microstrip resonators are loaded to the slot-line. Circuit model for microstrip resonator-loaded slot-line is given and analyzed. The design methodology has been finally verified by the measured results. Band-notched UBW BPFs are hot spots in a few years; there are some trends in this field, such as multiple notched band and tunable notched band.

Author details

Xuehui Guan

Address all correspondence to: xuehuiguan@gmail.com

East China Jiaotong University, Nanchang, PR China

References

[1] Federal Communications Commission. Revision of part 15 of the commission's rules regarding ultra-wideband transmission systems. Tech. Rep., ET-Docket 98-153, FCC02-48. Apr 2002

[2] Zhu L, Sun S, Menzel W. Ultra-wideband (UWB) bandpass filters using multiple-mode resonator. IEEE Microwave and Wireless Components Letters. 2005;**15**(11):796-798

[3] Gao SS, Yang XS, Wang JP, Xiao SQ, Wang BZ. Compact ultra-wideband (UWB) bandpass filter using modified stepped impedance resonator. Journal of Electromagnetic Waves & Applications. 2008;**22**(22):541-548

[4] Wu HW, Chen YW, Chen YF. New ultra-wideband (UWB) bandpass filter using triangle-ring multi-mode stub-loaded resonator. Microelectronics Journal. 2012;**43**(11):857-862

[5] Zhu L, Wang H. Ultra-wideband bandpass filter on aperture-backed microstrip line. Electronics Letters. 2005;**11**(18):1015-1016

[6] Shi X, Xi X, Liu J, Yang H. Novel ultra-wideband (UWB) bandpass filter using multiple-mode resonator. IEICE Electronics Express. 2016;**13**(11)

[7] Chen CP, Takakura Y, Nihie H, Ma Z. Design of compact notched UWB filter using coupled external stepped-impedance resonator. In: IEEE MTT-S International Microwave Conference; Boston, America. 2009. pp. 945-948

[8] Ghatak R, Sarkar P, Mishra RK, Poddar DR. A compact UWB bandpass filter with embedded SIR as band notch structure. IEEE Microwave and Wireless Components Letters. 2011;**21**(5):261-263

[9] Sun H, Feng C, Huang Y, Wen R, Li J, Chen W, Wen G. Dual-band notch filter based on twist split ring resonators. International Journal of Antennas and Propagation. 2014;**2014**. Article ID 541264

[10] Yang GM, Jin R, Vittoria C, Harris VG, Sun NX. Small ultra-wideband (UWB) bandpass filter with notched band. IEEE Microwave and Wireless Components Letters. 2008;**18**(3):176-178

[11] Uikey R, Sangam RS, Prasadu K, Kshetrimayum RS. Novel notched UWB filter using stepped impedance stub loaded microstrip resonator and spurlines. International Journal of Microwave Science and Technology. 2015;**2015**. Article ID 939521

[12] Sarkar P, Reddy BVK, Pal M, Ghatak R. UWB bandpass filter with broad notch band and ultra-wide upper stopband. In: IEEE MTT-S International Microwave and RF Conference; New Delhi, India. 2013. pp. 1-3

[13] Huang JQ, Chu QX, Liu CY. Compact UWB filter based on surface-coupled structure with dual notched bands. Progress in Electromagnetics Research. 2010;**106**(4):311-319

[14] Karthikeyan SS, Kshetrimayum RS. Notched UWB bandpass filter using complementary single split ring resonator. IEICE Electronics Express. 2010;**7**(17):1290-1295

Chapter 4

Toward Deep Learning-Based Human Target Analysis

Yuan He, Xinyu Li and Xiaojun Jing

Additional information is available at the end of the chapter

http://dx.doi.org/10.5772/intechopen.81592

Abstract

In this chapter, we describe methods toward deep learning-based human target analysis. Firstly, human target analysis in 2D and 3D domains of radar signal is introduced. Furthermore, range-Doppler surface for human target analysis using ultra-wideband radar is described. The construction of range-Doppler surface involves range-Doppler imaging, adaptive threshold detection, and isosurface extraction. In comparison with micro-Doppler profiles and high-resolution range profiles, range-Doppler surface contains range, Doppler, and time information simultaneously. An ellipsoid-based human motion model is designed for validation. Range-Doppler surfaces simulated for different human activities are demonstrated and discussed. With the rapid emergence of deep learning, the development of radar target recognition has been accelerated. We describe several deep learning algorithms for human target analysis. Finally, a few future research considerations are listed to spark inspiration.

Keywords: ultra-wideband radar, range-doppler surface, deep learning, human target analysis

1. Introduction

Human target analysis is acknowledged to be useful for a wide range of security and safety applications, such as through-wall detection and ground surveillance [1, 2]. The analysis has usually been conducted in the time-frequency (micro-Doppler) and time-range (high-range resolution profile) domains. Chen first introduced the micro-Doppler concept to the radar community in [3]. Time-frequency transforms, such as the short-time Fourier transform, are used to analyze target Doppler signatures in slow time. Since then, studies have investigated micro-Doppler-based target feature analysis [4–9]. The high-range resolution profile (HRRP) of human targets has also been studied [10]. Micro-Doppler profile and HRRP, which are both generated by micromotions, have their shortcomings: they only contain information from either the time-frequency or time-range domain. Micro-Doppler analysis neglects range information, while HRRP analysis neglects Doppler information.

Therefore, in order to analyze the target signature more comprehensively, we describe a new concept called *range-Doppler surface* (RDS). As an alternative to the micro-Doppler profile and HRRP, RDS is a radar target representation extracted from a three-dimensional data cube—the range-Doppler (RD) video sequence [11, 12]. The RDS consists of all the important information contained in both HRRP and micro-Doppler signatures. The present study analyzes the RDS using simulated and real radar data. Results suggest a new area of human target analysis and classification.

It is worth mentioning that the term "range-Doppler surface" has been presented in prior works [13–15]. It was used for a 2D range-Doppler image that is shown in a 3D perspective. In this chapter we present this term to describe the time-varying range-Doppler isosurface information. RDS is referred to 3D visualization for the first time in this study, and it is indeed a suitable, precise term to describe this concept.

Nowadays, deep learning has become a mainstream method for human activity recognition instead of conventional machine learning methods. Deep learning came into our sight and has emerged as a hot topic in the past few years. It works by learning several layers of representation for modeling the complex relationships among data. It can create high-level features from related low-level ones by means of its hierarchical architecture without artificial extraction from the raw data and specialized knowledge. In this way, it makes activity recognition system more intelligent and versatile. Therefore, deep learning is an applicable approach to identify human activities.

This chapter is organized as follows: In Section 2, human target analysis with the micro-Doppler profile, HRRP, as well as the three-dimensional RD video sequence is described. In Section 3, the range-Doppler surface is described. Then, deep learning for human activity classification is introduced briefly in Section 4. Finally, future directions are drawn in Section 5.

2. Human target analysis in 2D and 3D domains

2.1. Human target analysis with RD video sequence

The RD video sequence that consists of N time sampled 2D range-Doppler images contains both spatial and temporal characteristics: range and frequency information consists in every RD image, while time information exists among sequential frames. Compared with 1D and 2D forms of radar echoes, the joint time-/range-frequency form of echoes contains all the targets' motion information.

Among these human target analysis systems using the RD video sequence, so far, a representative example is Google Project Soli, which is the first gesture recognition system capable of recognizing a rich set of dynamic gestures based on short-range radar [27, 28]. It is based on an end-to-end trained combination of deep convolutional and recurrent neural networks, and the dataset is comprised of 3D data cubes. Combining CNN and RNN could enhance the ability to recognize different activities that vary in temporal and spatial dimensions. The system can recognize subtle gestures of 10 kinds performed by 10 people. From then on, many researches have been done using radar just like Kinect and Leap Motion in CV [21]. In addition, with the advent of this system, many novel ideas have been proposed based on it [22, 29, 30].

2.2. Human target analysis with HRRP and micro-Doppler profiles

Although containing abundant information of human activity properties, 3D form of human backscattering echoes is complicated to process. As a result, the complexity of the systems using 3D form of echoes is higher compared with those using 2D forms. 2D forms of radar echoes, which mainly refer to HRRP and micro-Doppler profiles, also carry enough human activity information and can be used for human target analysis.

It is a common way to obtain time-Doppler maps, namely, joint time-frequency transformation (JTFA) [23, 24]. Similar to the developments in other fields such as acoustics and speech processing, JTFA can provide additional insight into the analysis, interpretation, and processing of radar signals, and the performance is superior to what has been achieved in the traditional time or frequency domain alone [3].

The short-time Fourier transform (STFT) is the most commonly used time-frequency transform. STFT performs the Fourier transform on a short-time sliding window basis instead of using one long-time window to the entire signal. The square modulus of the STFT is called the spectrogram, which is a nonnegative time-frequency energy distribution without phase information [20]:

$$Spectrogram(t,f) = \left|STFT(t,f)\right|^2 \tag{1}$$

The resolution of STFT is determined by the size of window function. There is a trade-off between the time resolution and the frequency resolution [4].

By performing a STFT over time for every range bin, a series of 2D time-Doppler images along range can be acquired. Then, summing the time-Doppler "video" along range, a time-Doppler map is obtained.

Among these three 2D forms of echoes, till now, the time-Doppler maps are most commonly used to analyze human targets. The time-Doppler maps include a wealth of Doppler information changing over time. The main Doppler shift is caused by the bulk speed, while micro-Doppler is produced by rotating or vibrating parts, such as the legs, feet, and hand. By selecting and classifying the micro-Doppler features in the time-Doppler map, human activities can be recognized by various models. For example, G. Klarenbeek et al. applied a LSTM structure with the time-Doppler maps to realize the multi-target human gait classification [26].

Time-range maps contain time-varying range information between the target and the radar. When a person is moving, different components of the human body have different relative distances from the radar at time t. Therefore, various time-range maps produced by different activities can be used to recognize the corresponding activities, although they neglect the Doppler information. In [25], Yuming Shao et al. have employed the time-range maps with a deep CNN to classify human motions, and a good performance was achieved.

3. Range-Doppler surface

3.1. Range-Doppler processing

In general, separating the frequency components of different body parts is a vital step for human target analysis. However, the ability to resolve separate frequency components is limited because of the time-varying Doppler shifts in radar echoes. A general way of representing the scattered signals is range-Doppler (RD) processing. And a classical way for RD processing is to apply Fourier transform to samples from a fixed range bin over one coherent processing interval. This interval is theoretically limited by the time during which the target stays in the same range bin:

$$T_r = \frac{\delta_r}{v} \tag{2}$$

The radar transmits a coherent burst of M pulses:

$$S_{tx} = \sum_{m=0}^{M-1} p\left(t - mT_r\right) e^{j2\pi f_c t}, \tag{3}$$

where t is the fast time, $p(t)$ is the pulse complex envelope, T_r is the pulse repetition interval, and f_c is the center frequency. The echo of a moving point scatterer can be described by a delayed and attenuated version of the transmitted signal in Eq. (3):

$$S_{rx} = \alpha S_{tx}(t - \tau(t)), \tag{4}$$

where α is the complex amplitude and $\tau(t)$ is the round-trip time delay. Assuming that the radial velocity v is constant during this period, the round-trip delay can be approximated by

$$\tau(t) = \tau_0 - \frac{2v}{c} t, \tag{5}$$

where $\tau_0 = \frac{2R_0}{c}$ is the initial delay, R_0 is the initial range, and c is the speed of light. Substituting Eqs. (3) and (5) into Eq. (4) leads to

$$S_{rx}(t) = \alpha \sum_{m=0}^{M-1} p\left[\left(1 + \frac{2v}{c}\right)t - \tau_0 - mT_r\right] e^{j2\pi f_c\left(1+\frac{2v}{c}\right)t}, \tag{6}$$

where all the constant terms have been absorbed and the variable name has been kept as α. Then, for notational convenience the fast time t' was introduced: $t' = t - mT_r$. Substituting t' into Eq. (6), after demodulation the baseband signal is given as

$$S_{rx}(t', m) = \alpha p\left[\left(1 + \frac{2v}{c}\right)t' - \tau_0 + \frac{2v}{c} m\, T_r\right] e^{j2\pi f_c \frac{2v}{c}\left(t' + mT_r\right)} \tag{7}$$

In radar, we usually assume that the target remains static in one pulse duration T:

$$vT \ll \delta R \tag{8}$$

where $\delta R = \frac{c}{2B_w}$ is the range resolution of the radar and B_w is the signal bandwidth. This indicates that the Doppler effect in fast time is negligible. By simplifying, Eq. (7) can be rewritten as

$$S_{rx}(t', t_s) = \alpha p(t' - \tau_0)\, e^{j2\pi\beta f_c t_s} \tag{9}$$

FT is performed over t_s in Eq. (9) and the Doppler spectrum is given:

$$\tilde{S}_{rx}(t', f_d) = \alpha p(t' - \tau_0) sinc(f_d - \beta f_c), \tag{10}$$

where $sinc(f) = \frac{sin(\pi f)}{\pi f}$.

However, a target may traverse multiple range cells in one coherent processing interval sometimes. In this situation, applying conventional Fourier transform-based RD processing is not suitable, which will lead to a blur in frequency. To improve the Doppler resolution, a Keystone transform-based range-Doppler processing is proposed in this chapter.

By performing RD processing on the radar echoes, a sequence of RD images is obtained. The three-dimensional RD video is proposed to describe the slow-time evolution of target RD signatures.

3.2. Range-Doppler surface construction

Before constructing the RDS, it is essential to detect the target in the range-Doppler domain, since detection allows the extraction of targets and elimination of false alarms. The cell-average constant false alarm rate (CA-CFAR) procedure [16] is a classical approach of detecting a target in noise and clutter. Detection is performed employing a two-dimensional CA-CFAR procedure [17] in the range-Doppler domain. For each range-Doppler image in the range-Doppler video sequence, a sliding 2D window is applied to scan this RD image pixel by pixel. For each pixel, it is claimed as detected if its intensity exceeds an estimated threshold. In **Figure 1**, a typical 2D window is shown. The cell under test covers the target reflections. The reference cells estimate background noise for computing the detection threshold. The guard cells separate the cell under test and reference cells as a barrier. The sizes of these cells strongly affect the performance of the CA-CFAR detection and thus should be tuned carefully according to radar parameters and target characteristics (e.g., signal bandwidth, maximum unambiguous Doppler, and target velocity).

In **Figure 2a**, the detected scatterers of a simulated human target are shown in a three-dimensional (3D) volume, where the intensities of different scatterers are represented by various colors. Note that the simulated radar system uses the same parameters as used in generating **Figure 3**. Finally, the RDS (see **Figure 2b**) is constructed by creating a surface that has the same intensity value within the 3D range-Doppler-time volume (i.e., range-Doppler video sequence) in **Figure 2a**. Isosurface plots are similar to contour plots in that they both indicate where values are equal. The MATLAB® function *isosurface* is applied to extract the isosurface from the volume using a

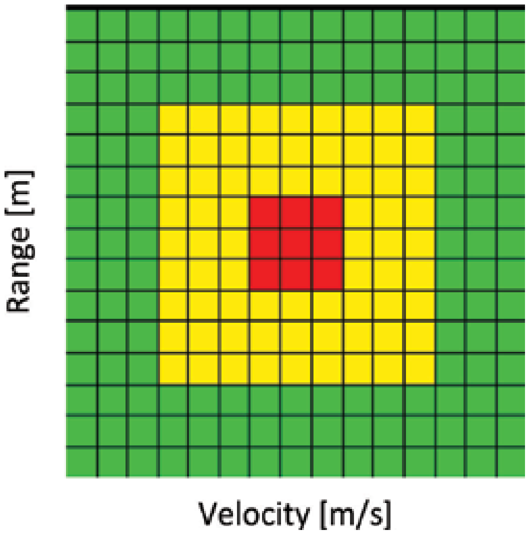

Figure 1. 2D CA-CFAR window [27] (red: cell under test; yellow: guard cells; green: reference cells).

user-defined isosurface threshold. The isosurface connects points that have the specified value much the way contour lines connect points of equal elevation. Note that the difference of the surface color in **Figure 2b** is not due to different intensities, but due to the lighting effect used to illustrate the 3D object in MATLAB®. Selecting a reasonable threshold is important in this procedure, because this affects the final output significantly. Although currently the threshold is set manually, automatic approaches to construct the volume surface are certainly interesting in future studies.

Target analysis has been commonly done in the time-range domain or time-frequency domain. As mentioned above, HRRP neglects Doppler information, while micro-Doppler neglects range information. Furthermore, micro-Doppler is difficult to be used in multi-target situations, since the Doppler spectrums of different targets may overlap. The RDS shows the target surface in the 3D range-Doppler-time space. All the important targets' information, which might be contained in HRRP and micro-Doppler, is included in RDS.

The RDS of different body segments is presented in **Figure 4**. The responses of the feet are well separated in either range or Doppler, and the responses of the thorax and hands overlap with each other. The feet have a larger Doppler offset than the thorax and hands.

3.3. RDS of measured human activities

PulsOn 400 radar system, manufactured by Time Domain Corporation [18], was used to acquire measurement data (experimental setup; see **Figure 5**). Its operational frequency band is 3.1–5.3 GHz, and the signal is modulated by an m-sequence. The transmitted power is −14.5 dBm. The pulse repetition frequency is 200 Hz, and the sampling frequency is 16.39 GHz. More details about this radar are given in the literature [19].

In the measurement, two scenarios were considered: single-person walking and two-people walking. The RDSs generated for these two scenarios are presented in **Figures 6** and **7**, respectively. The RDS for the single-person scenario is similar to the simulated RDS shown

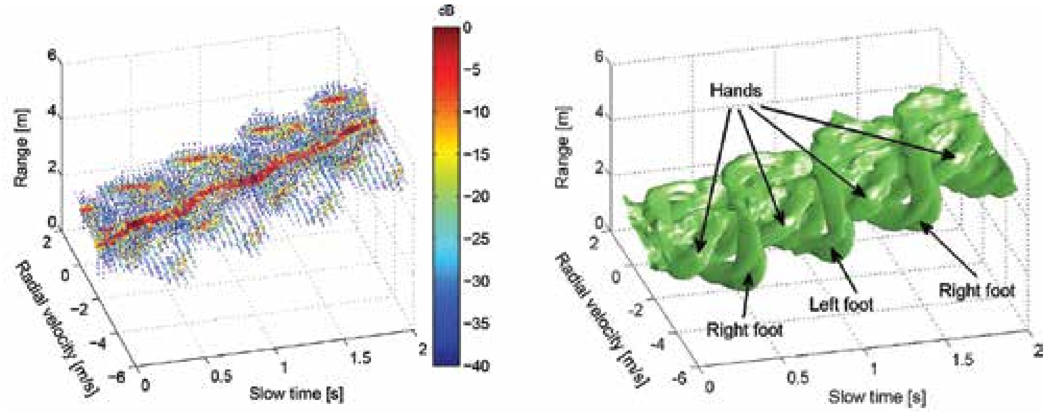

(a) Detected CFAR plots in range-Doppler-time space (b) Range-Doppler surface

Figure 2. Range-Doppler surface of a simulated walking human target.

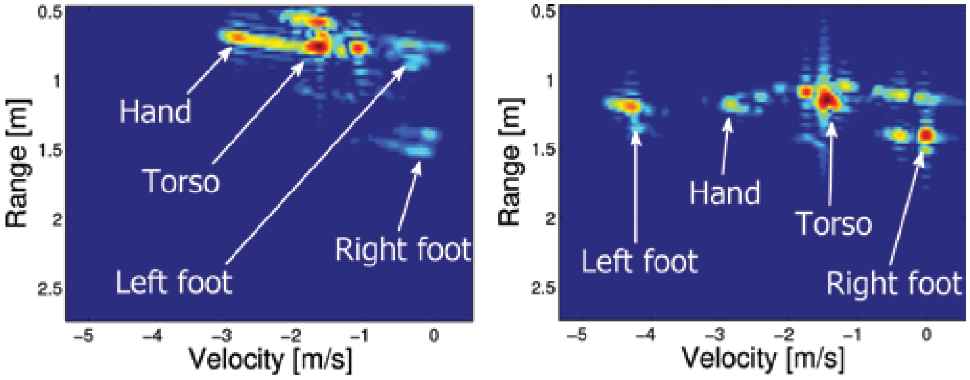

(a) Double support (b) Right stance

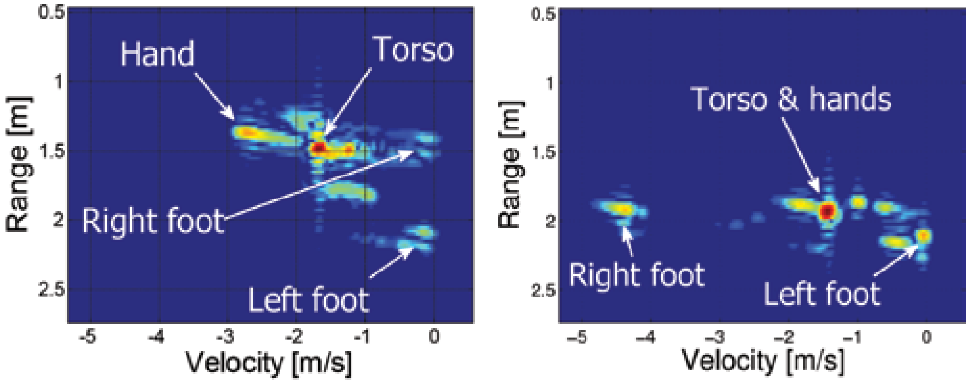

(c) Double support (d) Left stance

Figure 3. Range-velocity images of one simulated human gait.

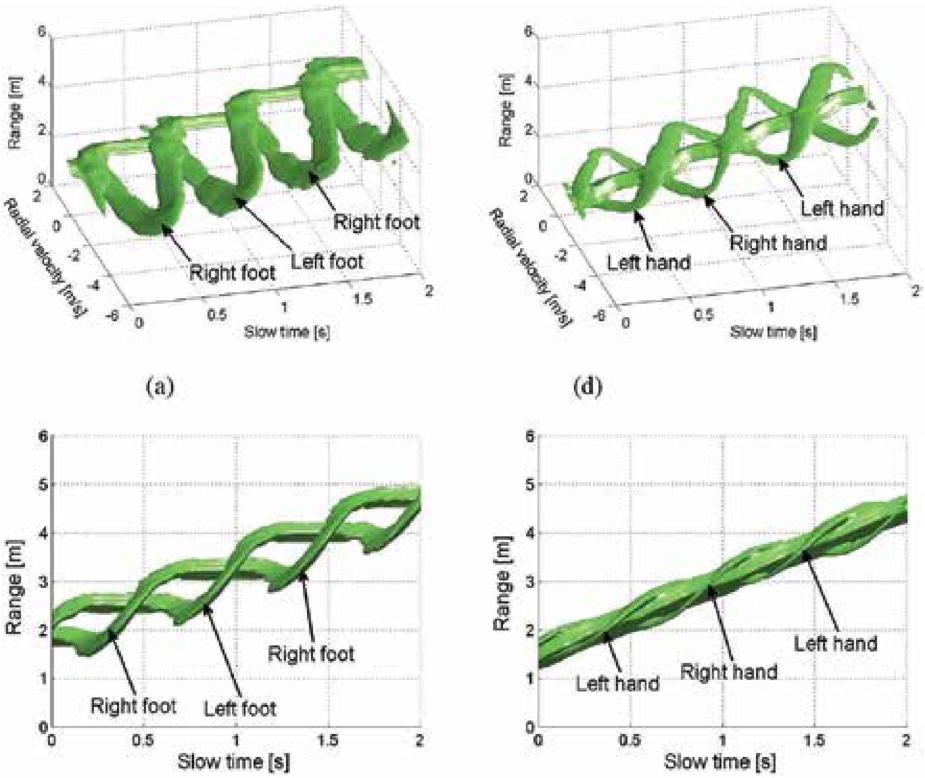

(b) (a) (e) Time-range projection of RDS in (d]

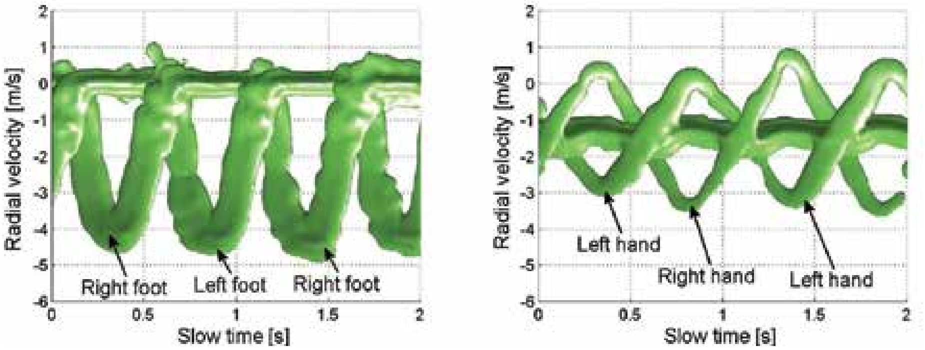

Figure 4. Range-Doppler surface of different body segments (a) RDS of feet, (b) Time-range projection of RDS in (a), (c) Time-velocity projection of RDS in (a), (d) RDS of thorax + hands, (e) Time-range projection of RDS in (d), (f) Time-velocity projection of RDS in (d).

in **Figure 2b**, and the capability of RDS to separate body segments is demonstrated again in **Figure 6d** and **e**. It should be noted that in the processing for real data, static clutter is removed via moving target indication before constructing RDS, which cancels the clutter and also the stationary parts of the human body. More precisely, in each walking step, the reflection from the stationary leg/foot is rejected, while the reflection of the moving leg/foot is retained.

Figure 5. Radar system and experimental setup.

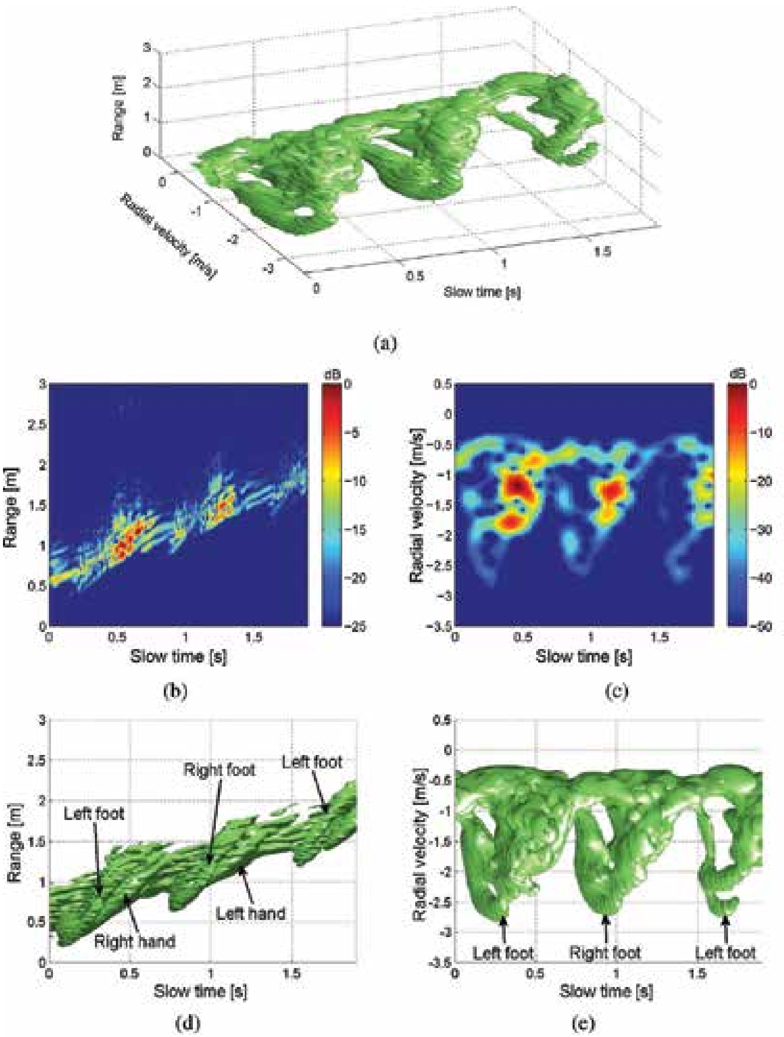

Figure 6. Range-Doppler surface of two human targets (threshold = −20 dB).

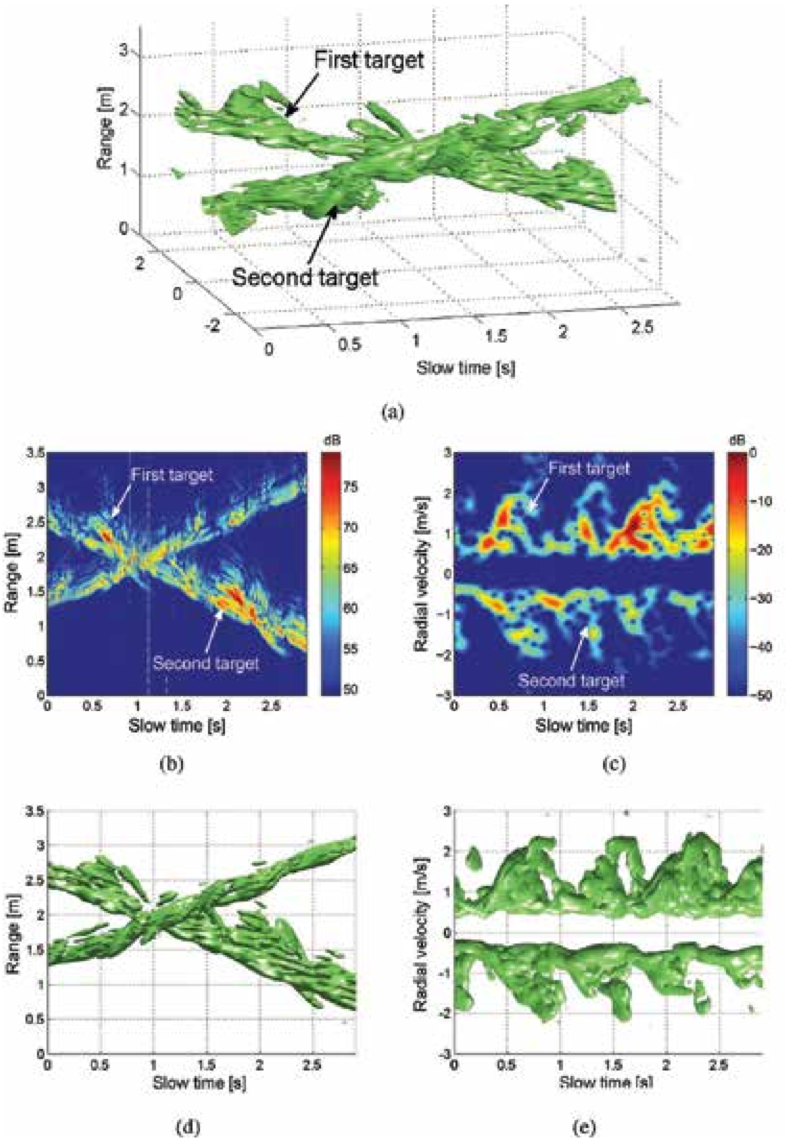

Figure 7. Range-Doppler surface of two human targets (threshold = −23 dB).

In **Figure 7**, the RDS of the two-people scenario shows that the backscattering of the human targets is automatically separated in the 3D range-Doppler-time space. This indicates that RDS is not only able to show the range-Doppler signatures of a single extended target but also able to separate (or even track) multiple targets in the range-Doppler video sequence. Additional processing to separate multi-target reflection (e.g., the separating method proposed in [19]) is not required anymore.

As an example, the RDS has been demonstrated for human target analysis using an S-/C-band UWB radar, but RDS itself is in fact a generic tool. It can be used in various applications, such as feature extraction, tracking, or classification. Similar to micro-Doppler or high-resolution range profiles, the RDS has the potential of being used to analyze different types of targets (e.g., people or animals) and also used in different types of radars (e.g., S-band, C-band, or X-band radar).

4. Deep learning for human target analysis

With the rapid emergence of new deep learning algorithms and architectures, the development of many domains such as speech recognition, visual object recognition, object detection, and even drug discovery and genomics has been accelerated. Deep learning is composed of multiple processing layers to learn high-level representations with multiple levels of abstraction, thus automating the process of feature extraction. Hence, deep models do not need heavy feature engineering and domain knowledge compared with traditional machine learning techniques. What is more, with so many complicated deep-level transformations, very complex functions can be learned, and more classification and recognition problems can be solved. As a result, deep learning has made great contributions in overcoming difficulties in artificial intelligence and advancing the development of artificial intelligence.

Next, we will mainly describe several deep learning models, which are used mostly in human target analysis field.

4.1. Convolutional neural network

Convolutional neural network (CNN) is inspired by the visual cortex structure which is composed of simple cells and complex cells. It adopts four key ideas: local connections, parameter sharing, pooling, and multilayers. In this way, CNN is able to fully explore the property of raw signals that there are compositional hierarchies, namely, extracting higher-level features from the lower-level ones. As a result, convolutional neural networks, as one of the representative algorithms of deep learning, have made a remarkable progress in object detection and recognition, natural language processing (NLP), speech recognition, and medical image analysis in the past few years. In human activity recognition field, CNN is one of the most used deep learning models. For instance, Zhenyuan Zhang et al. have adopted this network to realize continuous dynamic gesture recognition using a radar sensor [30], while Youngwook Kim et al. detected and classified human activities using deep convolutional neural networks [32].

4.2. Recurrent neural network

With the successful application in NLP, recurrent neural network (RNN) has caught researchers' attention. RNNs have shone light on modeling temporal sequences such as texts and speeches because they can mine timing and semantic information in them. From the perspective of network structure, RNN can remember the previous information and use it to influence the output of the following nodes. However, conventional RNN has its own limit: long-term dependencies. To overcome this problem, long short-term memory (LSTM) came into being and performed better in many tasks. LSTM owns three special gates: input gate, output gate, and forget gate. By using these memory units especially the forget gate, LSTM can access a long-range context of the sequential data. Due to these advantages above, many human activity recognition systems adopted RNN and its variants. Zhi Zhou et al. adopted multimodal signals, including HRRPs and Doppler profiles, which are acquired by the terahertz radar system to recognize dynamic gestures, and the recognition rate reaches more than 91% [22].

4.3. Auto-encoder

Auto-encoder is a high-performance deep learning network suitable for dealing with one-dimensional data by extracting optimized deep features. It learns a deep feature representation of raw input via several rounds of encoding-decoding procedures. Auto-encoder applies the layer-wise greedy unsupervised pre-training principle so as to quickly obtain an efficient deep network.

The commonly used variants of auto-encoder are mainly the following kinds: (1) sparse auto-encoder, which is able to rebuild the input data well, and (2) de-noising auto-encoder and contractive auto-encoder which can make the models more generic by adding noise or a well-chosen penalty term.

Auto-encoder is able to provide a powerful feature extraction approach for many tasks, which saves a lot of labor. In this way, auto-encoder can combine with whether conventional machine learning algorithm or other deep learning models and becomes a more robust one. Mehmet Saygin Seyfiolu et al. [33] used a convolutional auto-encoder architecture to discriminate 12 indoor activity classes involving aided and unaided human motions by recognizing different 2D Doppler maps, and Branka Jokanovic et al. [34] applied three stacked auto-encoders to extract deep features, respectively, and fuse the result together with a voting principle to classify activities.

5. Future directions

Despite plentiful human target analysis researches have been done with all kinds of deep learning methods and the effect is considerable, there are still many challenges and opportunities. Next, a few future research considerations will be listed below.

5.1. Distinguish radar images from natural images

Among three forms of backscattered radar signals mentioned above, 2D domain radar signals such as time-Doppler maps and time-range maps are mostly used for recognition because they are represented in two dimensions and look more intuitive. Furthermore, these deep learning models are usually introduced from the field of computer vision. In CV area, the images are natural images but the radar images are not. This will lead a doubt that it is proper or not to treat radar 2D images as natural images completely. As a result, it is very urgent to create some techniques to distinguish more radar images with natural images.

5.2. Notice phase information

Common energy-based power spectrograms after FT or STFT always abandon the phase information in backscatter echoes. But phase is an important attribute of any signal and contains a wealth of information such as transmission duration and distance. Pavlo Molchanov et al. investigated frequency and phase coupling phenomena for radar backscattered signals and proposed novel bicoherence-based information features [31]. We think phrase information in radar backscattering signals should be considered more in future studies.

5.3. Take orientation sensitivity into consideration

Doppler shift is caused by the radial velocity of the moving target. The radial velocity changes with the position of the target and the radar because it is the component of the object's velocity. In other words, when the radar is above the pedestrian, the Doppler is partly induced by the motion vertical component such as arm and leg vertical motions. In this case, negative Doppler will appear. As a result, if the relative position is different, radar backscattered signals produced by one subject performing a specified activity will differ a lot. How to overcome the orientation sensitivity of radar-based HAR is one of the future research topics.

5.4. Focus more on 1D and 3D domain radar echoes

Through the investigation of the current research status, compared with the researches in 2D domain, there are few research results on 1D and 3D domains of human echo signals, but through the discussion in previous chapters, we have reason to believe that the two forms of echoes have enough development potential and explore space. Thus, more attention should be paid to this part of human target analysis field.

Acknowledgements

I would like to express my gratitude to Pavlo Molchanov, Takuya Sakamoto, Pascal Aubry, Francois Le Chevalier, and Alexander Yarovoy for their contribution. I thank them for assisting and supporting and for their advisable opinions.

Author details

Yuan He*, Xinyu Li and Xiaojun Jing

*Address all correspondence to: eric.yuanhe@gmail.com

Beijing University of Posts and Telecommunications, Beijing, China

References

[1] Lai CP, Narayanan RM, Ruan Q, et al. Hilbert-Huang transform analysis of human activities using through-wall noise and noise-like radar. IET Radar, Sonar and Navigation. 2008;**2**(4):244-255

[2] He Y. Human target tracking in multistatic ultra-wideband radar [PhD thesis]. Delft University of Technology; 2014

[3] Chen VC. Analysis of radar micro-Doppler with time-frequency transform. In: Proceedings of Tenth IEEE Workshop on Statistical Signal and Array Processing, USA. 2000. pp. 463-466

[4] Chen VC. The Micro-Doppler Effect in Radar. Norwood, MA, USA: Artech House; 2011

[5] Tahmoush D, Silvious J. Recognizing and Tracking Humans and Vehicles Using Radar. In: Proceedings of SPIE 7539, Intelligent Robots and Computer Vision XXVII: Algorithms and Techniques. 2010. p. 753907

[6] Zabalza J, Clemente C, Di Caterina G, et al. Robust PCA for micro-Doppler classification using SVM on embedded systems. IEEE Transactions on Aerospace and Electronic Systems. 2014;**50**(3):2304-2310

[7] Smith GE, Woodbridge K, Baker CJ, et al. Multistatic micro-Doppler radar signatures of personnel targets. IET Signal Processing. 2010;**4**(3):224-233

[8] Andrić M, Bujaković D, Bondžulić B, et al. Analysis of radar Doppler signature from human data. Radioengineering. 2014;**23**(1):11-19

[9] Thayaparan T, Abrol S, Riseborough E, Stanković L, Lamothe D, Duff G. Analysis of radar micro-Doppler signatures from experimental helicopter and human data. IET Radar, Sonar and Navigation. 2007;**1**(4):289-299

[10] Fogle OR. Human micro-range/micro-Doppler signature extraction, association, and statistical characterization for high-resolution radar [PhD thesis]. Wright State University; 2011

[11] He Y, Aubry P, Le Chevalier F, Yarovoy AG. Decentralised tracking for human target in multistatic ultra-wideband radar. IET Radar, Sonar and Navigation. 2014;**8**(9):1215-1223

[12] He Y, Aubry P, Le Chevalier F, Yarovoy AG. Self-similarity matrix based slow-time feature extraction for human target in high-resolution radar. International Journal of Microwave and Wireless Technologies. 2014;**6**(Special Issue 3-4):423-434

[13] Howland PE, Maksimiuk D, Reitsma G. FM radio based bistatic radar. IEE Proceedings Radar, Sonar and Navigation. 2005;**152**(3):107-115

[14] Chetty K, Smith G, Woodbridge K. Through-the-wall sensing of personnel using passive bistatic wifi radar at standoff distances. IEEE Transactions on Geoscience and Remote Sensing. 2012;**50**(4):1218-1226

[15] Wang G, Xia X, Root BT, Chen V, Zhang Y, Amin M. Manoeuvring target detection in over-the-horizon radar using adaptive clutter rejection and adaptive chirplet transform. IEE Proceedings Radar, Sonar and Navigation. 2003;**150**(4):292-298

[16] Richards MA, Scheer JA, Holm WA. Principles of Modern Radar: Basic Priciples. Inc., Raleigh, NC: SciTech Publishing. 2010

[17] Daho OB, Khamlichi J, Chappe O, et al. Using CFAR algorithm to further improve a combined through-wall imaging method. In: Proceedings of 20th European Signal Processing Conference (EUSIPCO), Romania; 2012. pp. 2521-2525

[18] Time Domain Corporation. http://www.timedomain.com/ [Accessed: Dec, 2014]

[19] Sakamoto T, Sato T, He Y, Aubry PJ, Yarovoy AG. Texture-based technique for separating echoes from people walking in UWB radar signals. In: Proceedings of URSI International Symposium on Electromagnetic Theory, Japan. 2013. pp. 119-122

[20] Chen VC, Qian S. Joint time-frequency transform for radar range-Doppler imaging. IEEE Transactions on Aerospace and Electronic Systems. 1998;**34**(2):486-499

[21] Smith KA, Csech C, Murdoch D, et al. gesture recognition using mm-wave sensor for human-car interface[J]. IEEE Sensors Letters. 2018;**2**(2):1-4

[22] Zhou Z, Cao Z, Pi Y. Dynamic gesture recognition with a terahertz radar based on range profile sequences and doppler signatures[J]. Sensors. 2017;**18**(1):10

[23] Chen VC. Joint time-frequency analysis for radar signal and imaging. In: Geoscience and Remote Sensing Symposium, 2007. IGARSS 2007. IEEE International. IEEE; 2008. pp. 5166-5169

[24] Fathy AE. UWB micro-doppler radar for human gait analysis using joint range-time-frequency representation. In: Active and Passive Signatures IV; 2013. p. 873404

[25] Shao Y, Guo S, Sun L, et al. Human motion classification based on range information with deep convolutional neural network. In: International Conference on Information Science and Control Engineering. IEEE Computer Society; 2017. pp. 1519-1523

[26] Klarenbeek G, Harmanny RIA, Cifola L. Multi-target human gait classification using LSTM recurrent neural networks applied to micro-Doppler. In: European Radar Conference. 2017; pp. 167-170

[27] Poupyrev I, Poupyrev I, Poupyrev I, et al. Soli: Ubiquitous gesture sensing with millimeter wave radar. ACM Transactions on Graphics. 2016;**35**(4):142

[28] Wang S, Song J, Lien J, et al. Interacting with soli: Exploring fine-grained dynamic gesture recognition in the radio-frequency spectrum. In: Symposium on User Interface Software and Technology. ACM; 2016. pp. 851-860

[29] Sang Y, Shi L, Liu Y. Micro hand gesture recognition system using ultrasonic active sensing[J]. IEEE Access; 2018

[30] Zhang Z, Tian Z, Zhou M. Latern: Dynamic continuous hand gesture recognition using fmcw radar sensor[J]. IEEE Sensors Journal. 2018;**18**(8):3278-3289

[31] Molchanov P, Astola J, Egiazarian K, et al. Frequency and phase coupling phenomenon in micro-Doppler radar signature of walking human[C]//2012 13th International Radar Symposium. IEEE. 2012:49-53

[32] Kim Y, Moon T. Human detection and activity classification based on micro-doppler signatures using deep convolutional neural networks. IEEE Geoscience and Remote Sensing Letters. 2016;**13**(1):812

[33] Seyfioğlu MS, Özbayğglu AM, Gurbuz SZ. Deep convolutional autoencoder for radar-based classification of similar aided and unaided human activities[J]. IEEE Transactions on Aerospace and Electronic Systems; 2018

[34] Jokanovic B, Amin M, Erol B. Multiple jointvariable domains recognition of human motion. In: Radar Conference; 2017. p. 09480952

UWB Signal Generation and Modulation Based on Photonic Approaches

Ke Xu

Additional information is available at the end of the chapter

http://dx.doi.org/10.5772/intechopen.81311

Abstract

Demands for efficient and reliable wireless communications between computers, mobile phones, and other portable electronic devices in short distances are increasing very fast. Ultra-wideband impulse radio is one of the promising techniques, which has gained much research interests in recent years. It covers a wide scope of applications in short-reach wireless communications. Conventionally, the low-bandwidth electronics can process the UWB signals very well. More recently, microwave photonics has enabled a new paradigm for developing UWB techniques in photonic domain. The photonic approaches offer much higher bandwidth and seamless compatibility with optical fiber networks, which allow for scaling the UWB technology to more advanced application scenarios. This chapter is included because photonic approaches have become a unique and effective technique in microwave signal processing. We do not attempt to offer a comprehensive review of UWB photonics, but rather to introduce the typical photonic solutions for UWB signal generation, modulation, transmission, down conversion, and so on.

Keywords: UWB generation, UWB modulation, UWB-over-fiber, microwave photonics

1. Introduction

Ultra-wideband impulse radio (UWB-IR) shows great promise in short-range high-throughput wireless communications and sensor networks owing to its intrinsic properties, such as immunity to multipath fading, extremely short time duration, being carrier free, and having low duty cycle, wide bandwidth, and low power spectral density [1–8]. While mature microelectronics can generate the impulse signals with perfect quality [9–11], the increasing demands for wireless bandwidth have driven the UWB-IR moving to higher frequency like W band (100 GHz). Besides, UWB is limited to coverage of its immediate surrounding area (up to 10 m) because of its low radiation power. Due to its light weight, low power consumption, low latency, and large bandwidth, optical fiber is considered to be an optimal solution to distribute the wireless signal over several tens of meters or kilometers. As such, it is no longer an economical way to process the UWB signals in electrical domain since an additional electrical-to-optical conversion (EOC) is needed, which increases the cost and power budget of the whole system. Alternatively, an all-optical UWB transmitter that includes impulse generation and data encoding will be highly desirable as no EOC is required. The signal generated in optical domain can be directly fed into the local optical fiber network for distribution. Such UWB-over-fiber solution can be fully compatible with the infrastructure of the current passive optical network (PON). It means that the wireless signal and the wired signal can share the same optical fibers, which further reduce the costs.

Due to the advantages of optics, such optical approaches have been widely studied for microwave applications, and it has become a promising research area—microwave photonics (MWP). Over the past two decades, the wireless communication community holds the continuous demands for low power consumption, larger transmission capacity, flexibility in signal distribution, and so forth. Particularly, the optical communications have advanced significantly, and it gives rise to a plethora of mature device and system technologies, which can handle many problems with frequencies from microwave to millimeter wave and THz range. MWP has been reported to offer a wide range of promising solutions to arbitrary microwave signal generation, modulation, multicasting, beam forming, filtering, phase shift, interference cancelation, frequency conversion, and so on. Compared with components working at radio frequencies, optical and electrooptic devices in MPW have nearly no bandwidth limitation, which allow for very high-speed microwave signal processing. The MWP device platform mainly includes fiber optics, integrated materials like silicon or III–V semiconductors, electro-optic crystals, and other material systems. The principal idea for MWP is to manipulate the optical wave using optical techniques, which includes optical nonlinear effects, electrooptic effects, optical filtering, optical spectrum shaping, and so on. After proper optical processing, the optical signal can be downconverted to microwave domain by photodetection.

MWP has a wide scope of topics like signal generation, modulation, distribution, photonic analog-to-digital conversion, and many other signal processing applications. It should be noted that signals with frequencies located in a wide spectral band spanned from several GHz to one millimeter can be handled by MWP. Among such a broad area, UWB signal processing in optical domain is one of the most interesting research topics within the MWP community due to its intrinsic advantages of low power density and high data rate. To make it work, a handful of approaches have been proposed, and some of the excellent results have been demonstrated so far. In this chapter, we will provide some technology introduction, literature review, and insight of application prospect that are related to UWB photonics.

2. UWB signal generation

UWB-IR is regulated by the Federal Communications Commission (FCC) for indoor wireless access operating in the frequency range from 3.1 to 10.6 GHz [1]. Based on the FCC definition, a UWB signal should have a spectral bandwidth that is greater than 500 MHz or a fractional bandwidth that is greater than 20% [1]. The UWB-IR can be generally classified into two categories: (1) the direct sequence UWB-IR [7] and (2) the multiband UWB-IR [8]. Direct sequence impulse radio is a simple and widely accepted form for UWB communications since it is carrier free. Thus, there is no need for complicated frequency mixers and local oscillators to up- or downconvert the carrier frequency. The generation of UWB pulses is one of the most important considerations within a UWB transmitter because the impulse quality will affect the system performance significantly [12].

Gaussian pulses are the most widely used waveforms in UWB-IR communications as they offer the advantages like simplicity and achievability. In principle, different orders of UWB-IR waveforms can be generated by using different orders of frequency differentiator filter with a Gaussian pulse input [2]. The optical band-pass filter is normally able to act as a first- or second-order frequency discriminating filter. However, it has been demonstrated that the frequency spectra of both UWB monocycle and doublet pulses have significant components in the low frequency range (<2 GHz) and thus violate the dip in the FCC spectral mask [13, 14]. Higher-order derivative of Gaussian pulses like triplet, quadruplet pulse, and some other waveforms that are more power efficient are highly desirable but rather difficult and expensive to achieve [15–17]. Here, we introduce the typical UWB signal generation techniques that relied on electrooptic components. These approaches include [2]: (1) phase modulation to intensity modulation (PM-IM) conversion, (2) optical nonlinear effects, (3) optical spectral shaping and frequency-to-time mapping, (4) microwave delay-line filter, and (5) injection locking.

2.1. PM-IM conversion

PM-IM conversion is one of the earliest methods that developed for UWB-IR generation, which was realized by changing the phase relationships among all the frequency components of the optical phase-modulated signal. A frequency discriminating filter is normally needed to convert the phase to intensity, and thus, it can also be considered as optical filtering technique. A single-stage filter can generate the monocycle pulses when the optical carrier is biased at the linear slope of the filter. Higher-order Gaussian derivative pulses can be generated by using multiple filter and superimposing their outputs. **Figure 1** illustrates how a single filter produces the monocycle pulses. An electrical Gaussian pulse should be first converted to the optical domain using a phase modulator. The phase-modulated signal is then applied to a frequency discriminating filter. The laser wavelength can be adjusted to either side of the linear region of the filter spectrum slope. The operation of phase modulation and frequency discrimination is equivalent to a first-order differentiation of the input Gaussian pulses encoded on the optical phase. The phase-modulated signal with a constant intensity will be converted to an intensity monocycle waveform through the PM-IM process as shown in **Figure 1**. The converted signal is then detected at a PD, which serves as an envelope detector.

The normalized optical field being phase-modulated by the Gaussian pulse train can be expressed in the form of

$$E_{PM}(t) = \exp\left[j\,\omega_c\,t + \beta_{PM}\cdot s(t)\right] \tag{1}$$

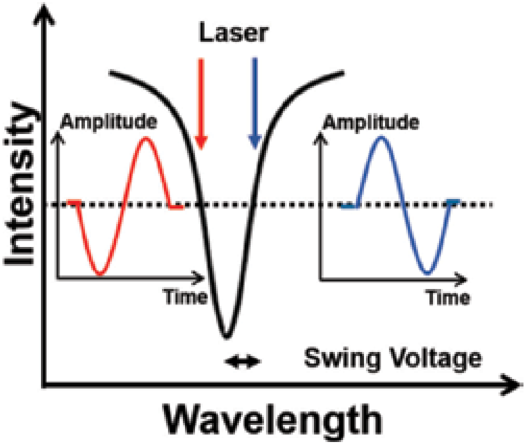

Figure 1. The schematic diagram of the monocycle pulse generation based on PM-IM conversion.

where ω_c is the angular frequency of the optical carrier, β_{PM} is the phase modulation index, and s(t) is the pulse train represented by

$$s(t) = \sum_{n=-\infty}^{+\infty} \Omega(t - nT_\Gamma) \tag{2}$$

Based on the configuration shown in **Figure 1**, when the phase-modulated light is located at the linear region of the filter spectral slopes, as shown in **Figure 1** at A, the ac part of the recovered signal at the output of the PD can be written as [7].

$$\tau(t) \sim RP\beta_{PM}K \cdot s'(t) \tag{3}$$

where R is the responsivity of the PD, P is the optical power after the filter, K is the slope steepness factor of the filter transmission spectrum, and s′(t) is the first-order derivative of the modulating signal s(t). Then, the UWB monocycle pulses are obtained.

Monocycle UWB-IR is the simplest waveform that can be directly generated from a single optical filter, but the power spectrum of the monocycle is not efficient. Here, we introduce a more advanced PM-IM conversion scheme with multiple filters, which allows for more power-efficient UWB-IR generation. The principle is described in **Figure 2(a** and **b)** where the laser wavelength can be biased at different nonlinear slope of the filter spectrum. Different types of asymmetric monocycle pulses can then be generated with different polarities due to the intensity peaking effect. Based on such asymmetric monocycle waveforms, we can superimpose them into higher-order Gaussian derivative pulses using the configuration shown in **Figure 2(c)**. The generation of a doublet or triplet pulse can be implemented via two identical optical filters in parallel with each producing an asymmetric monocycle first. By introducing an appropriate group delay to one of the pulses, a simple combination of the two pulses can generate the target doublet pulse or triplet pulse. As indicated in **Figure 2(c)**, quadruplet pulses can also be generated using such delay and superimpose method if three identical filters and two optical delay lines are used.

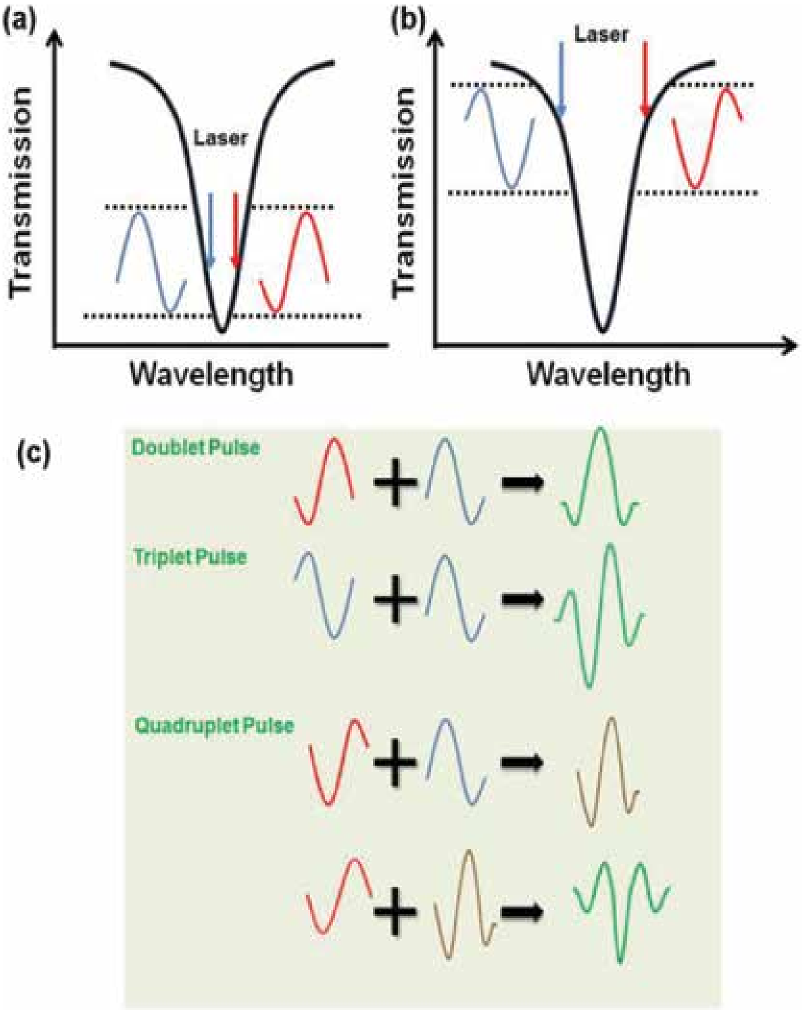

Figure 2. The schematic diagram of the (a and b) generation of asymmetric monocycle pulses; (c) generation of higher-order Gaussian pulses using combination of different asymmetric monocycle pulses.

The selection of an optical frequency-discriminating filter is important in the PM-IM conversion process. In optics, the fiber Bragg grating (FBG), thin-film band-pass filter, arrayed waveguide grating (AWG), Sagnac filter can be the excellent candidate. For example, FBG, a type of distributed Bragg reflector constructed in a short segment of optical fiber that reflects particular wavelengths of light and transmits all others, can be flexibly designed and a frequency discriminator with the desired optical spectrum that is suitable for PM-IM conversion. A typical setup for FBG-based UWB-IR generation is shown in **Figure 3**. Light from a laser diode is fiber coupled to an electrooptic PM, which is driven by a sequence of Gaussian pulses.

The phase-modulated optical signal is then applied to an FBG via an optical circulator. The PM-IM conversion is achieved by using the FBG serving as a frequency discriminator. The converted UWB signal is then detected at a PD, which serves as an envelope detector.

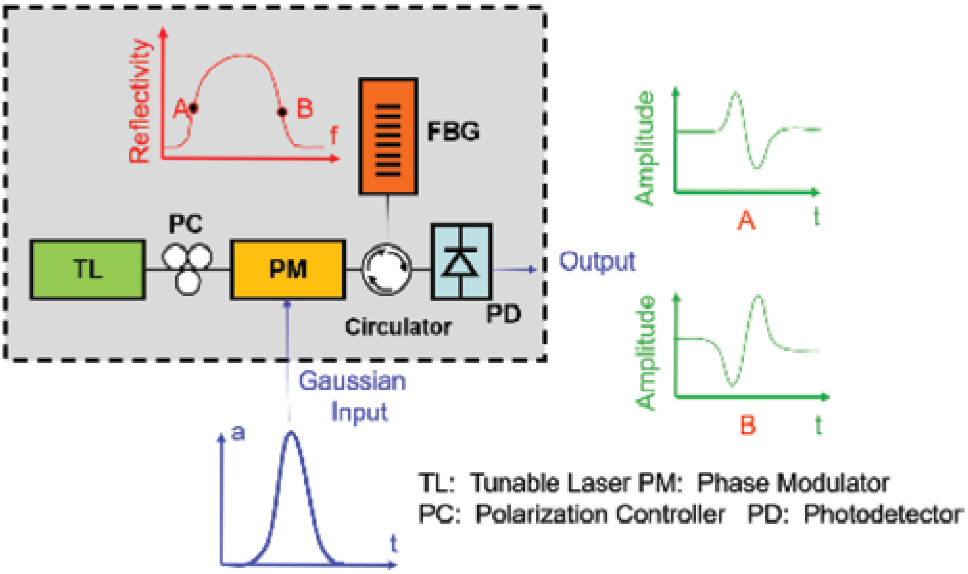

Figure 3. The schematic setup of a typical FBG-based monocycle pulse generation system.

2.2. Optical nonlinear effects

Optical nonlinear effects in optical waveguides like optical fiber, periodically poled lithium niobite, integrated nanowire waveguide are ultrafast processes that can be highly functional in many areas. Here, we introduce several nonlinear processes that can be applied to UWB-IR generation [18, 19]. It is important to point out that most of such techniques are associated with the PM-IM conversion. We still consider them as a new class of technique due to their unique mechanisms compared with the typical PM-IM approaches.

Typically, by sending a phase-modulated Gaussian pulse to a frequency-discriminating filter, a Gaussian monocycle pulse can be generated via frequency discrimination. Higher-order Gaussian pulses can be obtained by combining time-delayed UWB monocycles at different wavelengths with inverted polarities [20, 21]. Alternatively, for example, triplet pulses can be generated through four-wave mixing effect combined with an optical band-pass filter. In this scheme, the high-order Gaussian triplet pulse is directly generated by performing the first-order derivative of a phase-modulated Gaussian doublet pulse without complicated superposition of different pulses.

A general schematic block diagram of such four-wave mixing (FWM)-based UWB generation is depicted in **Figure 4**. The two paths of input optical continuous waves (CWs) are phase modulated. The phase modulators are driven by two sets of electrical Gaussian pulses that can be divided from a single-pulse pattern generator. For the upper electrical path, the Gaussian pulse is processed by an electrical Mach-Zehnder interferometer (MZI) before driving to the phase modulator. An optical delay is between the two light waves. The two light waves are then combined together and fed into the nonlinear medium such as highly nonlinear fiber, silicon waveguide, or chalcogenide waveguide to perform FWM. The output signal is converted

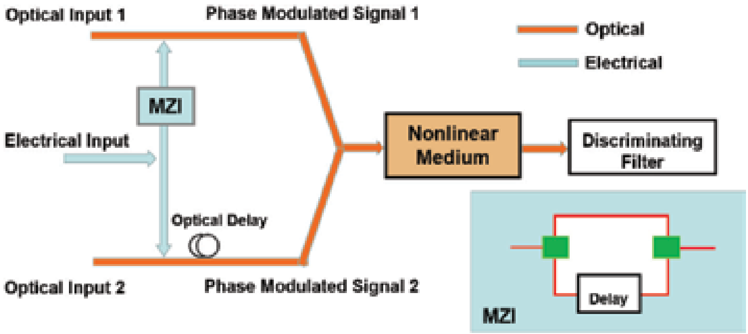

Figure 4. The schematic block diagram of the four-wave mixing (FWM)-based triplet pulse generation.

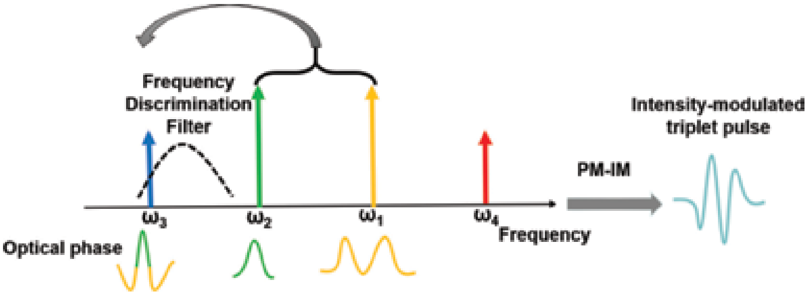

Figure 5. The schematic illustration of the working principle for triplet pulse generation using FWM.

to the triplet pulses by a discriminating filter via PM-IM conversion. An UWB triplet can be generated by converting the signal into the electrical domain using a photodetector.

The working principle of this method is shown in **Figure 5** where the electrical MZI modulated the light wave (ω_1) with a modified Gaussian pulse and the other carrier (ω_2) with a normal Gaussian pulse. An FWM process will function as a phase conjugation that modulates the idler phase with a triplet Gaussian pulse as shown in the inset of **Figure 5**. Then, an optical band-pass filter will translate this phase response into intensity triplet pulses. Compared with the monocycle pulse, triplet pulse has a suppression in the low frequency range that makes the spectrum fit the FCC mask better.

Two-photon absorption (TPA) is another optical nonlinear effect that can be used for UWB signal generation. The schematic block diagram of the all-optical UWB monocycle pulse generation using non-degenerated TPA in a nonlinear WG is shown in **Figure 6**. A CW probe and a pulse pump are aligned to the Si waveguide's TE-like mode and coupled together. After propagation through the long waveguide, the CW probe is inversely modulated by the pulse pump during the non-degenerated TPA process in the nonlinear WG. By properly controlling the delay and power relation between the attenuated pump and inversely modulated probe, positive and negative UWB monocycle pulses with different shape can be generated in the optical domain after their recombination. With the optical-to-electrical conversion at a photodetector, a UWB monocycle pulse is obtained in the electrical domain.

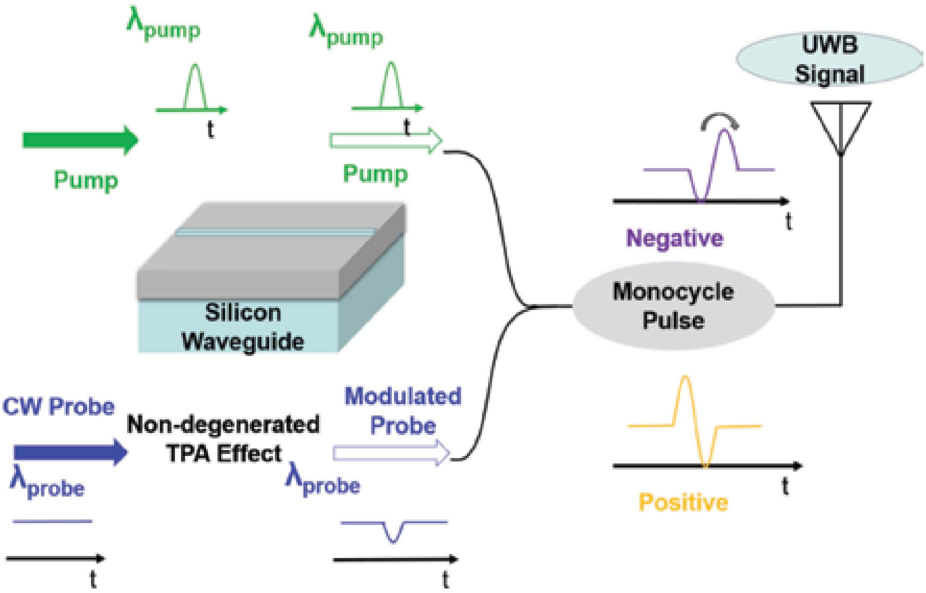

Figure 6. The schematic diagram of the working principle for TPA-based monocycle pulse generation.

2.3. Optical spectral shaping and frequency-to-time mapping

UWB pulses can also be generated based on optical spectral shaping and frequency-to-time conversion using a Fourier transform device. Fourier transform optical spectral shaping and dispersive stretching were implemented to generate adaptive broadband microwave arbitrary waveforms [22, 23]. UWB pulse generation has been widely demonstrated via spatial-light-modulator (SLM)-based spectrum shaper and frequency-to-time mapping [24–26]. But in this approach, the pulse shaping is implemented in free space, which makes the system bulky and complicated. UWB pulses can also be generated based on spectral shaping and frequency-to-time conversion using pure fiber-optic components [27]. The use of fiber-optic components instead of free space optics has the advantage of smaller size, light weight, and the potential for integration using the photonic integrated circuit (PIC) technique.

Figure 7 shows a UWB pulse generation system based on spectral shaping and frequency-to-time mapping using all-fiber components. In the system, the optical power spectrum of a femtosecond pulse from a mode-locked fiber laser (MLFL) is shaped by optical spectral shaper to obtain a spectral shape corresponding to a UWB monocycle or more power-efficient waveform. The wave shaper based on MEMS can act as an excellent spectral shaper for this

Figure 7. The block diagram of a UWB-IR generation system based on optical spectral shaping and frequency-to-time mapping. MLFL, mode-locked fiber laser.

scenario. A certain length of single-mode fiber (SMF) acting as a dispersive element can be used to perform the frequency-to-time mapping. In the meantime, the SMF can also distribute the UWB signals to a remote site. A UWB-IR pulse is then obtained at the output of a high-speed PD. The UWB pulse has a shape that is a scaled version of the user-designed power spectrum. The pulse width is determined by the total dispersion of the SMF. In fact, an ultra-short pulse from the MLFL source can also be divided into two paths by an optical coupler. When the input pulse spectrum from one port is shaped by a reflection filter, the input pulse from the other port is spectrally shaped by a transmission filter. The spectra shapes of the two filters are complementary, which ensures that the time-domain pulses are polarity reversed. Similar to PM-IM conversion, this technique can generate more complicated pulses other than monocycle pulse by applying asymmetric spectral shaping in the complementary filters. Then, the spectrum-shaped pulse is then sent to a length of dispersive fiber to perform frequency-to-time mapping.

2.4. Microwave delay-line filter

We have discussed the generation of monocycle, doublet and triplet pulse generation in the previous section. It is known that monocycle, doublet, and triplet represent the first-, second-, and third-order derivative of the Gaussian pulse. In principle, different order derivatives can be approximated by first- or higher-order differences, which can be implemented via a photonic microwave delay-line filter, with two or three taps, with one negative tap. For a photonic microwave delay-line filter, the filter should operate in the incoherent regime using incoherent detection to avoid optical interference. A photonic microwave delay-line filter with incoherent detection normally has positive coefficients only [28–30]. Thus, it is necessary to design filter with negative coefficients while maintaining the incoherent detection.

The general working principle can be described in **Figure 8**. UWB-IR can be generated by such a system that consists of an N-tap photonic microwave delay-line filter, a light source, an optical modulator, a time delay element, and a PD. The microwave signal is modulated onto the light wave using an optical modulator. The modulated light wave is then sent to an N-tap

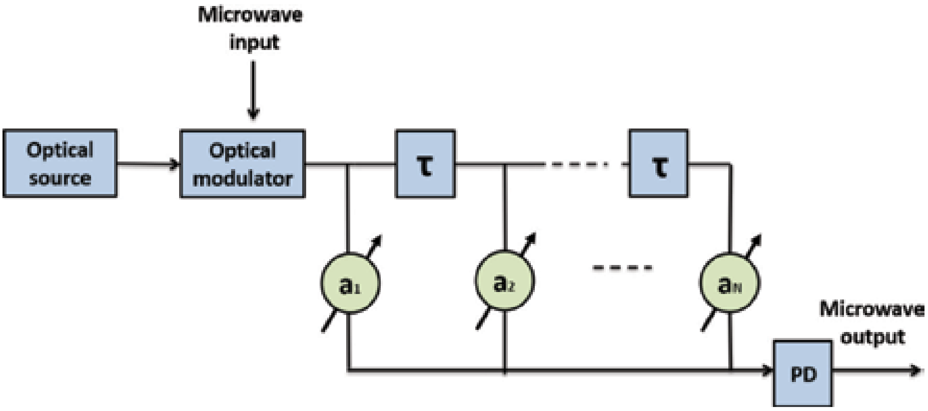

Figure 8. The schematic diagram of the UWB signal generation principle based on microwave delay-line filter.

delay-line device to introduce different time delays with an identical time delay difference between each adjacent tap. The time-delayed signals are then converted to electrical signal via a PD. The multitap delay-line device acts as a multitap RF filter in the electrical domain. The free spectral range (FSR) and the tap coefficients can be designed by introducing appropriate time delay difference. Thus, the desired frequency response of the RF filter can be realized using the photonic devices.

2.5. Photonic integrated circuits

We have mentioned a handful of approaches that can generate the UWB-IR in optical domain. Most of the systems relied on the discrete packaged components like optical fiber, lithium niobate electrooptic modulator, thin-film filter, fiber Bragg grating, spatial light modulator, and so on. Such system is quite bulky and requires sophisticated control on optical phase, polarization, optical intensity, wavelength, and many other parameters. Some of these parameters are extremely sensitive to the environmental variations and thus are difficult to stabilize. From the economical point of view, the UWB system based on many discrete packaged components will suffer from additional losses at the interface between different devices and also suffer from high packaging costs.

Photonic integrated circuits (PICs) have become a new paradigm for on-chip subsystem with a plethora of applications like optical computing, interconnection, sensing, microwave photonics, and so on. Similar to the electronic integrated circuits, the idea of PIC originates from the large-scale integration of various photonic devices and functionalities on a single chip. The benefits from on-chip system based on PIC include low cost, low power consumption, stable performance, and small footprint. Silicon and III–V material systems have been widely used for integrated photonic devices. While III–V material has limited wafer dimension and high cost, silicon is now considered as the most promising photonic integration platform. The past two decades have witnessed the huge success of silicon photonics that advanced from scientific research to commercialization.

Here, we introduce a UWB-IR generation technique using silicon microring resonator, which consists of a bus waveguide and a microring waveguide. The working principle of a microring resonator is shown in **Figure 9**. The bus waveguide and the microring are coupling with each other via a coupler. When light of the resonant wavelength is passed through the bus waveguide, it will cross couple into the microring and builds up in intensity over multiple round trips due to constructive interference. Once it travels through a round trip, it is output to the output bus waveguide. Because only a selected few wavelengths will satisfy the resonance condition within the cavity, the optical ring resonator can function as a filter. If only one bus waveguide is implemented as shown in **Figure 9**, the microring will serve as a notch filter with the output spectrum shown as the inset of the figure. The microring resonance spectrum normally has a Lorentz shape with very large extinction ratio, and the resonance dip of the notch filter induces an abrupt phase change. Thus, microring resonator is a good candidate for a frequency discrimination filter, which can be used for PM-IM conversion. By generation of different types of monocycle pulses as described in **Figure 1**, a delay and superimpose method can produce much more complicated and power-efficient UWB pulses.

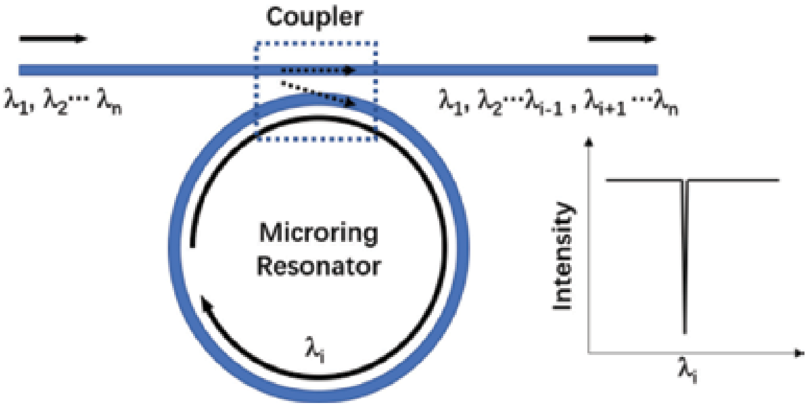

Figure 9. The schematic diagram of a microring resonator. Inset: the schematic optical spectrum at the through port of the microring.

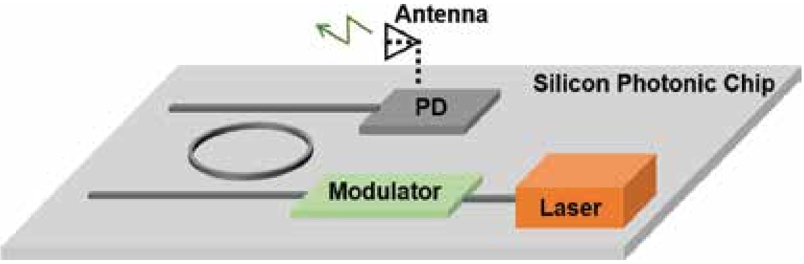

Figure 10. Experimental setup of the UWB generation using MRR and integrated Ge photodetector. PD, photodetector.

The advantages of using silicon microring are the possibility of integration and the extremely small footprint. A possible system setup of the on-chip monocycle UWB-IR generation can be depicted in **Figure 10**.

If we recall the principle illustrated in **Figure 2**, doublet and triplet UWB waveforms can be generated by using a pair of identical filters. In a nonintegrated system, we need to double the efforts and costs to set up another set of filter, cables, connectors, and so forth. In contrast, PIC holds one of the most exciting features of just copying the circuit layout and sharing the same fabrication process. Importantly, the cost is not necessarily doubled since many expenses are shared in a multiproject wafer [31]. A PIC layout for doublet or triplet pulse generation is shown in **Figure 12** where two identical microring resonators produce two asymmetric monocycle pulses. The microring pair can be electrically controlled to adjust the working wavelengths. The microscope image of the tunable microring pair is shown as the inset. After PM-IM conversion via the ring resonator, one of the light waves is time-delayed by a certain length of long waveguide. Then, two paths of optical waves are combined and superimposed by a coupler. Finally, the optical to electrical conversion is performed in the photodiode and hence the electrical doublet or triplet UWB-IR is generated. The microscope images of the long waveguide and the photodiode are shown in the inset of **Figure 11**.

3. UWB signal modulation

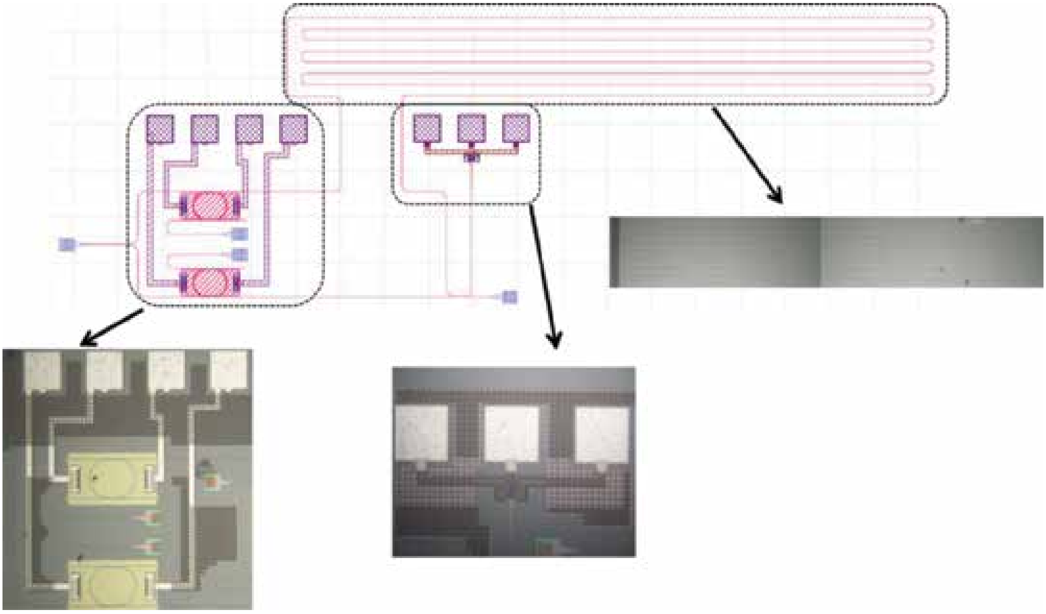

Figure 11. The PIC layout of the on-chip UWB generation system. The inset are the microscope images of the microrings, photodetector, and long waveguides.

UWB-IR is a wide band RF spectrum with extremely low power spectral density. It actually functions as a wireless carrier to deliver information in a short reach scenario. The modulation of UWB-IR is also a fundamental issue in the transmitter design. One of the most intuitive modulation formats that can apply for UWB-IR is the on-off keying (OOK). This format is easy to implement, but it suffers from intensity noise. Pulse position modulation and biphase modulation are alternative formats apart from OOK. Here, we introduce a novel UWB signal modulation scheme using the tunable filter, which can be compatible for both OOK and biphase modulation.

In **Figure 12**, we illustrate the working principle of how to generate and modulate the UWB monocycle pulse using a single tunable filter. Such a tunable filter should have a large extinction ratio and fast tuning speed. Electrooptic silicon microring is one of the perfect candidates for this scheme. As shown in **Figure 12(a)**, when the laser wavelength is set at the center of the linear slope of the ring resonance, a monocycle pulse with a certain intensity is generated. When a driving voltage is applied to the ring resonator, the ring resonance is shifted and its resonance dip is shifted to match the laser wavelength. As a result, the pulse will vanish due to the low intensity at the ring resonance dip and the OOK modulation is achieved.

If the driving voltage is larger, a larger wavelength shift will be introduced to the ring resonance as shown in **Figure 12(b)**. First, the laser wavelength is set to a midpoint at one side of the resonance slope center. Without the electrooptic tuning, a monocycle pulse will be generated. By applying an appropriate swing voltage, the laser wavelength can be just located to the other side of the resonance slope. As a result, the polarity of the monocycle pulse will be reverted since it experiences a π phase shift. The biphase modulation can be

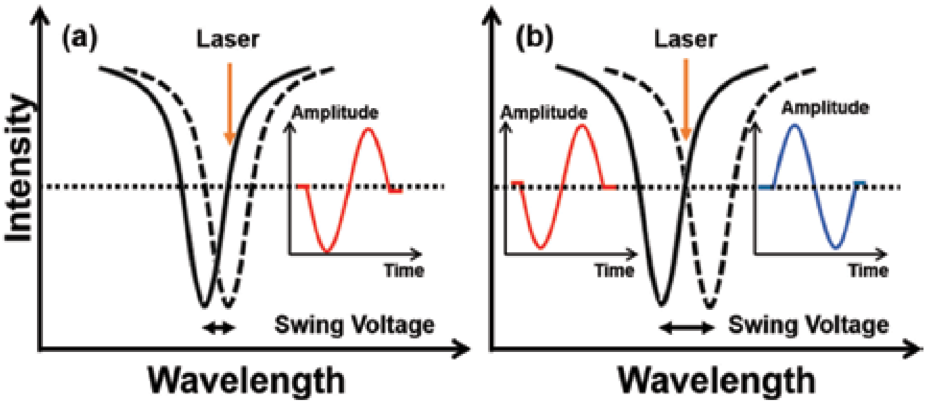

Figure 12. The schematic principle of the tunable-filter-based (a) UWB OOK modulation and (b) UWB biphase modulation.

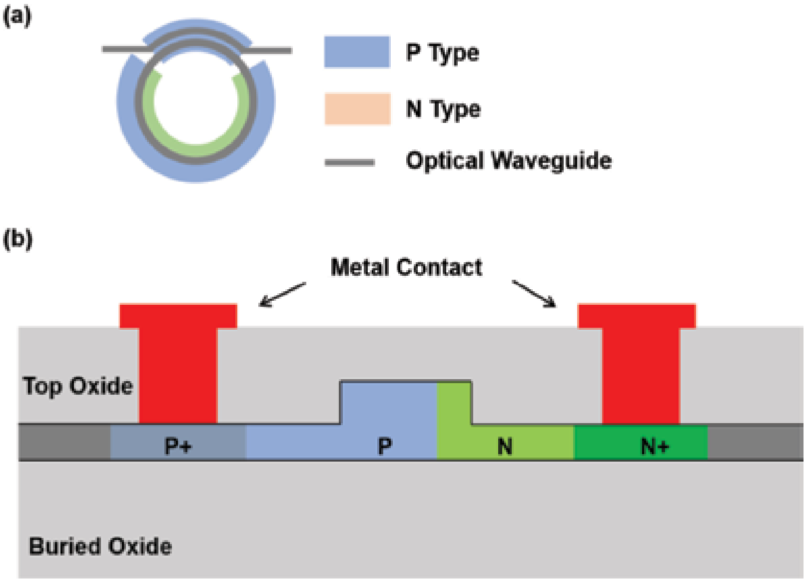

Figure 13. (a) The top-view schematic diagram of the silicon microring modulator and (b) the schematic diagram of the P-N silicon waveguide.

realized if the driving voltages are well controlled with equal intensity for the polarity-reverted monocycle pulse.

An active microring resonator (microring modulator) can be used to simultaneously generate and modulate the UWB-IR. The top view and cross section schematic structure of a silicon ring modulator are shown in **Figure 13(a)** and **(b)**. The resonance wavelength tuning is achieved by modifying the resonance condition, which is expressed by

$$n_{eff}L = m\lambda_i \tag{4}$$

where n_{eff} is the waveguide effective refractive index, L is the round-trip length, m is an integer, and λ_i is the resonance wavelength. The cavity waveguides are normally doped with P- and N-type implantations as shown in **Figure 13**. Silicon is a semiconductor; the doping improves the conductivity of the waveguides, which introduces the free carriers inside the waveguides. The P- and N-type doping forms a P-N junction inside the waveguide with several hundreds of nanometers width. By electrical tuning, the effective index of the waveguide changes due to the variations in carrier distribution, which is called free carrier dispersion effect [32]. The index change results in the resonance shift indicated in Eq. (4), and thus, it could be utilized for UWB-IR generation and modulation.

4. UWB-over-fiber

UWB-over-fiber (UWBoF) has been proposed to effectively distribute UWB-IR signals while keeping the wireless transmission within tens of meters range. For such optical distribution, it can be more cost-effective to implement the generation and distribution of UWB-IR in optical domain, thus avoiding the need for multiple electrical to optical to electrical conversions. An interesting idea is to integrate the UWB signal distribution networks into the existed access networks. By sharing the same fiber, optical UWB-IR and wired downstream signal coexist in the access fiber networks. The fiber to the home brings the wireless UWB signal to the home as well. There are many UWBoF architectures discussed in the literatures. Among those access network solutions, wavelength division multiplexed-passive optical network (WDM-PON) is one of the most promising systems as it has extremely large data capacity. Though it has not been commercialized yet due to the cost issues, it has a bright future since it can fully utilize the nearly infinite optical bandwidth. Here, we introduce a hybrid solution of UWB-IR wireless service that is integrated with a WDM-PON. It provides a wired baseband data service and a UWB-IR signal distributed from the other remote antenna unit (RAU).

The schematic system configuration is shown in **Figure 14**. In such a WDM distribution system that integrates the UWB-IR and wired baseband signal, a silicon PIC is implemented in an optical network unit (ONU) within the WDM-PON architecture. The silicon chip serves as a wireless access point and a wired signal receiver. Centralized light sources are located at the central office, and there are two laser diodes with wavelength close to each other for each transmitter (Tx). This is a trick that is used for separation of the UWB and wired signal at the ONU side. For Tx1, laser diode1 (LD1) is intensity modulated with wired signal, while LD2 is phase modulated with the UWB wireless data. The wavelengths of LD1 and LD2 occupy two adjacent channels of the AWG. All the channels are multiplexed and transmitted in the distribution fiber. At the remote node, the wavelength channel allocated to wired signal is sent to the receiver directly. The other channel is separated into two branches with a portion of the signal remodulated by the upstream data. Since the UWB signal is a phase-modulated CW, the phase information will not affect the upstream data if intensity modulation format is used. Another part of the signal is coupled onto the silicon chip through

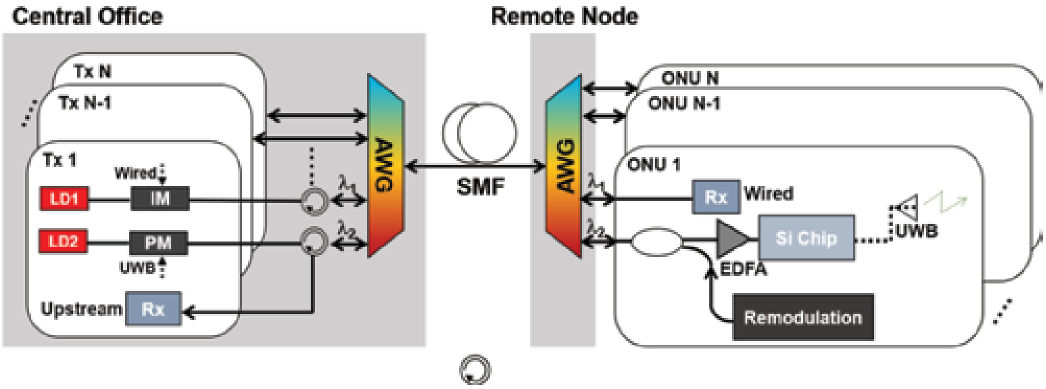

Figure 14. The schematic diagram of the UWBoF system, which is compatible with WDM-PON.

a grating coupler. The on-chip microring resonator performs the PM-IM conversion. The UWB monocycle pulse is generated and converted to electrical signal by a waveguide germanium photodetector, which can be fabricated using fully CMOS compatible process. If the photodetector has enough responsivity, its output can be directly fed into the antenna for wireless emission.

5. Conclusion

Though UWB has not been so widely implemented as Wi-Fi, Bluetooth, and other narrowband services, its broadband nature and intrinsic advantages make it extremely suitable for some particular applications like indoor positioning and tracking. The UWB service has much higher precision and less interferences than other radio systems, which make it promising for Internet of things in the near future. MWP is emerging as an alternative technology for other UWB signal generation and processing in electrical domain. Over the past decade, we have witnessed a lot of lab demonstrations of UWB photonics like UWB waveform generation, UWB signal modulation, UWB-over-fiber, and so on. There are many other topics that remain open to the whole community such as the study on impact of fiber channel impairments, integration of UWB antenna and photonic chip, more power-efficient UWB pulse generation, advanced formats of UWB signal modulation, and so on.

Author details

Ke Xu

Address all correspondence to: kxu@hit.edu.cn

Harbin Institute of Technology, Shenzhen, China

References

[1] Fed. Commun. Commission. Revision of part 15 of the commission's rules regarding ultra-wideband transmission systems. Tech. Rep., ET-Docket 98-153, FCC02-48; 2002

[2] Ghavami M, Michael LB, Kohno R. Ultra-Wideband Signals and Systems in Communication Engineering. 2nd ed. West Sussex: Wiley; 2004. 297 p. DOI: 10.1002/9780470060490

[3] Alarifi A, Al-Salman A, et al. Ultra-wideband indoor positioning technologies: Analysis and recent advances. Sensors. 2016;**16**(5):707. DOI: 10.3390/s16050707

[4] Aiello GR, Rogerson GD. Ultra-wideband wireless systems. IEEE Microwave Magazine. 2003;**4**(2):36-47. DOI: 10.1109/MMW.2003.1201597

[5] Siwiak K, McKeown D. Ultra-Wideband Radio Technology. 2nd ed. Chichester: Wiley; 2004. 264 p. DOI: 10.1002/0470859334

[6] Yang L, Giannakis GB. Ultra-wideband communications: An idea whose time has come. IEEE Signal Processing Magazine. 2004;**21**(6):26-54. DOI: 10.1109/MSP.2004.1359140

[7] Nassar CR, Zhu F, Wu Z. Direct sequence spreading UWB systems: Frequency domain processing for enhanced performance and throughput. In: IEEE International Conference on Communications (ICC '03); 11-15 May 2003; Anchorage. New York: IEEE; 2006. pp. 2180-2186

[8] Balakrishnan J, Batra A, Dabak A. A multi-band OFDM system for UWB communication. In: IEEE Conference on Ultra Wideband Systems and Technologies; 16-19 Nov. 2003; Reston. New York: IEEE; 2004. pp. 354-358

[9] Goavec A, Zarudniev M, Vauche R, Hameau F, Gaubert J, Mercier E. An efficient method of power spectral density estimation for on-chip IR-UWB transmitter self-calibration. IEEE Transactions on Circuits and System I. 2017;**64**(3):686-695. DOI: 10.1109/TCSI.2016.2617887

[10] Vauche R, Muhr E, Fourquin O, Bourdel S, Gaubert J, Dehaese N, et al. A 100 MHz PRF IR-UWB CMOS transceiver with pulse shaping capabilities and pea voltage detector. IEEE Transactions Circuits and System I. 2017;**64**(6):1612-1625. DOI: 10.1109/TCSI.2017.2669902

[11] Lin W, Chen J. Implementation of a new ultrawide-band impulse system. IEEE Photonics Technology Letters. 2005;**17**(11):2418-2420. DOI: 10.1109/LPT.2005.857977

[12] Wu X, Tian Z, Davidson TN, et al. Optimal waveform design for UWB radios. IEEE Transactions on Signal Processing. 2006;**54**(6):2009-2021. DOI: 10.1109/TSP.2006.872556

[13] Xu K, Wu X, et al. Amplitude and phase modulation of UWB monocycle pulses on a silicon photonic chip. IEEE Photonics Technology Letters. 2016;**28**(3):248-251. DOI: 10.1109/LPT.2015.2494000

[14] Luo B, Dong J, Yu Y, et al. Photonic generation of ultra-wideband doublet pulse using a semiconductor-optical-amplifier based polarization-diversified loop. Optics Letters. 2012;**37**(12):2217-2219. DOI: 10.1364/OL.37.002217

[15] Tan K, Shao J, Sun J, et al. Photonic ultra-wideband pulse generation, hybrid modulation and dispersion-compensation-free transmission in multi-access communication systems. Optics Express. 2012;**20**(2):1184-1201. DOI: 10.1364/OE.20.001184

[16] Fu X, Dai Y, Shu C. Reconfigurable photonic ultrawideband pulse generation from an optically injected semiconductor laser. Optics Letters. 2013;**38**(6):968-970. DOI: 10.1364/OL.38.000968

[17] Zheng J, Zhu N, Wang L, et al. Photonic generation of ultrawideband (UWB) pulse with tunable notch-band behavior. IEEE Photonics Journal. 2012;**4**(3):657-663. DOI: 10.1109/JPHOT.2012.2193562

[18] Li W, Hofmann W, Zhu N, et al. Generation of ultra-wideband triplet pulses based on four-wave mixing and phase-to-intensity modulation conversion. Optics Express. 2012;**20**(18):20222-20227. DOI: 10.1364/OE.20.020222

[19] Yue Y, Huang H, Zhang L, et al. UWB monocycle pulse generation using two-photon absorption in a silicon waveguide. Optics Letters. 2012;**37**(4):551-553. DOI: 10.1364/OL.37.000551

[20] Zhou E, Xu X, Lui KS, et al. A power-efficient ultra-wideband pulse generator based on multiple PM-IM conversions. IEEE Photonics Technology Letters. 2010;**22**(14):1063-1065. DOI: 10.1109/LPT.2010.2050469

[21] Feng H, Fok M, et al. A reconfigurable high-order UWB signal generation scheme using RSOA-MZI structure. Photonics Journal. 2014;**6**(2):7900307. DOI: 10.1109/JPHOT.2014.2306832

[22] Chou J, Han Y, Jalali B. Adaptive RF-photonic arbitrary waveform generator. IEEE Photonics Technology Letters. 2003;**15**(4):581-583. DOI: 10.1109/LPT.2003.809309

[23] Lin IS, Mckinney JD, Weiner AM. Photonic synthesis of broadband microwave arbitrary waveforms applicable to ultra-wideband communication. IEEE Microwave and Wireless Components Letters. 2005;**15**(4):226-228. DOI: 10.1109/LMWC.2005.845698

[24] Mckinney JD, Lin IS, Weiner AM. Shaping the power spectrum of ultra-wideband radio-frequency signals. IEEE Transactions on Microwave Theory and Techniques. 2006;**54**(12):4247-4255. DOI: 10.1109/TMTT.2006.885573

[25] Mei Y, Jin T, et al. Characterization of the photonic generation of phase-coded RF signals based on pulse shaping and frequency-to-time mapping. Applied Optics. 2015;**54**(13):3956-3962. DOI: 10.1364/AO.54.003956

[26] Mckinney JD, Weiner AM. Compensation of the effects of antenna dispersion on UWB waveforms via optical pulse-shaping techniques. IEEE Transactions on Microwave Theory and Techniques. 2006;**54**(4):1681-1686. DOI: 10.1109/TMTT.2006.871999

[27] Wang C, Zeng F, Yao J. All-fiber ultrawideband pulse generation based on spectral shaping and dispersion-induced frequency-to-time conversion. IEEE Photonics Technology Letters. 2007;**19**(3):137-139. DOI: 10.1109/LPT.2006.888966

[28] Fandino J, Munoz P, et al. A monolithic integrated photonic microwave filter. Nature Photonics. 2017;**11**:124-129. DOI: 10.1038/nphoton.2016.233

[29] Minasian RA. Photonic signal processing of microwave signals. IEEE Transactions on Microwave Theory and Techniques. 2006;**54**(2):832-846. DOI: 10.1109/TMTT.2005.863060

[30] Capmany J, Ortega B, Pastor D. A tutorial on microwave photonic filters. Journal of Lightwave Technology. 2006;**24**(1):201-229. DOI: 10.1109/JLT.2005.860478

[31] Lim AEJ, Song J, Fang Q, et al. Review of silicon photonics foundry efforts. IEEE Journal of Selected Topics in Quantum Electronics. 2014;**20**(4):405-416. DOI: 10.1109/JSTQE.2013.2293274

[32] Soref R, Bennett B. Electrooptical effects in silicon. IEEE Journal of Quantum Electronics. 2003;**23**(1):123-129. DOI: 10.1109/JQE.1987.1073206

Edited by Dusan Kocur

Ultra-wideband (UWB) technology is a radio technology that uses electromagnetic waves with a very low power spectral density occupying a bandwidth of more than 25% of a centre frequency, or more than 0.5GHz, for short-range remote sensing, high-bandwidth communications or object positioning. The detailed analyses of state-of-the-art UWB technology has shown that this technology is very interesting and promising with a great application potential. Following these facts, our book attempts to present current and emerging trends in research and development of UWB systems. The book is focused on basic components of UWB systems such as antennas, filters, photonic approach for signal processing methods, as well as on some applications of UWB systems (human target analysis, cancer detection).

Published in London, UK

IntechOpen

ISBN 978-1-83962-069-0